Alma Mater Studiorum · University of Bologna

Department of Physics and Astronomy
Master Degree Programme in Astrophysics and Cosmology

Monte Carlo simulations of the X/Gamma-ray Imaging Spectrometer instrument onboard the THESEUS mission

Master's Thesis

Submitted by
Alfonso Pisapia

Supervisor
Prof. Cristian Vignali
Co-supervisor
Dr. Riccardo Campana

V Session
Academic Year 2023/2024

For my family and my friends

Contents

Abstract

Gamma-Ray Bursts (GRBs) are among the most studied high-energy transient phenomena in the last few decades. Their emission consists of very rapid and energetic radiation (the *prompt* emission), peaking in the γ-ray band, followed by the *afterglow* emission, which spans a broad energy range. This characteristic has allowed for the investigation of their nature and properties. Numerous efforts have been dedicated to developing experiments capable of detecting these transient events, which occur randomly from any direction in the sky. The extreme luminosity of GRBs (10^{53} erg/s) makes them invaluable tools for investigating the Early Universe and advancing Multi-Messenger Astrophysics. It is therefore essential to study all classes of GRBs across a broad energy range, to uncover the unresolved mysteries surrounding them, as well as to investigate their use to probe the most important cosmological parameters.

The *Transient High-Energy Sky and Early Universe Surveyor* (THESEUS) mission has been proposed as a pioneering mission for the detection and localization of GRBs. Currently, it is a candidate for the ESA M7 medium-class mission, and is undergoing a Phase A study. The mission was also previously considered in 2018–21 for the M5 launch slot. The innovative and cutting-edge capabilities in the design of THESEUS are expected to significantly advance our understanding of GRBs. Its payload includes two wide-field instruments, the *Soft X-ray Imager* (SXI) and the *X and Gamma-ray Imaging Spectrometer* (XGIS), both operating in the X-ray and γ-ray energy bands, as well as a high-resolution *InfraRed Telescope* (IRT). The combined capabilities of these instruments will enable THESEUS not only to continuously scan the sky for high-energy transients but also to rapidly re-point ($>7^\circ$/min) at them with the telescope, allowing for onboard redshift estimation. This will enable THESEUS to play a crucial role in the Multi-Messenger Astrophysics and Time-Domain Astrophysics and to work in a synergic way with future facilities for electromagnetic radiation detection, as well as for neutrinos and gravitational waves.

In this thesis, a study has been conducted on the performance of the XGIS instrument, which works both as an imager, utilizing the coded mask technique, and as a spectrometer. The focus of my study is on evaluating XGIS effective area, instrumental response, and estimates of the background noise count rate that the instrument will encounter in the Low Earth Orbit (LEO) where it will operate. The performance has been

assessed using a Monte Carlo simulation software built upon the CERN Geant4 toolkit, which allows for the study of the passage of particles through matter. This toolkit is a standard in high-energy physics, and is also used by space agencies, such as NASA and ESA, to assess the performance of high-energy instruments.

In particular, this work implements several improvements and upgrades to the simulations carried out during the previous M5 Phase A study, by introducing a more accurate mass model for XGIS compared to the original design. A random-pattern realistic coded mask and various passive layers, which were planned during the design phase but not tested in simulations, have been included. Simulations with both the simple and upgraded mass models will then be compared.

The outline of this thesis is as follows.

Chapter 1 introduces the astrophysical phenomenon of GRBs, in particular focusing on the history of the past 50 years, in which the observations carried on by space missions led to the formulation of the current Standard Model for GRBs. The chapter details the characteristics of their prompt and afterglow emission, as well as the central engine that triggers their explosion. Additionally, some facilities that will play a crucial role in the coming decades, including THESEUS, are presented within the context of the Multi-Messenger Astrophysics domain.

In **Chapter 2**, the THESEUS mission concept is presented, outlining its scientific objectives along with the scientific and technical requirements that will ensure its success. Additionally, the instruments comprising its payload and the planned observational strategies are described.

In **Chapter 3**, a detailed explanation is provided of the physical principles underlying the operation of XGIS and the technologies it uses to detect X-rays and γ-rays. The detection is achieved through a compact experiment composed of two Silicon Drift Detectors (SDDs) coupled with scintillator bars, which is ideal for a space mission constrained by budget, mass, and volume limitations. The adopted technique, the coded mask principle, is explained in detail. After providing a brief description of the software used for the simulations and how they are implemented, the employed mass model is analyzed, along with the added improvements, including their effects on radiation transmission. Finally, the derived effective area as well as the instrument response matrix, are presented.

In **Chapter 4**, the sources of background in LEO are described, along with their effects on the instruments. The results of their simulations are then presented, showing the expected count rates for both the simple and upgraded mass models. The strategies adopted to mitigate the effects of the background are also discussed.

Finally, **Chapter 5** provides a summary of the results, outlining also the future activities planned for studying the XGIS performance in the context of the ESA Phase A study.

Chapter 1

Gamma-Ray Bursts

Gamma-ray bursts (GRBs) are sudden bright flashes of radiation with spectral energy distributions peaking in the γ-ray band. The long journey that began over 50 years ago with the first detection of gamma-ray bursts (Frontera, 2024), marked by the gradual unraveling of the mystery behind their origin, has made them among the most fascinating phenomena in the Universe. Moreover, increasing efforts are still dedicated to uncovering their hidden secrets and exploring the profound connections between GRBs and the diverse fields of astrophysics, where their properties play a significant role.

GRBs are essentially bright ultra-relativistic jets in galaxies at cosmological distances, with kinetic luminosities exceeding 10^{53} erg/s (Gehrels et al., 2009; Vedrenne and Atteia, 2009; Longair, 2011); their brightness is capable of outshining any X-ray and gamma-ray source. They are considered to be the most energetic phenomena in the universe known to date. Their emission, unpredictable in both direction and time of arrival, has an energy spectrum extending from a few keV up to GeV, and a variable duration from milliseconds to several hundreds of seconds. The performance of modern X-ray and gamma-ray detectors allows for the detection of 2–3 GRB events per day across the entire sky (Frontera, 2024).

The following sections outline the key milestones in the history of GRB discoveries, which have led to the currently accepted Standard Model for GRBs, highlighting the crucial role played by various space missions and the technological advancements in scientific instrumentation that have driven these breakthroughs. Our current understanding of GRBs is the result of a close collaboration within the international scientific community, in which the Italian contribution has played a fundamental role in the last decades.

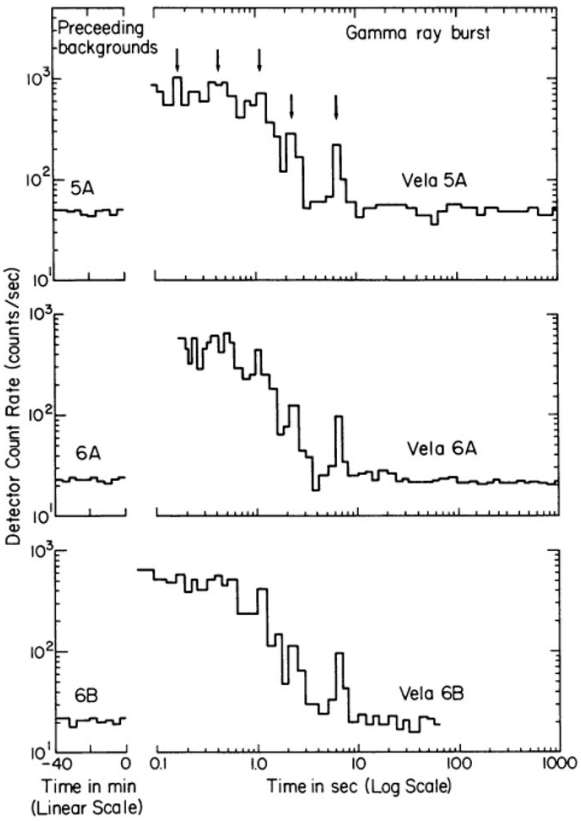

Figure 1.1: *One of the 73 gamma-ray bursts observed by the three Vela satellites. The figure shows the count rate as a function of time for the gamma-ray burst of August 22, 1970. Each plot presents: in linear time scale, the background count rates for the period immediately preceding the burst; in logarithmic time scale, the record of the burs with a distinct peak around 6.5 s (Klebesadel et al., 1973).*

1.1 A new transient emission

The earliest detection of a flash of γ-rays, the so-called *prompt* emission, occurred in 1967, by chance, thanks to the American Vela satellites, which in those years were intended to monitor potential atmospheric explosions of nuclear weapons, experiments that were prohibited during the Cold War years. This constellation of satellites was equipped with γ-ray experiments consisting of six CsI(Tl) scintillators (cesium iodide, doped with thallium, see Chapt. 3) with a total volume of 60 cm^3, energy passband 0.2–1.5 MeV, capable of achieving nearly isotropic sensitivity. High atomic number materials were used to shield scintillators from charged particles. They were able to detect an emission different from any known nuclear weapon signature, and after this, others followed (Klebesadel et al., 1973).

The Los Alamos team excluded the terrestrial and solar origins of these events. The detection of 73 GRB events (Fig. 1.1) over a decade by the Vela spacecraft was published in those years, and subsequently, many other instruments and space missions were developed devoted to the detection of GRBs, in order to find what triggers the emission, the sites and the power released by these events.

The first clues came from the Konus experiment on board the Russian Venera satellites: six NaI(Tl) scintillators (sodium iodide, doped with thallium) oriented along six different directions to cover the entire sky. It was capable of localizing the direction of GRBs within an arcminute using triangulation and obtaining the photon spectrum and the temporal evolution of the signal. The most significant evidence was the recording of an isotropic distribution of events across the sky, implying that GRBs originate either very close to or very far from Earth.

In the early 1990s, the most advanced instrument for GRB detection was BATSE (Burst and Transient Source Experiment) on board the American Compton Gamma Ray Observatory satellite. It consisted of eight NaI(Tl) Large Area Detectors (LADs) sensitive in the 30 keV–2 MeV energy range, positioned at the corners of the spacecraft with an exposed area of 2025 cm^2 each. For each LAD, there was a smaller spectroscopy detector (SD) with a detection area of about 600 cm^2, optimized for energy resolution and broad energy coverage (10 keV – 11 MeV). BATSE was able to confirm the isotropic distribution of GRBs, with no dipole and quadrupole components (Fig. 1.2a). It also succeeded in establishing:

- the bimodality of prompt emission duration, in accordance to which GRBs events are classified: *short* and *long*, separated by ∼2 s duration (Fig. 1.2b). Results also showed that short bursts have a harder spectrum then long bursts (higher ratio of high to low energies);

- the spectral distribution of the prompt emission was well described a smoothed broken power law, also called Band function (Band et al., 1993):

$$N_E(E) = \begin{cases} A \left(\frac{E}{100\,\mathrm{keV}}\right)^{\alpha} \exp\left(-\frac{E}{E_0}\right) & (\alpha-\beta)E_0 \geq E \\ A \left[\frac{(\alpha-\beta)E_0}{100\,\mathrm{keV}}\right]^{\alpha-\beta} \exp(\beta-\alpha) \left(\frac{E}{100\,\mathrm{keV}}\right)^{\beta} & (\alpha-\beta)E_0 \leq E \end{cases} \tag{1.1}$$

  At low energies, a power law continuum with an exponential cutoff $N_E(E) \propto E^{\alpha}\exp(-E/E_0)$ prevails, while the high energies are described by a steeper power law $N_E(E) \propto E^{\beta}$ with $0 \lesssim \beta \lesssim \alpha$ and 100 keV $\lesssim E_0 \lesssim$ 1 MeV, where E_0 is the break in the spectrum. Typical values of the parameters are centered in $\alpha = -1$, $\beta = -2.3$, $E_0 = 150$ keV (Vedrenne and Atteia, 2009).

There is considerable variability in the γ-ray prompt light curves of GRBs. Both long and short bursts can display temporal profiles that range from smooth, single-peaked pulses to complex multi-pulses. The prompt emission can be described using

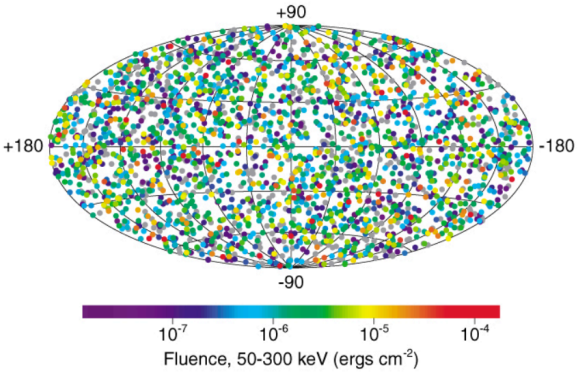

(a) *Sky distribution in galactic coordinates of 2704 GRBs detected with the BATSE experiment aboard the Compton Gamma Ray Observatory satellite (Longair, 2011).*

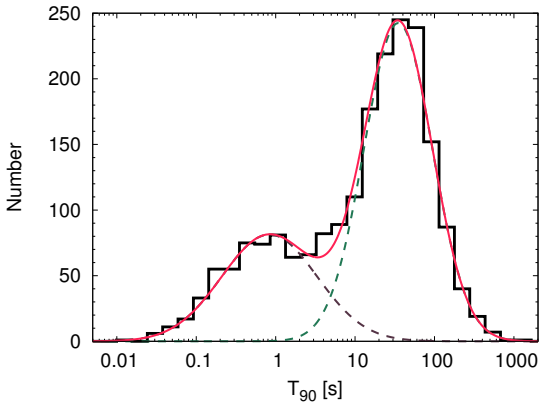

(b) *Distribution of T_{90} for 2006 GRBs detected with BATSE with significant T_{90} estimates. T_{90} is defined as the time during which the GRB cumulative counts increase from 5% to 95% of the total detected counts. Dashed lines give the best fit to the T_{90} distribution (Frontera, 2024).*

various spectral and temporal parameters, for which statistical correlations have been found, as shown in Fig. 1.3. However, the physical reasons behind these correlations are still not fully understood. As summarized in Gehrels et al. (2009):

a the variability or spikiness of the light curve has been found to correlate with the peak luminosity ($L_{\rm peak}$) or the total isotropic energy of the burst ($E_{\rm iso}$);

b the time lag between individual peaks observed in different energy bands is shown to be negatively correlated with luminosity for long bursts, while for short bursts the lag is either small or undetectable;

c the peak energy (E_P) is also found to correlate with the isotropic energy ($E_{\rm iso}$) for long bursts, with short bursts being clear outliers (the so-called *Amati Relation* from the discovery paper by Amati et al. 2002);

d furthermore, the total isotropic energy emission is linked to the duration of the burst, with both short and long bursts lying approximately on the same correlation line;

e Short GRBs also appear to be harder in X-rays compared to long;

f finally, the prompt GRB light curves can generally be broken down into a series of individual pulses, with rise times being shorter than decay times on average.

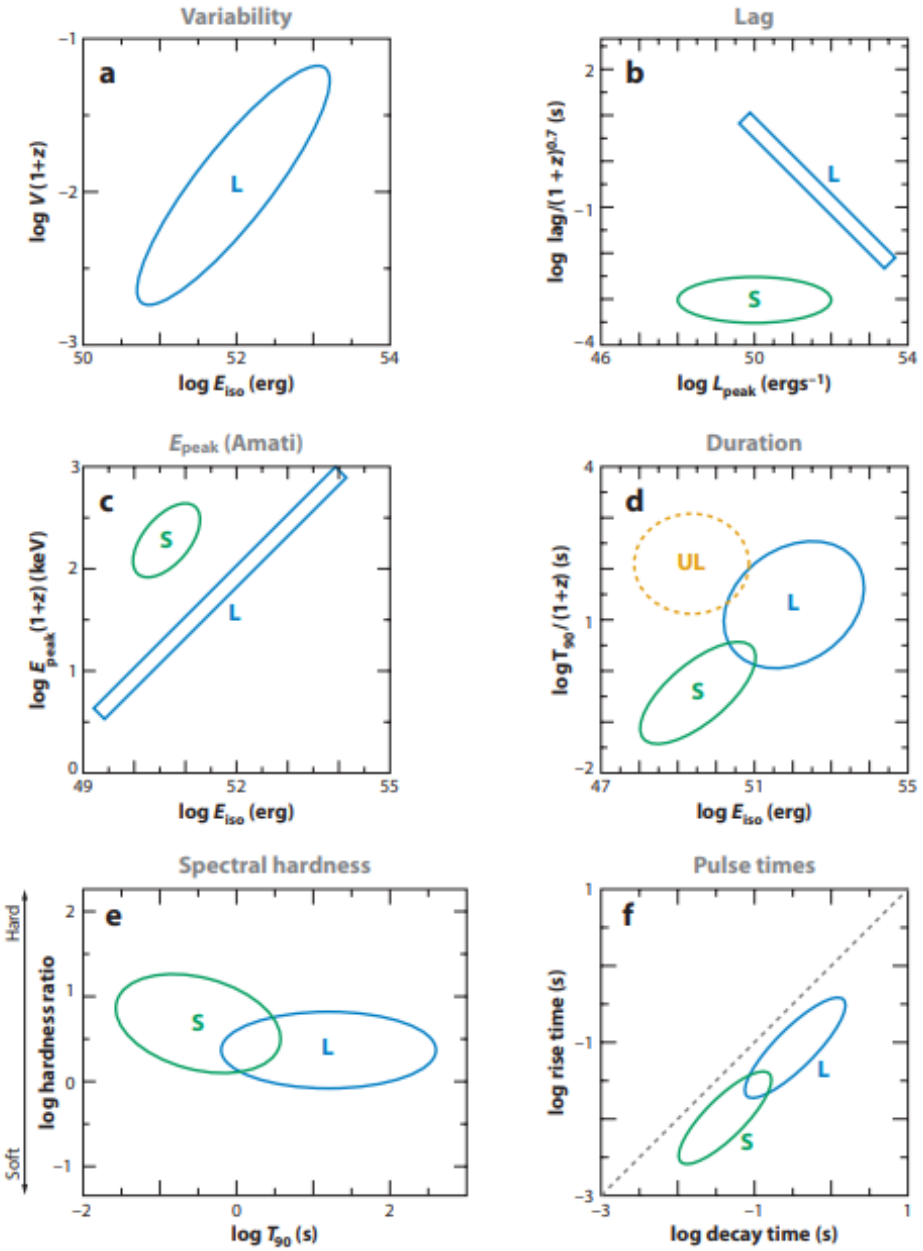

Figure 1.3: *Correlations between various prompt emission properties for long (L), short (S), and underluminous (UL) GRBs. (a) Variability scaled to the burst frame versus* $E_{\rm iso}$*. (b) Spectral lag scaled to the burst frame versus peak luminosity. (c)* $E_{\rm peak}$ *scaled to the burst frame versus* $E_{\rm iso}$*. (d) Duration scaled to the burst frame versus* $E_{\rm iso}$*. (e) Spectral hardness versus observed duration. (f) Pulse rise time versus its decay time (Gehrels et al., 2009).*

1.2 The BeppoSAX era

Only with the launch of the Italian-Dutch satellite BeppoSAX (Satellite per Astronomia X, Fig. 1.4) in 1996 did it become possible to localize GRBs in the sky (Frontera, 2024; Piro, 1997). Indeed, up to that moment, not only was imaging difficult due to the challenge of focusing γ-rays, but the prompt emission also faded within a few seconds, thus preventing the facilities available at that time from achieving accurate angular positioning for follow-up observations. Thanks to a localization accuracy between 3 and 5 arcminutes, never achieved before, and the detection of X-ray, optical, and radio counterparts from follow-up observations, it was possible to confirm the interpretation of GRBs as major explosive events occurring in galaxies at cosmological distances.

BeppoSAX had ambitious scientific objectives, aiming to study celestial X-ray sources. It employed wide-field instruments to monitor the variability of the X-ray and gamma-ray sky over a broad energy range (0.1–300 keV). In addition, narrow-field instruments were used for spectroscopic studies in a more limited range (2–30 keV). At first, GRBs were not included as the main science goal because, at that time, it was not clear whether any delayed associated X-ray emission could be detected. To achieve these objectives, the payload consisted of:

- two narrow-field instruments (NFIs) oriented in the same direction: a Gas Scintillator Proportional Counter (GSPC) with 2–35 keV energy passband, surmounted by a coded mask (3° FOV) with arcminute imaging capability, and a Phoswich Detection System (PDS) at higher energies (15–300 keV), consisting of four independent detection units, each one made of a sandwich of NaI(Tl) plus CsI(Na) scintillator crystals. The NaI(Tl) was used as the main detector, with the CsI(Na) as an active shield from the bottom. This technique, called phoswich (PHOSphor sandWICH), had been demonstrated to provide a very low instrument background. To further reduce the background, four slabs of CsI(Na) detectors, in anti-coincidence with the four phoswich units, laterally covered the instrument. The PDS FOV, of 1.5° (Full Width at Half Maximum, FWHM), was obtained by means of honeycomb collimators;

- two wide-field cameras (WFCs) made of a proportional counter surmounted by a coded mask, with axes perpendicular to the NFI and in opposite directions to each other. Energy band of 2–28 keV and field of view (FOV) $20° \times 20°$ (FWHM) with imaging capability with an angular resolution of 3–4 arcmin.

During the industrial phase A study, four focusing telescopes having the same on-axis direction, one Low Energy Concentrator Spectrometer (LECS) with a passband from 0.1 to 10 keV, and the other three Medium Energy Concentrators Spectrometers (MECS) with a passband from 1.3 to 10 keV, were included. Moreover, because of the high scientific interest for X-ray pulsars spectra, GSPC was improved with a higher gas pressure

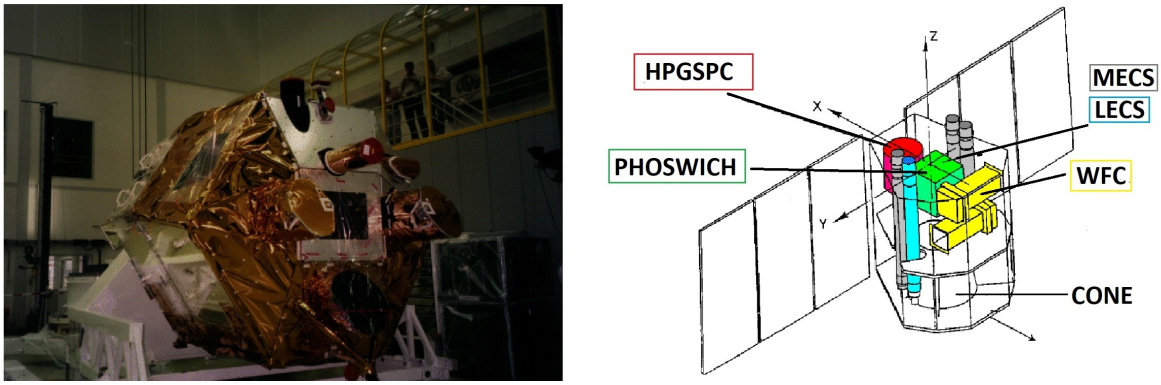

Figure 1.4: *The BeppoSax satellite (left) and payload schematic view (right) (Miliucci et al., 2024).*

(HPGSPC). During the phase of design, it was decided (Frontera, 2024) to use the four slabs of CsI(Na) anti-coincidence detectors as a Gamma-Ray Burst Monitor (GRBM) with a passband from 40 to 700 keV. In fact, by exploiting the parallel alignment of two of these elements with the WFCs, the simultaneous detection of a GRB within the fields of view of both instruments allowed the signal to be classified as a true GRB by the GRBM and localized with an accuracy between 3 and 5 arcminutes by the WFCs, a precision never achieved before. Moreover, the combined presence of the GRBM and WFCs allowed an unprecedented capability of detecting and fast positioning GRBs and starting follow-up observations.

The first GRB prompt emission identified by both GRBM and WFC was localized only 20 days after detection. By the time BeppoSAX NFI pointed in that direction, no X-ray counterpart was found (Piro et al. (1997b)). Therefore, it was clear that, in order to capture GRB afterglow emission, it was necessary, after a very accurate detection of the prompt emission, to optimize all processes aimed at pointing instruments across all spectral bands as quickly as possible toward the source.

1.2.1 The GRB afterglow discovery

The first time afterglow emission was recorded for GRB970228 (Costa et al., 1997). The detection, achieved with the GRBM, and the localization, performed by one of the two WFCs, revealed a light curve with an initial bright peak followed by three additional peaks of decreasing brightness (Fig. 1.5a, 1.5b). Follow-up observations were conducted by the NFI eight hours later. Within the FOV of the MECS, a previously unknown source was discovered (SAX J0501.7+1146), with a flux of $(2.8\pm0.4)\times10^{-12}$ erg cm^{-2} s^{-1} in the 2–10 keV band. Subsequent observations showed that the source had faded by a factor of 20 over a timescale of three days. The confirmation that this new X-ray source represented a delayed emission, the so-called *afterglow*, from the GRB event, was

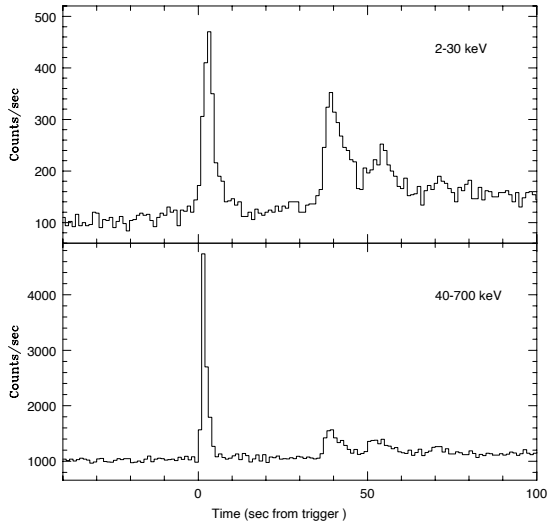

(a) *Time profile of GRB970228 in the γ-ray (from the Gamma-Ray Burst Monitor) and X-ray (from the Wide Field Camera) bands. The origin (time 0) is the trigger time. The first pulse is shorter in γ-rays than in X-rays. There are three additional pulses (at $\sim$35, 50 and 70 s from the trigger) that are much enhanced in the X-ray band. The total burst duration is $\sim$80 s (Costa et al., 1997).*

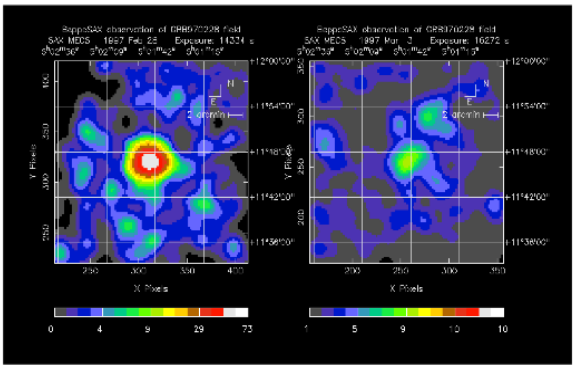

(b) *X-ray images of GRB 970228 as detected by MECS telescopes at two different times. The image on the left is that obtained 8 to 16 h after the burst. The figure on the right is the image obtained in the observation 3.5 days after the burst. From the first to the second X-ray observations, the source had faded by a factor 20 in $\sim$three days (Costa et al., 1997).*

supported by the matching power-law decay patterns observed in the temporal behavior recorded by both instruments.

Further observations were conducted in the following weeks in the optical band by observatories such as the William Herschel Telescope, the Isaac Newton Telescope, and the Hubble Space Telescope. These observations not only revealed the presence of a previously unknown optical source that was fading from $V = 21.3$ to $V > 23.6$ but also indicated that the source appeared to be embedded in a faint nebular structure, likely a host galaxy. A detailed spectral analysis of GRB970228 and its afterglow revealed that the spectrum of the prompt emission was consistent with the Band function that became harder within each peak, while the afterglow spectrum followed a stable power law $N_E(E) \propto E^{-2.04}$.

1.2.2 The first measurement of GRB distance

Another milestone for BeppoSAX was the detection of GRB970508, which resolved the mystery of whether GRBs originated in our galaxy or in distant galaxies. It confirmed remote galaxies as the host sites of GRBs, sweeping away all the galactic models. The

combined localization of the transient by the GRBM and WFC was followed by the identification of an unknown X-ray source by the NFI (1SAX J0653.8+7916) (Piro et al., 1997a). The source coordinates were promptly distributed, enabling several groups to observe and identify an optical counterpart with increasing brightness over the following two days, reaching a peak magnitude of $R = 20.14 \pm 0.03$, and subsequently decaying according to a power-law profile. Follow-up observations using the Keck Low Resolution Imaging Spectrograph detected emission lines at a redshift of $z = 0.835$, originating from an extended source in the same position as the point-like object: the galaxy that had hosted the fading object.

Determining the distance at which a γ-ray burst occurs is crucial for establishing its energy scale. From the luminosity distance of the GRB970508 optical counterpart (1.49×10^{28} cm), obtained assuming a standard Friedmann cosmology with $H_0 = 70$ km s^{-1} Mpc^{-1} and $\Omega_0 = 0.2$, it was possible to derive the first estimate of the energy released by a GRB: $E_{\rm iso} = (0.61 \pm 0.13) \times 10^{52}$ erg, assuming an isotropic emission. GRB970508 was also notable for the discovery of the first radio afterglow using the VLA radio telescope.

Currently, the most distant burst that has been spectroscopically confirmed is at $z \simeq 8.2$ (GRB090423, Tanvir et al. 2009), indicating that GRB observations are very promising for exploring the high-redshift universe.

1.2.3 Swift contribute to afterglows

A significant contribution to afterglow studies was made by NASA Swift satellite, which, following the successes of BeppoSAX, was built with a similar configuration (Gehrels et al., 2004). Launched in 2004 and still operational, Swift is equipped with a wide-field GRB monitor with a coded mask, the Burst Alert Telescope (BAT, 15–150 keV), for the prompt identification and localization of gamma-ray bursts (Fig. 1.6), as well as an X-ray Telescope (XRT, 0.1–10 keV) and an Ultraviolet/Optical Telescope (UVOT) for afterglow observations. Thanks to its rapid response capability, follow-up observations could be performed in less than two minutes, leading to two major breakthroughs: the characterization of the early afterglow properties of long GRBs and the detection of afterglows from short GRBs, which had been beyond the reach of BeppoSAX. Swift showed the presence of a canonical light curve (1.8), with three distinct power-law decays ($\propto t^{-\beta}$): initially ($\lesssim 500$ s) very steep ($3 < \beta < 5$), then ($10^3 < t < 10^4$ s) very shallow ($0.5 < \beta < 1$) and after several hours a decay $1.0 < \beta < 1.5$ as found with BeppoSAX, consistent with photo-electrically absorbed power law. Overall, afterglows shown in Fig. 1.7 display light curves with a variety of power-law slopes.

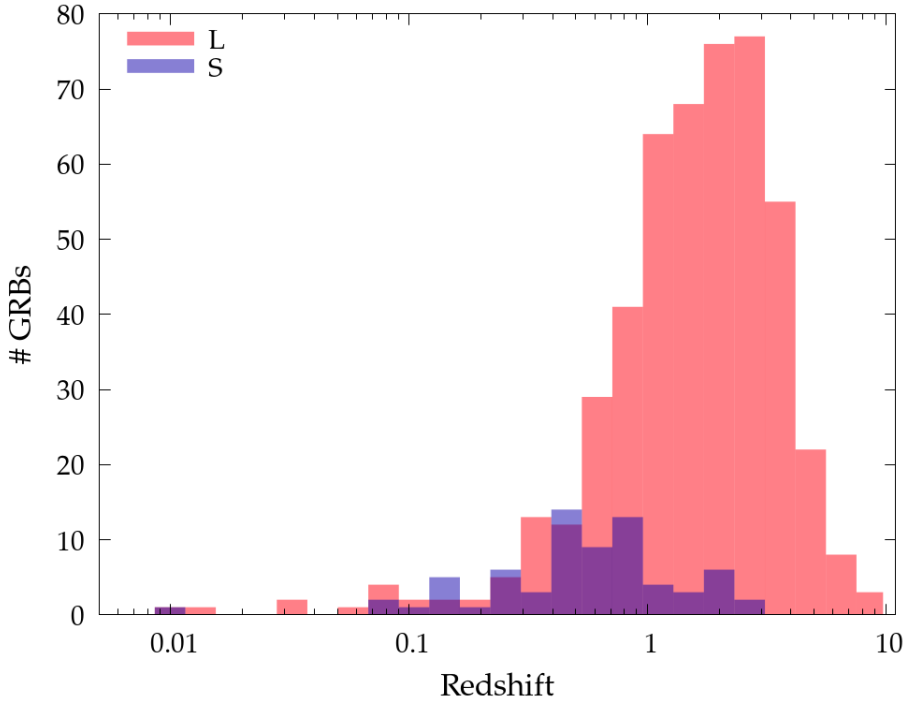

Figure 1.6: *Redshift distribution of 70 short (purple) and 488 long GRBs, list updated up to April 2024. Most of them have been discovered and promptly localized with Swift. The peak frequency of short GRBs is at lower redshift compared to that of long GRBs (Frontera (2024).*

1.3 Host Galaxies

Much of our knowledge about GRBs comes not from direct observations of the prompt burst radiation, but from examining their afterglows. These afterglows illuminate the area around the burst and provide insights into their host galaxies. Furthermore, by performing spectroscopy of the host galaxies and afterglow spectra, it has become increasingly possible to accurately estimate the redshift of GRBs.

Surveys of long GRBs have established that their host galaxies are typically sub-L* galaxies (with median luminosity $L \sim 0.1L^*$, where $L*$ is the characteristic galaxy luminosity controlling the cut-off of the Schechter function, Schechter 1976), featuring exponential-disk profiles Specific Star-Formation Rates (SSFR $\sim$1 Gyr^{-1}) (Gehrels et al., 2009). Thanks to Swift, the redshift range of GRB host galaxies has been extended from $z \sim 4$ to $z \sim 9$. The ability to determine redshifts via afterglow spectroscopy avoids mass and luminosity biases, allowing these galaxies to be used for studying the mass-metallicity relation (Fig. 1.9). Mass-metallicity studies suggest that long GRB progenitors originate in low-metallicity environments, with such conditions becoming more common at $z > 1$.

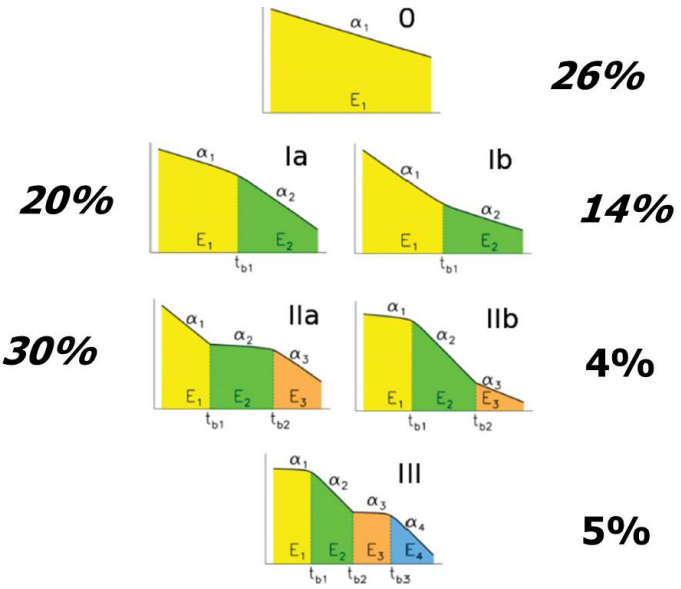

Figure 1.7: *Different types of afterglow light curves in the energy band 0.1–10 keV observed by Swift starting from $T \geq 60$ s. The fraction of GRBs with the given type is also shown. Initially, the supposed light curve was thought to resemble either the IIa or Ia, whose frequencies cover only 50% of the cases (Margutti et al., 2013).*

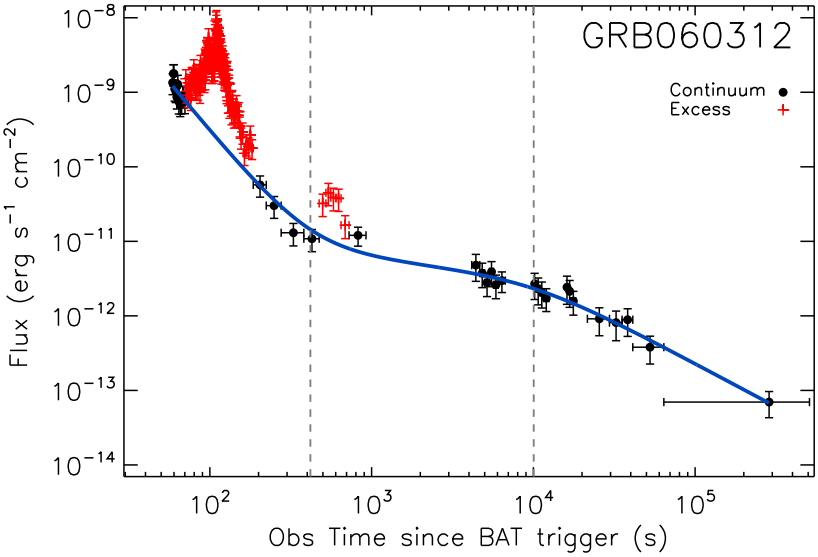

Figure 1.8: *Example of light curve of the intrinsic 0.6–30 keV afterglow starting from $T \geq 60$ s as detected by Swift. Vertical dashed lines are the best estimates of the break times (Margutti et al., 2013).*

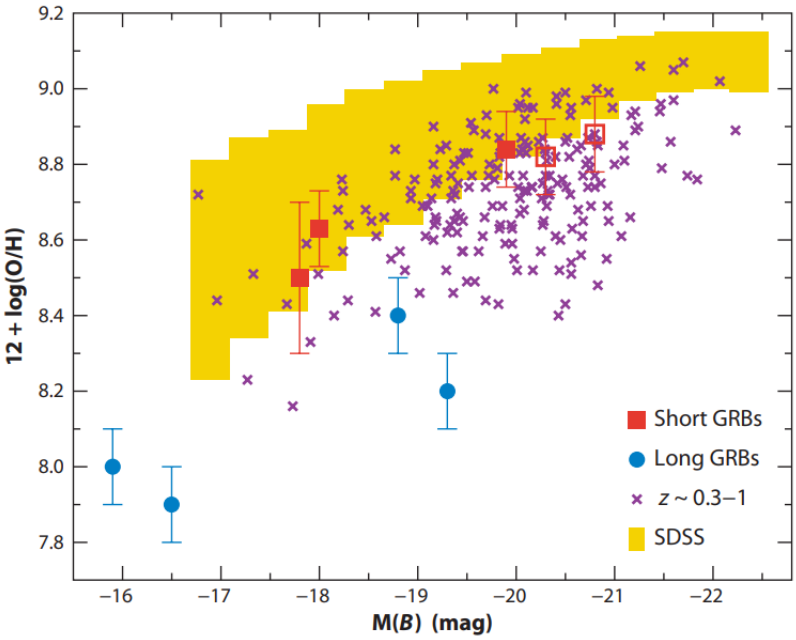

Figure 1.9: *Metallicity as a function of B-band absolute magnitude for the host galaxies of short (red) and long (blue) GRBs. The yellow bars mark the 14–86 percentile range for galaxies at $z \sim 0.1$ from the Sloan Digital Sky Survey, whereas crosses designate field galaxies at $z \sim 0.3$–1. Both field samples exhibit a clear luminosity-metallicity relation. The long GRB hosts tend to exhibit lower than expected metallicities, whereas the hosts of short GRBs are in excellent agreement with the luminosity-metallicity relation (Gehrels et al., 2009).*

This aligns with observations that the GRB rate increases with redshift more rapidly than the cosmic star-formation rate, creating an offset between the true star-formation rate and that traced by GRBs.

For short GRBs, afterglow observations revealed a connection with regions of low star formation, either in elliptical galaxies or in specific regions of galaxies where star formation is minimal. Thanks to the precise localization of these GRBs, three distinct classes of hosts were identified (Gehrels et al., 2009):

- Low-redshift ($z < 0.5$), high-mass ($L \sim L^*$) early-type host galaxies and galaxy clusters;
- Low-redshift, sub-L^* late-type galaxies;
- Faint star-forming galaxies at $z \sim 1$, resembling the hosts of long-duration GRBs.

1.4 GRB physics and progenitors

The observational discoveries briefly outlined in the previous chapters, gathered by the cited space missions and others not explicitly mentioned, must be considered when developing a physical model aimed at explaining the origin and the properties of gamma-ray bursts. Moreover, they serve as valuable constraints for ruling out invalid theories. Currently, there is a widely accepted "Standard Model" for GRBs, though it still presents gaps and unresolved issues. Firstly, it is crucial to identify the type of object and physical processes involved in releasing such enormous amounts of energy, referred to as a *central engine*.

Since GRBs are produced at cosmological distances, their observed fluxes imply a tremendous energy release within a few seconds, reaching up to 10^{54} erg, assuming isotropic emission, which corresponds to 10^{47} J[1]. Such a value is comparable to the conversion of an entire solar mass into γ-ray radiation on a timescale of just a few seconds, and it is several orders of magnitude larger than the energy released by a supernova. However, GRB emissions are highly collimated into two oppositely directed jets (Gehrels et al., 2009), driven by magnetohydrodynamic processes, originating from the central engine, with opening angles ranging from 2 to 20 degrees[2]. Consequently, the radiated energy becomes

$$E_{\rm obs} = E_{\rm iso}(\Omega/4\pi)$$

where Ω is the solid angle of the jet. This collimation reduces the total energy emitted to a value comparable to that of a supernova, approximately 1/2000 of a solar mass converted into radiation within a few seconds.

The isotropic energy of GRBs from the earliest stellar population (Population III, $M > 100 M_{\odot}$) could be even higher, reaching up to 10^{57} erg with duration larger than 10^4 s. If such a large energy release were observed at high redshift ($z = 20$), it would provide compelling evidence for the existence of these primordial, very massive stars (Toma et al., 2012).

GRBs show variability on the characteristic timescale Δt of milliseconds, which can be used as a constraint on the source size R. Variations occurring on timescales shorter than the light-crossing time of the source will be smeared out due to propagation delays within the emitting region. Consequently, the relation $R < c\Delta t$ implies typical emitting regions with sizes of the order of $\sim 10^3$ km, where $10^{50} - 10^{54}$ erg must be released within a few seconds. The release of such enormous energies within a very small volume suggests the formation of a *fireball* composed of e^+, e^-, γ. Such fireball powers the two

[1] $1\,\mathrm{J} = 10^7\,\mathrm{erg}$.

[2] The collimation of GRBs suggests that the actual number of such events in the universe should be significantly higher than what we estimate from our observations, even accounting for the sensitivity limits of our detectors. This occurs because most jets will "miss" Earth and will never be observed; only a small fraction of the total are randomly aligned toward our planet in a way that allows us to detect them as γ-ray bursts.

opposite jets. This scenario leads to the conclusion that GRBs are likely associated with mass-accreting disks around compact objects. More precisely, this arises in two contexts: the explosive end of a massive star and the merger of binary compact stellar remnants, such as black holes and neutron stars. The remnant of these catastrophic events is in any case a spinning black hole with an accretion disk or torus[3] formed from the remaining debris (Fig. 1.10). This structure provides the gravitational energy necessary to power the GRB, as material from the disk or torus falls onto the black hole. Additionally, the presence of a spinning black hole is crucial for creating a matter-free region, enabling the formation and escape of a jet.

An alternative scenario involves a pulsar-like central engine: the accretion occurs onto a rapidly spinning (period $P \sim 1$ ms), highly magnetized (up to $10^{14} - 10^{15}$ G on the surface) neutron star, called *fast magnetar*, or *magnetars*, when it is spinning down. Here, the jets are magnetically driven rather than powered by neutrino annihilation. The maximum energy that can be extracted is given by the rotational energy (Frontera, 2024):

$$E_{\rm rot} \approx \frac{1}{2} I \Omega^2 \approx 2 \times 10^{52} \frac{M}{1.4 M_\odot} \left(\frac{R}{10^6\,{\rm cm}} \right)^2 \left(\frac{P}{1\,{\rm ms}} \right)^{-2} {\rm erg}$$

where I is the moment of inertia, Ω the angular velocity, M and R the mass and the radius of the neutron star. These magnetars, due to their intense rotation and magnetic field dynamics, can generate large-scale magnetic structures and highly magnetized relativistic winds. If the energy released by a GRB is higher than that given by $E_{\rm rot}$, this mechanism can be ruled out.

1.4.1 Standard Model for GRBs

The concept of a fireball composed of e^+, e^-, γ, introduced for the first time by Cavallo and Rees (1978), comes out when huge amounts of energy are released within a very small volume and are suddenly converted into high-energy (MeV) photons.

Pair creation is an efficient way to suppress photons above ∼MeV; however, the high fluxes observed at such energies suggest that the emission originates from regions with a low photon density, where pair production is inefficient. Such low photon density is explained by relativistic expansion and baryon contamination of the fireball. The fireball is generated thanks to the annihilation of neutrino and antineutrino pairs above the accretion disk of a recently formed black hole. In the innermost, hottest regions of the disk, neutrino cooling becomes highly efficient, facilitating the process. Initially, the

[3]The torus is a structure of dust and molecular gas that surrounds an active black hole and its accretion disk. It is responsible for the obscuration, absorption, and re-emission of the radiation emitted by the disk. Several models have been developed to describe its distribution (Elitzur, 2006).

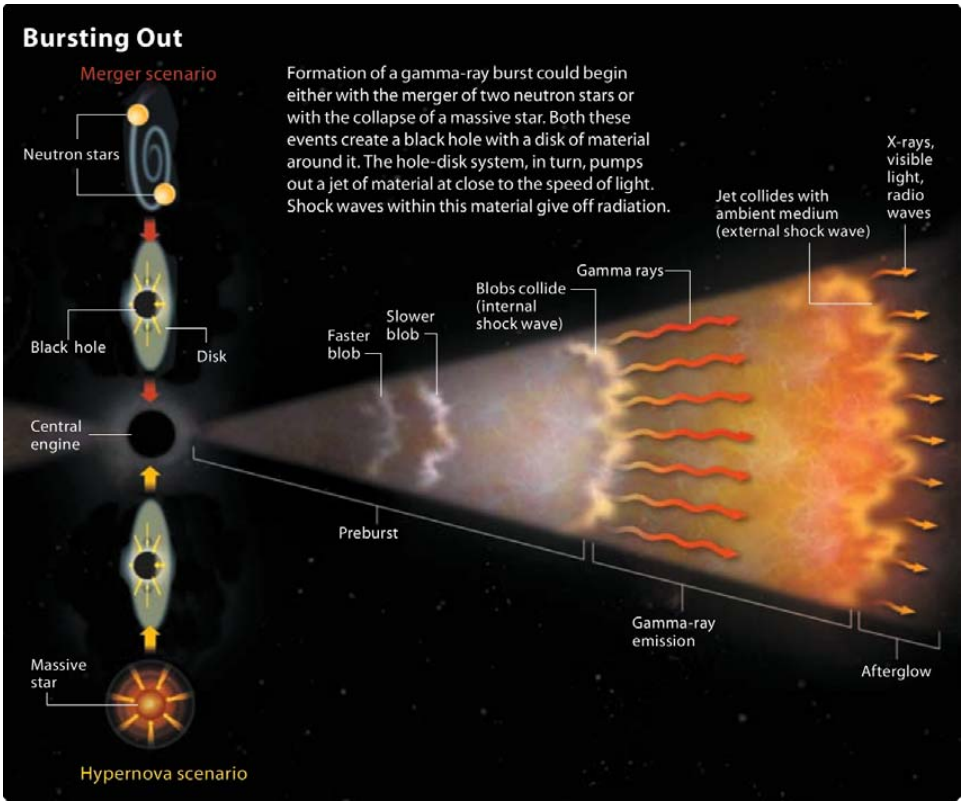

Figure 1.10: *Illustration of the various step of the basic Standard Model with the internal and external shocks and the various radiations they emit. On the left the two main scenarios, both collapsar and merger of compact objects which lead to a central black hole surrounded by a disk are indicated (Vedrenne and Atteia, 2009).*

fireball consists of electron-positron pairs in thermal equilibrium, but as it expands, pairs fall out of equilibrium and recombine.

As described, e.g., in Vedrenne and Atteia (2009), the highly relativistic expansion alters the emitted radiation, causing a blueshift of the observed photons and a shortening of the observed timescales. The optical depth and the rate of pair creation thus are largely decreased: in the moving source frame, the photons are softer by a factor Γ (the Lorentz factor of the relativistic flow [4]), and have lower density due to variable sizes of $\Gamma^2 c\Delta t$; finally, only a small fraction $1/\Gamma$ of the source can be observed due to the relativistic beaming. Calculations show that with Lorentz factors $\sim$100, the pair opacity is below unity before the fireball starts to radiate a significant fraction of its energy.

However, such dense source must be extremely opaque to pair creation ($\gamma + \gamma \rightarrow e^+ + e^-$) so that the radiation emitted when the outflow becomes optically thin would

[4]the Lorentz factor is given by $\Gamma = 1/\sqrt{1 - \frac{v^2}{c^2}}$.

be expected to exhibit a thermal spectrum. Instead, observations reveal a non-thermal power-law spectrum. Moreover, the photon escape timescale would correspond to the time when the outflow becomes optically thin, measured in milliseconds, far shorter than the observed GRB durations. To avoid these problems, Meszaros and Rees (1993) introduced for the first time a fireball shock model with *external shocks* and *internal shocks*, adding some baryon contamination: interactions between baryons and the fireball medium generate relativistic shocks. Shocks convert bulk kinetic energy into internal energy, producing non-thermal radiation and particles, through adiabatic processes. The abundance of electrons within the medium accelerates the shocks and facilitates energy radiation via synchrotron or synchrotron-Inverse Compton (IC) processes.

As the fireball accelerates during expansion, a rarefaction wave propagates inward. At a critical point, the fireball becomes optically thin to Compton scattering, allowing radiation to escape as the GRB. Meanwhile, the external medium is swept outside the contact discontinuity in the external shock wave, which effectively describes the observed multi-wavelength afterglow. As more material accumulates, the fireball expansion begins to decelerate, concentrating matter in a thin shell. This deceleration triggers a secondary, more energetic emission burst. Between the interface of the fireball material and the external shock, the gas is heated, and as deceleration progresses, a reverse shock propagates inward into the fireball ejecta.

These shocks arise in the fast-moving ejecta when the variable outflow from the central engine causes the ejection of successive shells with different Lorentz factors. When faster shells overtake slower ones, multiple shocks are produced. The primary burst is observed as the matter within the blast wave shell cools. This process effectively accounts for the rapidly fluctuating light curve characteristic of the prompt emission. This internal-external shock model does not depend on the nature of the central source, namely whether it is due to the coalescence of compact objects or to a collapsar produced by the explosion of a supermassive star.

1.4.2 Collapsar

Collapsars are defined as rotating massive stars whose iron core collapses directly into a black hole. This accretes surrounding matter and emits a powerful relativistic jet, producing the observed GRB (Gehrels et al., 2009; Vedrenne and Atteia, 2009; Mészáros, 2019). Three primary conditions are required in the formation of a collapsar according to the model: *a*) a star with a massive core; *b*) the removal of the hydrogen envelope; *c*) high angular momentum in the core to sustain a transient torus around the remnant. These characteristics align well with Wolf-Rayet stars, which are also linked to the progenitors of type Ib/c supernovae. The formation of the black hole may occur either promptly, as the collapse of the iron core fails to generate an outward shock (type I collapsar), or via fallback in a mild explosion (type II collapsar).

In the type I collapsar scenario, the progenitors of long GRBs are stars with masses ex-

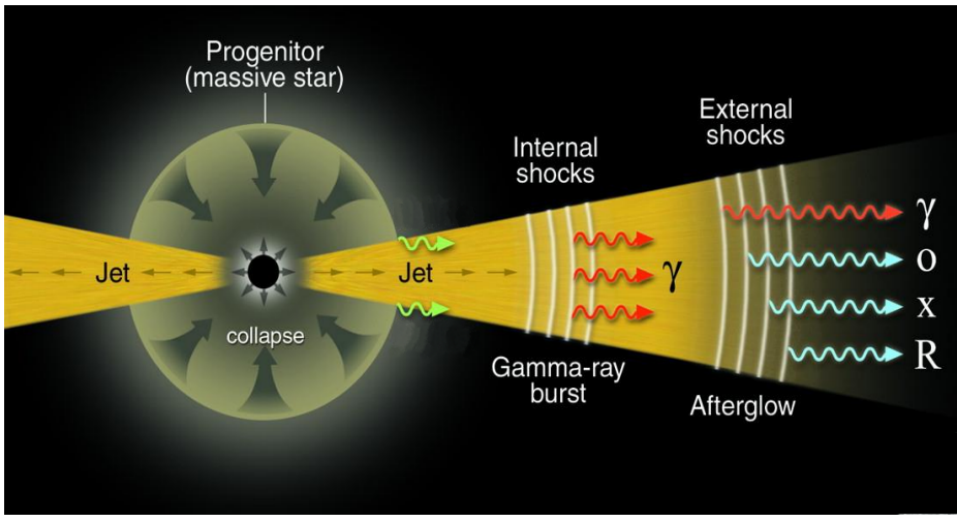

Figure 1.11: *The standard GRB fireball shock model from a collapsar, showing the photosphere, internal shock and external shock resulting in the afterglow (Mészáros, 2019).*

ceeding 35–40 $M_\odot$ that have lost their hydrogen envelopes before their death (Fig. 1.11). These stars, during the main sequence, can develop helium cores of 9–14 $M_\odot$ and undergo a two-step collapse: first, the Fe core collapses into a neutron star, followed by its direct collapse into a black hole surrounded by a massive accretion disk. This system known as "failed supernova" acts as a reservoir of gravitational energy that powers the GRB. A supernova does not occur in this case because the outward shock is unable to form prior to disk formation. The infall of matter along the rotational axis and stagnation in the equatorial plane create a low-density polar region, enabling energy dissipation in the disk via neutrino annihilation. This process powers the relativistic outflow of jets along the polar axis. Additionally, strong magnetic fields within the disk contribute to magnetohydrodynamic energy dissipation.

As the jet drills through the stellar material, the matter at the jet head heats up and forms a hot "cocoon". This cocoon exerts transverse pressure, which confines and further collimates the jet. Once the jet breaks through the star, relativistic material is expelled and collides with the winds previously emitted, leading to the formation of a soft GRB. The GRB itself becomes observable only after the jet clears the outer stellar layers, allowing relativistic plasma to escape.

Typically, the GRB originates at distances of $10^{14} - 10^{15}$ cm from the progenitor star, with emission beginning about 10 seconds after the black hole forms, as the jet dissipates its kinetic energy and produces gamma-ray radiation (prompt emission). Subsequently, at a distance of $10^{16} - 10^{17}$ cm the jet interacts with the interstellar medium, decelerating and generating synchrotron emission across X-ray to radio wavelengths, which constitutes the afterglow.

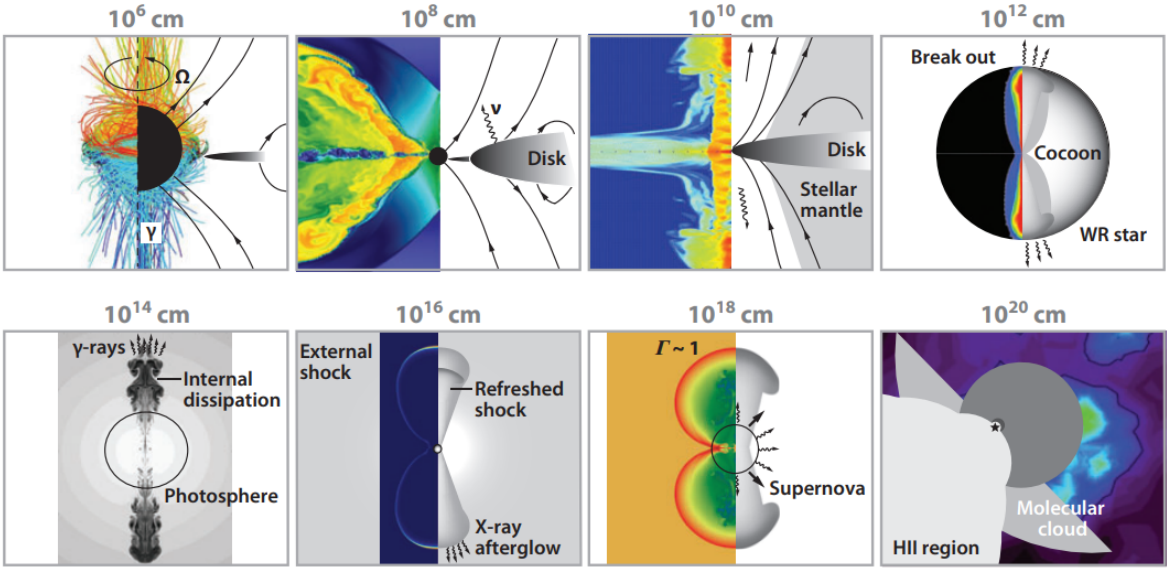

Figure 1.12: *Model for the production of a GRB from collapsar. At scales of* 10^6 *cm the GRB nucleus and its magnetosphere are shown. At* 10^8 *cm the accretion flow is likely to be embedded in a very active corona. Relativistic outflow from the black hole is focused into two jets. At* 10^{10} *cm some beaming is expected because energy would be channeled preferentially along the rotation axis. The majority of stellar progenitors will not collapse entirely during the typical duration of a GRB. A stellar envelope will thus remain to impede the advance of the jet. At* 10^{12} *cm typical size of an evolved massive star progenitor. A thermal break-out signal should precede the softer* γ*-rays observed in GRBs.* 10^{14} *cm is the most favorable region for shocks is across the jet profile, where velocity differences lead to highly variable* γ*-ray light curves. At* 10^{16} *cm the external shock becomes important when the inertia of the swept-up external matter starts producing an appreciable slowing down of the ejecta. At* 10^{18} *cm* $\sim$ *1 pc the end of the relativistic phase happens when the mass* E/c^2 *has been swept-up (Gehrels et al., 2009).*

Variability in the burst arises from instabilities in the accretion rate, leading to energy deposition fluctuations. This dynamic promotes GRB production through internal shocks as successive shells of ejected material interact. The succession of the main phases for the production of a GRB is summarized in Fig. 1.12.

The type II collapsar scenario involves the formation of a black hole following a mild supernova explosion. In this case, the outgoing shock cannot expel helium and heavier elements beyond the neutron star. The resulting fallback of this material leads to the delayed formation of a black hole surrounded by a torus, similar to the type I scenario. This mechanism applies to stars with masses between 20–40 $M_\odot$, indicating that type II

collapsar may be more frequent than type I. In this case, the energy of the jet depends on the efficiency of magnetohydrodynamic processes in extracting energy from the disk and black hole.

In conclusion, collapsar progenitors are expected to reside in star-forming regions where massive stars form and evolve. Notably, this model does not account for GRBs with durations shorter than approximately 5 seconds (Vedrenne and Atteia, 2009).

1.4.3 Binary mergers

Both the collapsar model and the mergers of compact binary systems result in the formation of a black hole surrounded by a transient accretion disk or torus. Coalescing compact binaries with electromagnetic counterparts include neutron star-neutron star (NS-NS) and neutron star-black hole (NS-BH) systems. They are associated with low star formation rate galaxies ($\leq 1 M_{\odot}\, yr^{-1}$), or elliptical galaxies.

NS-BH mergers can lead to the formation of a more massive black hole with an accretion disk only if the neutron star is disrupted outside the black hole innermost stable circular orbit (ISCO). NS-NS mergers can result in the formation of either a black hole, a stable neutron star, or, in most cases, a metastable neutron star that eventually collapses into a black hole. Electromagnetic emissions may be absent in cases where a black hole is formed promptly without leaving behind an accretion disk or ejected material in NS binary mergers. Similarly, in NS-BH mergers, no emission is observed when the neutron star is swallowed totally without being tidally disrupted (Fig. 1.13).

As for long GRBs, an accreting black hole in these systems can act as a central engine, powering a relativistic jet. Such systems harbor a huge reservoir of gravitational binding energy. Strong centrifugal forces clear the polar region, forming a low-density area. Energy release into this region generates a radiation-dominated plasma, which propagates outward, piercing through the circumburst medium formed by material previously ejected during the merger. In these systems, the two primary energy reservoirs are the gravitational binding energy of the disk/torus and the spin energy of the black hole.

Compact binary coalescences (CBCs) are known to emit a range of electromagnetic signals across the spectrum, from radio waves to gamma-rays. Additionally, they are significant sources of gravitational waves (GWs). Since the first GW detection in 2015 from a binary black hole merger, tens of additional stellar-mass black hole coalescences have been observed. Notably, two confirmed binary neutron star mergers and two confirmed (plus one potential) NS-BH mergers have been detected by the Advanced LIGO and Advanced Virgo detectors (Abbott et al., 2017). These observations affirm the expectation that CBCs are the most frequent GW sources detectable at high frequencies, where ground-based detectors are sensitive (approximately 10 Hz to a few kHz). Such detections enable valuable opportunities for multi-messenger astrophysics. The first GW detection of a neutron star-neutron star merger occurred on August 17, 2017, and was accompanied

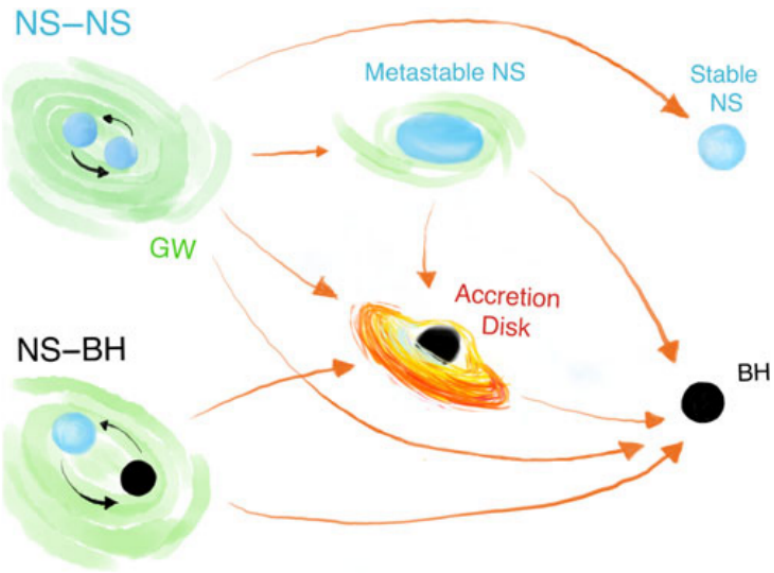

Figure 1.13: *Different scenarios for a NS–NS and a NS–BH merger and the merger remnant. The EM radiation is expected when an accretion disk and unbound mass are left outside the merger remnant (Ascenzi et al., 2021).*

by the short GRB (GRB170817A), the optical/infrared kilonova (AT2017gfo), as well as additional X-ray, optical, infrared, and radio emissions (Troja et al., 2017). This event provided a remarkable demonstration of the insights achievable by combining GW data with electromagnetic observations. A key astrophysical implication of joint detections of short GRBs and GWs, particularly from BH-NS mergers, is the confirmation that these systems are progenitors of at least a subset of GRBs (Fig. 1.14).

1.5 Cosmology and open problems

As highlighted in the review by Frontera (2024), GRBs as highly energetic transients produce distinct electromagnetic radiation across a wide range of frequencies, making them detectable over vast cosmic distances and invaluable for both astrophysical and fundamental physics studies. GRB studies play a crucial role across various branches of astrophysics. Below, the primary significance and applications of GRBs are outlined:

- Thanks to their extraordinary luminosity, GRBs can be observed at very high redshifts, making them an excellent probe for studying the early universe. In particular, they are crucial in probing the formation and evolution of the first collapsed structures, including Population III and early Population II stars. These events shed light on the epoch of the first star formation and their subsequent impact on

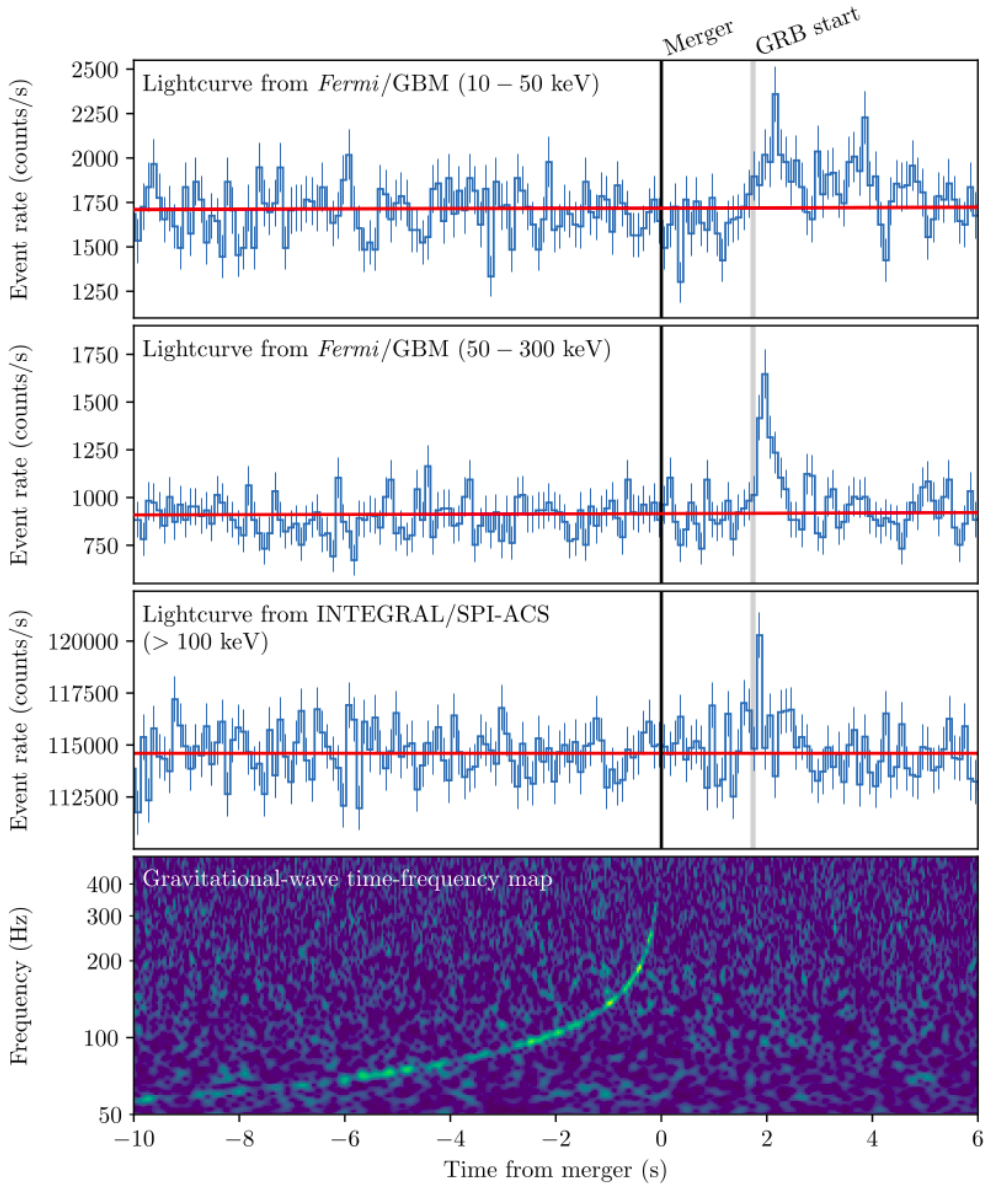

Figure 1.14: *Joint multi-messenger detection of GW170817 and GRB170817A. First: the summed GBM lightcurve for GRB170817A between 10 and 50 keV. The background estimate is overlaid in red. Second: the same as the top panel but in the 50—300 keV energy range. Third: lightcurve with the energy range starting approximately at 100 keV and with a high energy limit of least 80 MeV. Fourth: the time-frequency map of GW170817 was obtained by coherently combining LIGO-Hanford and LIGO-Livingston data. All times here are referenced to the GW170817 trigger time (Abbott et al., 2017).*

the surrounding environment, particularly their contribution to the reionization of the intergalactic medium. High-z GRBs also enable the extension of the Hubble diagram well beyond the redshift range accessible with Type-Ia Supernovae, providing an additional tool to rigorously test the ΛCDM cosmological model and its associated parameters (Moresco et al., 2022).

- Given their cosmological distances, GRBs serve as a unique laboratory to address several outstanding questions in fundamental physics including: test of the Lorentz invariance violation expected is some theories of quantum gravity; investigation of the BH physics through signatures in the timing properties of GRB prompt emission; studying theories of gravity beyond general relativity, with the association of GW event; the existence of axion-like particles (ALPs) and their photon oscillations can be tested using GRBs, as their cosmological distances allow the observation of high-energy γ-ray photons over vast scales.

- GRBs, driven by ultra-relativistic shocks with Lorentz factors of several hundreds, significantly higher than those of other potential accelerators like blazars, are considered prime candidates for accelerating particles to the extreme energies observed in cosmic rays. By analyzing their spectra, the energy distribution of these accelerated particles can be constrained.

- GRBs are also considered key contributors to the observed UHECRs and high-energy neutrinos due to the intense shock acceleration driven by the newly formed compact object. Low-luminosity GRBs, in particular, are expected to play a significant role in the production of high-energy neutrinos.

- The first GRBs and supernovae may also play a crucial role in the generation of the first cosmic magnetic fields. As mass is lost, for example through stellar winds, magnetic flux could be dispersed alongside heavy elements. The widespread presence of heavy elements in the Lyα forest suggests significant diffusion from the sites of early supernovae, and magnetic flux may have spread in a similar manner. This flux, stretched and sheared by large-scale motions, could serve as the "seed" for subsequent amplification processes, leading to the large-scale magnetic fields that permeate disc galaxies.

- In addition to providing insights into high-redshift star formation regions, each of these bursts has the potential to constrain the local element abundances in its host galaxy—data that would otherwise be unattainable until the development of telescopes larger than 20 meters in diameter. Even more compelling, each burst offers a unique opportunity to probe the extent of intergalactic reionization at its specific redshift and along its line of sight.

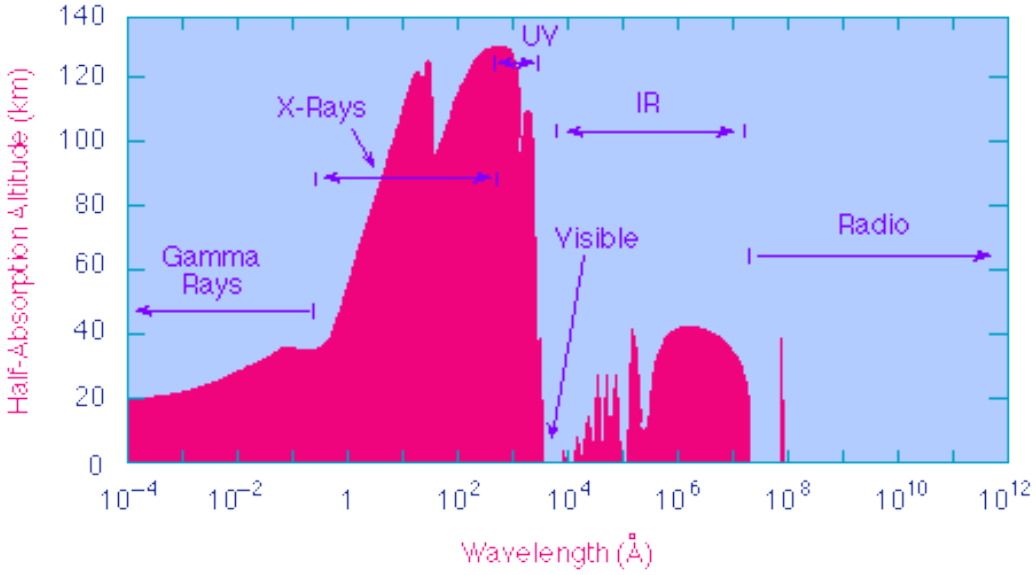

Figure 1.15: *Amount of absorption at different wavelengths in the atmosphere expressed in terms of half-absorption altitude, defined as the altitude where 1/2 of the radiation of a given wavelength incident on the upper atmosphere has been absorbed. Atmospheric windows correspond to visible and radio frequency; X-rays and UV are strongly absorbed soon in the upper layers of the atmosphere, while Gamma Rays and IR in the lower ones (Credits: Atmospheric Windows).*

- By deriving a method to determine the burst luminosity independently of redshift distance, GRBs can be used as standard candles, allowing for the determination of the cosmic expansion history of the Universe at higher redshifts than is possible with supernovae.

1.6 Current and future observatories from space and ground

Observations in the far-UV, X-ray, and γ-ray bands, corresponding to wavelengths below 300 nm and energies above 0.1 keV, must be conducted from above the atmosphere. This is because the atmosphere is opaque to radiation due to the presence of ozone, molecular gases, and photoelectric absorption by atmospheric atoms (Fig. 1.15).

Along with the previously mentioned missions, a multitude of other space missions contribute to the study and data collection on GRBs. Moreover, various ground-based facilities have made significant contributions to GRB research, and more in general to high-energy astrophysics. We highlight the most notable in the following:

- AGILE (Tavani et al., 2009), Astro-Rivelatore Gamma a Immagini Leggero, high-energy Italian mission launched in 2007 and de-orbited in February 2024. It was capable of detecting and monitoring gamma-ray sources across a wide field of view ($\sim$1/5 of the whole sky). The instruments onboard AGILE included GRID, Gamma-Ray Imaging Detector (30 MeV–50 GeV), MCAL, Mini-Calorimeter, and the Super-AGILE detector, all surrounded by a plastic scintillator Anticoincidence System for background particle identification.

- The Fermi Gamma Ray Observatory (Atwood et al., 2009), launched on 11 June 2008 and still operational, is the result of a collaboration between NASA and ASI.It has two main instrument: the Large Area Telescope (LAT, 20 MeV–300 GeV), and a Gamma-ray Burst Monitor (GBM, 8 keV–40 MeV).

- INTEGRAL (Winkler et al., 2003), International Gamma-Ray Astrophysics Laboratory. It was launched by the European Space Agency into Earth orbit in 2002 and was designed to provide fine imaging (12 arcmin FWHM angular resolution) and fine spectroscopy ($E/\Delta E = 500$) of celestial gamma-ray sources in the energy range 15 keV–10 MeV, with concurrent source monitoring in the X-ray (4–35 keV) and optical (V-band, 550 nm) energy ranges.

- IXPE (Deininger et al., 2023) is a NASA–ASI Small Explorers (SMEX) collaborative mission, launched on December 2021 aboard a SpaceX Falcon-9 rocket. The goal of the mission is measuring the X-ray (2–8 keV) polarization from neutron stars, black holes, active galactic nuclei (AGN) and angular resolved polarimetry for the brightest extended sources like supernova remnants (SNRs), pulsar wind nebulae (PWNe) and large-scale jets in AGN.

- MAGIC (Lorenz, 1996) and H.E.S.S, (H.E.S.S. Collab et al., 2021) Cherenkov telescopes focus on Very High Energy (VHE, >100 GeV) afterglow emission.

The present facilities are currently engaged in addressing the issues mentioned above. Below, some future missions and projects aimed at better addressing the open questions related to GRBs are outlined:

- The Transient High Energy Sky and Early Universe Surveyor, THESEUS (Amati et al., 2018), a mission approved by ESA for a Phase A study with a planned launch in 2035, will carry three instruments. These include a Soft X-ray Imager (SXI, 0.3—5 keV) and an X-ray Gamma-ray Imaging Spectrometer (XGIS, 2 keV–10 MeV) for GRB detection and localization, both with large fields of view. Additionally, it features a 70 cm InfraRed Telescope (IRT, 0.7–1.8μm) for identifying GRB IR counterparts and determining their redshifts, with limited spectroscopic capabilities ($R \approx 400$). See below for details.

- Two recently launched space missions are set to significantly advance GRB studies in the X-ray and gamma-ray energy bands. The Einstein Probe (EP; Yuan et al. 2015), a Chinese-led mission with international collaboration, launched on 9 January 2024, focuses on exploring GRBs in the relatively under-studied X-ray band. It features two instruments: the Wide-field X-ray Telescope (WXT), employing lobster-eye optics for transient surveys, with a large FOV ($60° \times 60°$) and a pass-band of 0.5–4 keV; and the Follow-up X-ray Telescope (FXT), comprising two units with Wolter I optics, a narrow FOV ($1° \times 1°$). The SVOM mission (Space-based multi-band astronomical Variable Objects Monitor; Götz et al. 2009), launched on 24 June 2024, is a Chinese–French collaboration designed for GRB detection across a broad energy range. It carries multiple instruments: the Gamma-ray Monitor (15 keV–5 MeV), the X-ray imaging and triggering telescope ECLAIRs (4–150 keV), the lobster-eye Microchannel X-ray Telescope (MXT, 0.2–10 keV), and an optical telescope. Moreover, the development of SVOM technology will be adopted by the THESEUS mission, increasing its Technology Readiness Level (TRL) and serving as a true pathfinder for THESEUS (Cordier et al., 2018).

- In the gravitational wave field, two large experiments have been recently approved: the ESA-NASA mission eLISA (Laser Interferometer Space Antenna; Amaro-Seoane et al. 2017), foreseen to be launched in the early 2035s, and the Einstein Telescope, a European ground facility, still awaiting a final location decision.

- Several large-scale neutrino detection facilities are currently operational. These include the underwater telescope ANTARES (Astronomy with a Neutrino Telescope and Abyss environmental REesearch project; Montaruli 2002) and the ICECUBE Neutrino Observatory (Aartsen et al., 2017). Additionally, a next-generation neutrino observatory, the KM3NET (Cubic Kilometre Neutrino Telescope; Katz 2006), is under development.

- In the Very-High-Energy (VHE) gamma-ray field, there are already several operational facilities, like VERITAS (Very Energetic Radiation Imaging Telescope Array System; Holder et al. 2006) LHAASO (Large High Altitude Air Shower Observatory; Vernetto et al. 2016). In addition, a very large project is under development: CTA (Cerenkov Telescope Array; CTA Consortium 2010).

- Also, new radio facilities are under development, particularly the Square Kilometer Array SKA (Dewdney et al., 2009), that will be the largest radio telescope in the world.

- Among the future optical facilities: the European Extremely Large Telescope (EELT; Gilmozzi and Spyromilio 2007), the US Thirty Meter Telescope (TMT;

Sanders 2013), the American Giant Magellan Telescope (GMT; Johns 2006) and the Vera Rubin Observatory (Brough et al., 2020).

- NewAthena (New Advanced Telescope for High Energy Astrophysics; Cruise et al. 2024) is the next ESA Large X-ray observatory to be launched in the second half of 2030s.

The focus of this thesis is precisely on the THESEUS mission, whose design concept will be extensively explored in the upcoming chapters, alongside an analysis of the performance of the XGIS instrument. The mission will open a new window on the early Universe through the detection of high-redshift GRBs. In the next decade, the vast array of facilities presented will reach their peak capabilities and scientific return, particularly when working in synergy. By providing complementary information, they will both respond to THESEUS discoveries and generate triggers for THESEUS, turning it into a true cornerstone for multi-messenger astrophysics (Fig. 1.16).

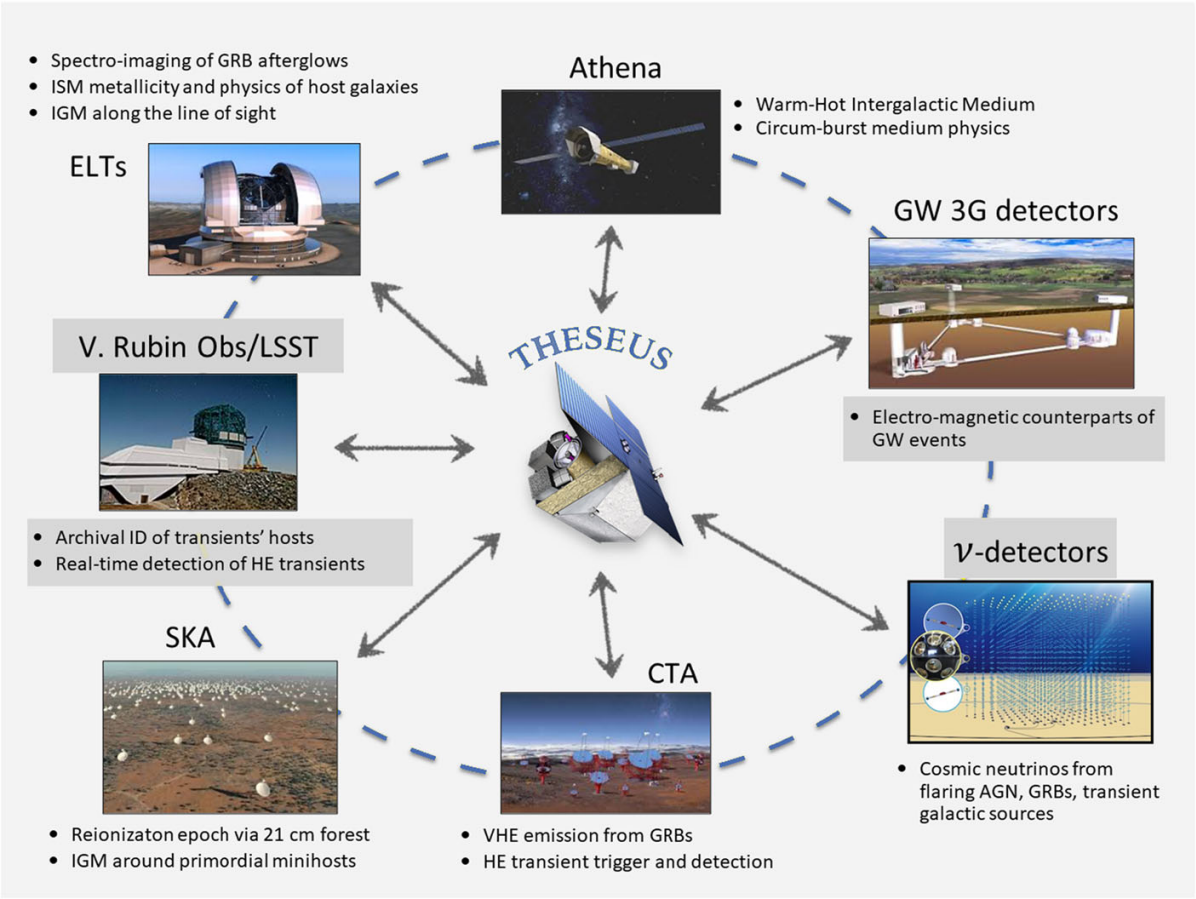

Figure 1.16: *THESEUS will work in synergy on a number of themes with major multi-messenger facilities in the 2030s and will provide targets and triggers for follow-up observations with these facilities (Amati et al., 2021).*

Chapter 2

THESEUS: ESA M7 space mission candidate

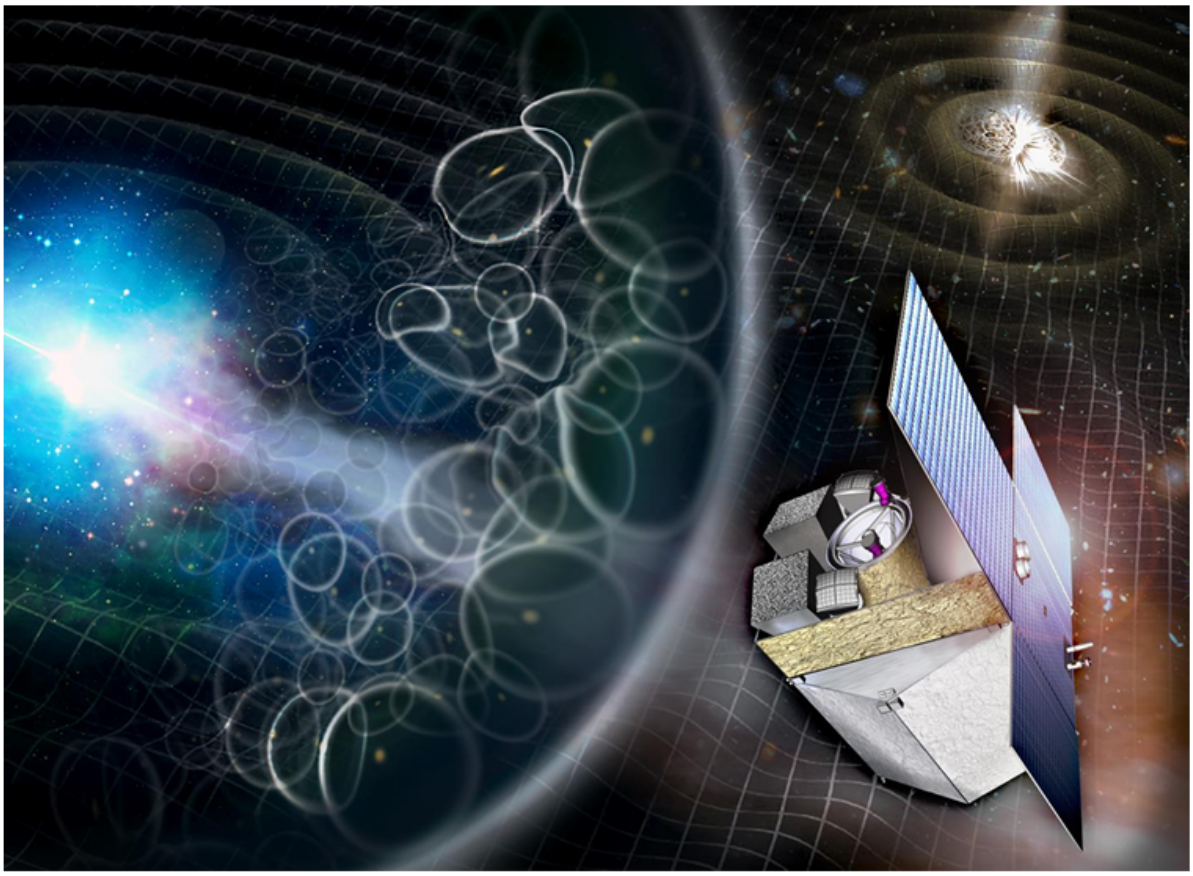

THESEUS (*Transient High-Energy Sky and Early Universe Surveyor*) is an ambitious space mission concept developed by a European collaboration and initially proposed to the European Space Agency (ESA) in 2016 for the M5 mission opportunity within the Cosmic Vision Programme (European Space Agency (ESA), 2021; Amati et al., 2018, 2021). Coordinated by Italy, with the United Kingdom, France, Switzerland, and Germany as co-leads, the THESEUS consortium includes contributions from numerous other ESA member states. Its members are responsible for delivering the payload and science ground segment; the final goal is to address fundamental questions about the early Universe and high-energy transient phenomena.

In 2018, THESEUS was selected alongside SPICA (Sibthorpe et al., 2015) and EnVision (Ghail et al., 2017) for a three-year Phase A assessment study to evaluate its scientific and technical feasibility. Although EnVision, a mission dedicated to studying the planet Venus, was ultimately chosen in 2021 as the M5 mission, THESEUS was reconsidered following the ESA M7 mission call in November 2023. It was endorsed, along with M-Matisse (Zinzi et al., 2016), a mission focusing on Mars habitability and evolution, and Plasma Observatory (Marcucci et al., 2023), designed to study the Earth plasma environment, for a detailed Phase A study.

In mid-2026, one of these three mission concepts will be selected to proceed to the Definition Phase, becoming ESA next Medium-class mission for a foreseen launch in the mid-2030s. The selected mission will join the current list of ongoing ESA Cosmic Vision missions, including Solar Orbiter (Marirrodriga et al., 2021), Euclid (Racca et al., 2016), PLATO (Miglio et al., 2017), and ARIEL (Pascale et al., 2018), the latter two of which are still in the development phase.

In this chapter, a broad and non-exhaustive overview of the mission design, scientific objectives, and payload is presented.

2.1 The mission concept

THESEUS has been designed firstly to fulfill three top-level science requirements. The first concerns exploiting the unique and breakthrough potentialities of GRBs for investigating the Early Universe, the second is focused on advancing Multi-Messenger Astrophysics, and the third is the exploration of high-energy transient phenomena across the entirety of cosmic history (Amati et al., 2021). The primary scientific goals of the mission are aligned with the Cosmic Vision program (Turon, 2006), ESA strategic scientific plan for the 2015-2025 decade, in particular within the theme of the Early Universe. THESEUS will address the fundamental question, *"How did the Universe originate and what is it made of?"* and will also make substantial contributions to the themes of *"The Gravitational Wave Universe"* and *"The Hot and Energetic Universe"*.

This will be achieved by a payload and mission profile (see Fig. 2.1, and Amati et al. 2018) providing an unprecedented combination of:

1. wide and deep monitoring of the high-energy sky across a very broad energy band, provided by the *X/Gamma-ray Imaging Spectrometer* (XGIS): a set of two coded-mask cameras using monolithic SDD+CsI(Tl) X-,γ-ray detectors, with a $\sim$2 sr imaging FoV and a source accuracy $<15'$ in 2–150 keV range, covering a total energy band from 2 keV up to 10 MeV and few μs timing resolution;

2. focusing capabilities in the soft X-ray band providing large grasp (product of the effective area and the field-of-view) and high angular resolution, exploiting the *Soft X-ray Imager* (SXI): a set of two "Lobster-eye" telescope units, covering an energy band of 0.3–5 keV and a total FoV of $\sim$0.5 sr with source location accuracy $\leq 2'$;

3. on board NIR capabilities for immediate low-frequency counterpart identification, arcsecond localization and redshift determination, by using the *InfraRed Telescope* (IRT, 0.7–1.8 μm): a 0.7 m class IR telescope with $15' \times 15'$ FoV, imaging (I, Z, Y, J and H filters), and spectroscopic capabilities (resolving power, $R \sim$ 400, through a $2' \times 2'$ grism).

These advanced instruments are complemented by a high degree of spacecraft autonomy and agility (slewing capability $>7^\circ$/min), ensuring rapid response to transient events. Additionally, the mission includes the capability for prompt transmission (within a few tens of seconds) of transient trigger information to ground-based systems, enabling timely and efficient follow-up observations (Amati et al., 2021).

The nominal mission duration is set at 4 years (corresponding to approximately three and a half years of scientific operations), with the possibility of an extension. The mission will use a Vega-C launcher to place the spacecraft into a low-inclination (5.4°) Low Earth Orbit (LEO) at an altitude of 550–640 km. This orbit provides several unique advantages, including maintaining a low and stable background level for high-energy instruments, allowing the exploitation of the Earth magnetic field for rapid spacecraft slewing, and enabling the prompt transmission of transient triggers and positions to the ground. The main ground station for the mission will be located in Malindi, Kenya, provided by Italy.

To address its specific scientific objectives, THESEUS will exploit the observation of both long and short GRBs:

- Long GRBs (see Sect. 1.4.2), associated with the collapse of massive stars, provide an excellent tool for studying star formation and gas physics across all redshifts, extending back to the reionization era. Thanks to their ionizing radiation, GRB progenitors and their host galaxies are very good representatives of the massive stars and star-forming galaxies likely responsible for reionization. Therefore, obtaining a statistical sample of GRBs at $z > 6$ is crucial for independently measuring the cosmic Star Formation Rate (SFR) during the early stages of the Universe. The first generation of metal-free stars (Pop III) and the second generation of massive,

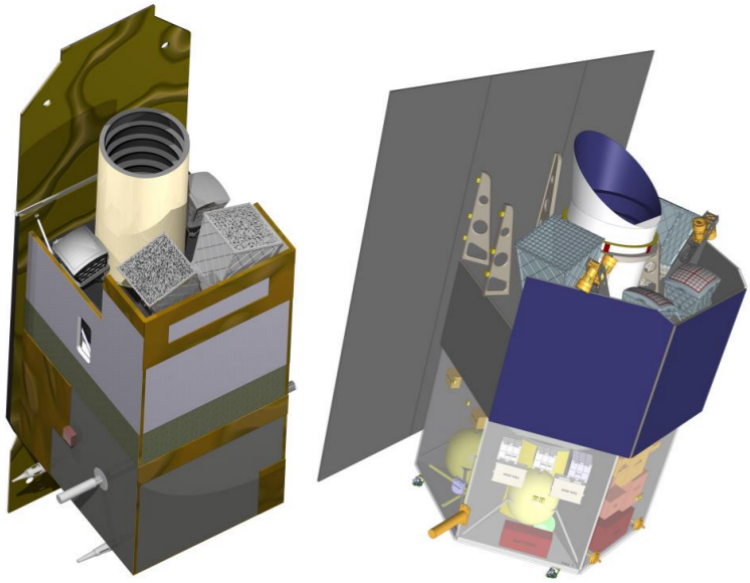

Figure 2.1: *Schematic view of two spacecraft designs, payload accommodation for the Phase A of 2018–2021 provided by Airbus Defence and Space (left) and Thales Alenia Space (right) (European Space Agency (ESA), 2021).*

metal-poor stars (Pop II) can produce powerful GRBs, enabling the identification of these ancient objects, not yet observed, and the study of their host galaxies. Furthermore, the contribution of Pop III stars to the metal enrichment of the first galaxies can be explored by analyzing the absorption features in Pop II GRBs, which are observed in a medium enriched by the first Pop III supernovae (Amati et al., 2018). Simulations show that THESEUS will detect and locate between 40 and 50 GRBs at $z > 6$ over 3.45 years of scientific operations (Fig. 2.2), with photometric redshift accuracy better than 10%, thanks to the identification of Lyman break features shifted to the THESEUS telescope imaging sensitivity range (Amati et al., 2021).

- Short GRBs (see Sect. 1.4.3) are associated with the merger of neutron star binaries which are known to be powerful sources of gravitational waves (Amati et al., 2018). Gravitational wave interferometers currently have limited sky localization capabilities, relying only on triangulation techniques. THESEUS will maximize the science return of the multi-messenger investigation, detecting electromagnetic signals from short GRBs, independently of the GW events (Fig. 2.3). This will enable the localization of GW sources beyond 200 Mpc, which will only be accessible to third-generation detectors expected around 2030 (Stratta et al., 2018).

THESEUS will be built on the successful model of Swift, which has demonstrated

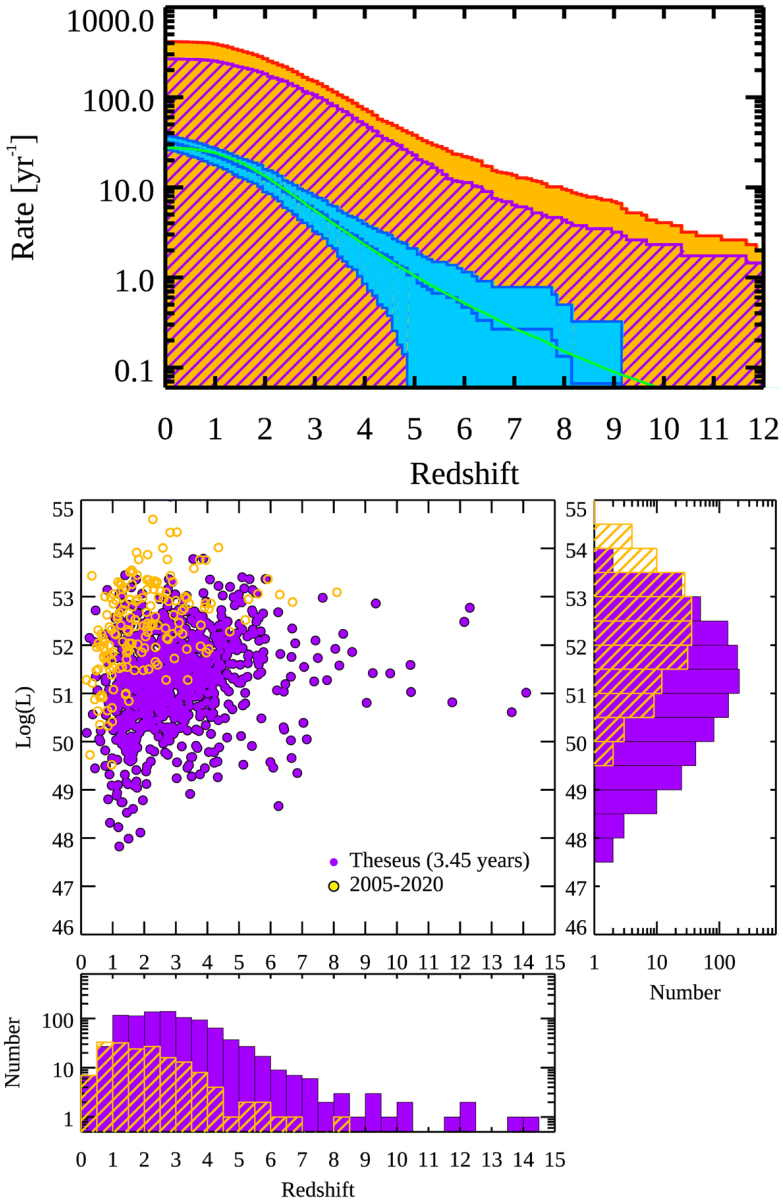

Figure 2.2: *Top Panel: expected detection rate of long GRBs by THESEUS (orange histogram) compared with those whose redshift was measured between 2005 and 2020 (blue area). The purple hatched histogram represents the GRBs for which a determination of the redshift by either THESEUS or ground-based facilities is expected. The green curve represents a model fitting the observed distribution: the THESEUS predictions are based on this. THESEUS will detect between one and two orders of magnitude more GRBs at any redshift with respect to current facilities, and most notably in the high-redshift regime ($z > 6$). Bottom Panel: Distribution of long GRBs with redshift determination in the peak isotropic luminosity versus redshift plane now (yellow points and hatched histogram) and after the nominal operation life of THESEUS (purple points and full histogram) (Amati et al., 2021).*

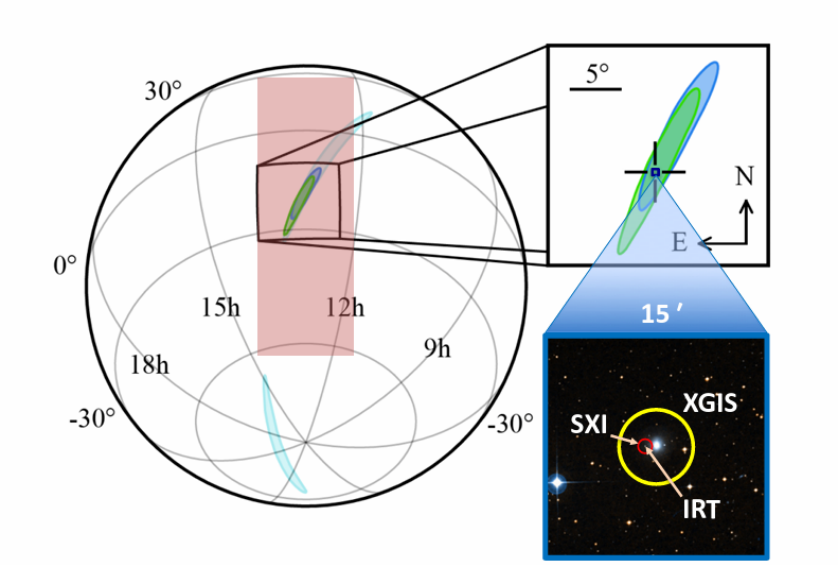

Figure 2.3: *THESEUS/SXI field of view (pink rectangle) superimposed on the probability skymap of GW170817, obtained with the two Advanced LIGO (cyan) and Advanced Virgo (green). THESEUS not only will cover a large fraction of the skymap, but will also localize the counterpart with an uncertainty of the order of 15' with the XGIS and better than 2' with SXI (Stratta et al., 2018)*

Mission	Autonomous rapid repointing	Arcsec localisation	Optical imaging	Near-IR imaging	Near-IR spectroscopy	On-board redshift broadcasting	<10 keV X-ray coverage	>10 keV X-ray coverage	MeV γ-ray coverage
Swift	✓	✓	✓	×	×	×	✓	✓	×
Fermi/GRB	×	×	×	×	×	×	×	✓	✓
Integral	×	×	✓	×	×	×	×	✓	✓
SVOM	✓	✓	✓	×	×	×	✓	✓	✓
Einstein Probe	✓	×	×	×	×	×	✓	×	×
eXTP	✓	✓	×	×	×	×	✓	×	×
THESEUS	✓	✓	✓	✓	✓	✓	✓	✓	✓

Figure 2.4: *GRB detection performance of THESEUS compared with current and upcoming high-energy spacecrafts. Note that, in the case of SVOM, the mission profile includes dedicated robotic telescopes on the ground for granting prompt follow-up of detected transients in the optical and NIR. By the 2030s, THESEUS will be the only facility allowing both the rapid identification of GRBs and the spectral characterization of their optical/NIR counterparts for a sizeable population of bursts at low and high ($z > 6$) redshift Amati et al. (2021).*

the power of rapid on-board localization of high-energy transients. It will also follow other missions, such as SVOM and Einstein Probe (see Sect. 1.6), but will have largely enhanced capabilities for high-redshift and short-hard GRB discovery, and multi-wavelength characterization compared to these other missions, as summarized in Fig. 2.4.

2.2 Scientific objectives and requirements

The first top-level science requirement is exploring the Early Universe down to the Cosmic Dawn and Reionization Era, by unveiling a complete census of the GRB population in the first billion years (European Space Agency (ESA), 2021). A sample that is representative of the parent population on a given redshift range within a certain confidence level is needed in this context. As a quantitative measure of the successful fulfillment of this scientific requirement, THESEUS will be capable, within the nominal mission lifetime in orbit, of detecting and precisely locating, at the arcsecond level, using the IRT, at least 40 long GRBs at $z \gtrsim 6$, corresponding to approximately the first billion years of the Universe in the standard ΛCDM cosmology (Fig. 2.2). The main drivers for this requirement are:

- constraining the slope of the Star Formation Rate (SFR) with an accuracy better than one magnitude on the cut-off magnitude of the galaxy luminosity function;
- ruling out at 95% confidence level the hypothesis that the reionization is sustained by stars if low values of the escape fraction $f_{\rm esc}$ are consistently measured in the host galaxy of fully characterized GRBs detected by THESEUS (this requires at least 30 GRBs with simultaneous determination of the galaxy SFR and of the escape fraction).

THESEUS will open a full new window in the exploration of GRBs with respect to what can be achieved by currently operational observatories such as Swift (in X-rays) or Fermi (in γ-rays), in particular at high redshift, increasing by at least one order of magnitude the number of known GRBs at $z > 6$, as well as probing luminosities by over two orders of magnitude deeper than currently possible, reaching the average luminosity of the (estimated) underlying population at all redshifts.

The second top-level science requirement is to identify and study the electromagnetic counterparts of GW and cosmic neutrino astrophysical sources through an unprecedented exploration of the time-domain Universe in near IR, X-rays and soft γ-rays. As a quantitative metric of the achievement of this objective, THESEUS shall be able to detect at least 30 short GRBs over the in-orbit nominal mission time, in order to build a statistically interesting sample of gravitational wave sources and short GRB sources, useful for effectively testing theoretical predictions on the nature of these objects (Stratta et al., 2018). Moreover, it will help address several questions about jets structure, their origin

and the physics of their progenitors (Binary Compact Objects). Arcsecond precision localization can be achieved from follow-up observational campaigns on the ground within the XGIS localization area. Sky coordinates at the arcsecond precision are mandatory to activate deep monitoring of the electromagnetic counterpart using large facilities such as VLT, ELT, etc. JWST will fully characterize, for example, the expected kilonova emission (too faint to be detected with IRT in most cases, i.e., at $z \gtrsim 0.05$) through high-quality spectra and deep imaging, shedding light on the role of these sources to the cosmic chemical enrichment of r-process elements. A sample of about 30 GRBs will enable the accurate ($\lesssim 1\%$) independent measure of the Hubble constant, H_0 by combining the luminosity distance obtained from the GW signal of BNS and the redshift from the electromagnetic counterpart, assuming the combination of ET+Cosmic Explorer and THESEUS.

In addition to the two pillar top-level science requirements illustrated above, THESEUS is also required to detect and characterize at least 300 transient and/or variable high-energy sources over the in-orbit mission lifetime, either on-board or in the off-line data processing, covering the whole range of astrophysical classes mentioned above. The current estimate of the rate of transients detected by the SXI largely exceeds the science requirement, even not considering the most common classes of transient events (novae, stellar flares) that one could efficiently filter on-board to ensure that THESEUS has sufficient flexibility to follow-up less common classes such as GW counterparts, SN shock break-outs, TDEs, and magnetars.

The conceptual relation between the highest-level (Level 0) scientific requirements and the Level 1 metric describing their achievement is shown in Fig. 2.5

2.3 Payload, science performance requirements

The high-level requirements outlined in the previous section include multiple complementary aspects that must be considered globally to achieve the best trade-off within the resources of a medium-class mission. These scientific objectives are achieved through the synergetic working of the whole scientific payload. THESEUS phase A has successfully conducted these trade-offs, defining a baseline mission profile that effectively satisfies the mission scientific goals. The key performance requirements are briefly discussed, taken from Amati et al. (2021) and summarized in Fig. 2.6:

- High-energy monitors sensitivity and grasp: the core of the THESEUS survey capabilities are two high-energy monitoring instruments, SXI and XGIS, with wide FoV, high sensitivity and wide spectral coverage. The grasp of SXI, as shown in Fig. 2.7, exceeds that of any existing or planned focusing X-ray telescope by over one order of magnitude. Although the already launched Einstein Probe carries telescope with an even large grasp, this does not invalidate the innovation of

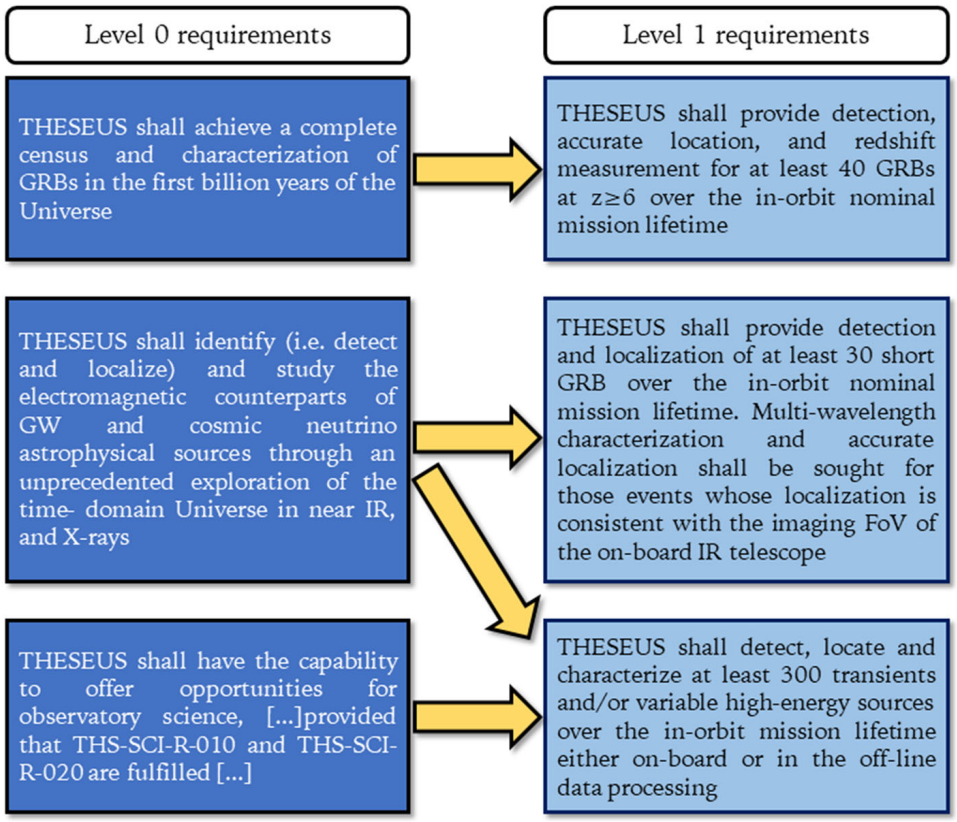

Figure 2.5: *Relation between Level 0 and Level 1 THESEUS scientific requirements (Amati et al., 2021).*

the THESEUS concept, which has a unique combination of sensitive high-energy monitors, covering a broad energy range, on a rapidly slewing platform, and a diffraction-limited IR telescope.

- Autonomous slewing capability: the crucial innovation in the science profile of THESEUS that will allow the rapid observation of the transient's error box using the IRT, identifying it with a IR source whose emission is consistent with that expected from a high-redshift ($z \gtrsim 6$) GRB afterglow, and measure its redshift. Even though other missions such as Swift and the future SVOM or EP, feature rapid autonomous slewing capabilities, THESEUS is the only mission where these capabilities are coupled to a NIR telescope.

- IRT imaging sensitivity, response time and redshift measurement accuracy: in order to fulfill the goal on the number of high-redshift long GRBs, a large IRT imaging sensitivity is required, coupled to an effective response time to a trigger ($\lesssim$10 minutes for at least 50% of the triggered events). Indeed, redshift has to

SXI sensitivity (3σ)	1.8×10^{-11} erg/cm^2/s (0.3-5 keV, 1500 s) 10^{-10} erg/cm^2/s (0.3-5 keV, 100 s)
XGIS sensitivity (1s, 3σ)	10^{-8} erg/cm^2/s (2-30 keV) 3×10^{-8} erg/cm^2/s (30-150 keV) 2.7×10^{-7} erg/cm^2/s (150 keV-1 MeV)
IRT sensitivity (imaging, SNR=5, 150 s)	20.9 (I), 20.7 (Z), 20.4 (Y), 20.7 (J), 20.8 (H)
SXI field-of-view	0.5 sr - 31x61 degrees^2
XGIS field-of-view (area corresponding to >20% efficiency)	2 sr (2-150 keV) – 117x77 degrees^2 4 sr (≥150 keV)
IRT field-of-view	15'x15'
Redshift accuracy (6≤z≤10)	≤10%
IRT resolving power	≥400
XGIS background stability	≤10% (over 10 minutes)
Field-of-Regard	≥50% of the sky
SXI positional accuracy (0.3-5 keV, 99% c.l.)	≤2 arcminutes
XGIS positional accuracy (2-150 keV, 90% c.l.)	≤7 arcminutes (50% of the triggered sGRB) ≤15 arcminutes (90% of the triggered sGRB)
IRT positional accuracy (5σ detections)	≤5 arcsecond (real-time) ≤1 arcsecond (post-processing)

Figure 2.6: *Key science performance requirements of THESEUS. They shall be granted up to mission End-of-Life (EoL). The sensitivity requirements assume a power-law spectrum with a photon index of 1.8 and an absorbing column density of* 5×10^{20} cm^{-2} *(Amati et al., 2021).*

be determined early enough, while the afterglow flux is above the IRT sensitivity flux threshold (H-band magnitude of 20.8 for a 150 s exposure). By being able to follow-up all localized GRBs/X-ray afterglows, THESEUS will detect with the IRT a large fraction of bright afterglows following the triggers on a short timescale. A redshift accuracy of 10% obtained from NIR spectroscopy measurements will ensure a clear determination of the photometric redshift. IRT spectroscopy, with a resolving power of 400, enables precise redshift measurements even at a continuum S/N of ∼3 per pixel. For bursts at $z > 6$, modeling the Lyα break profile (Fig. 2.8) provides insights into absorption by the neutral intergalactic and interstellar medium. Common metal absorption doublets, such as FeII (2374 Å, 2383 Å; 2586 Å, 2600 Å) and SiIV (1393 Å, 1402 Å), are well resolved at $R = 400$ and remain detectable in low-metallicity GRB environments with a spectral S/N of ∼10 per pixel. Consequently, THESEUS can determine onboard redshifts in the $z = 2.1 - 6$ range. Below $z = 2.1$, the CaII (3934 Å, 3969 Å) lines become too

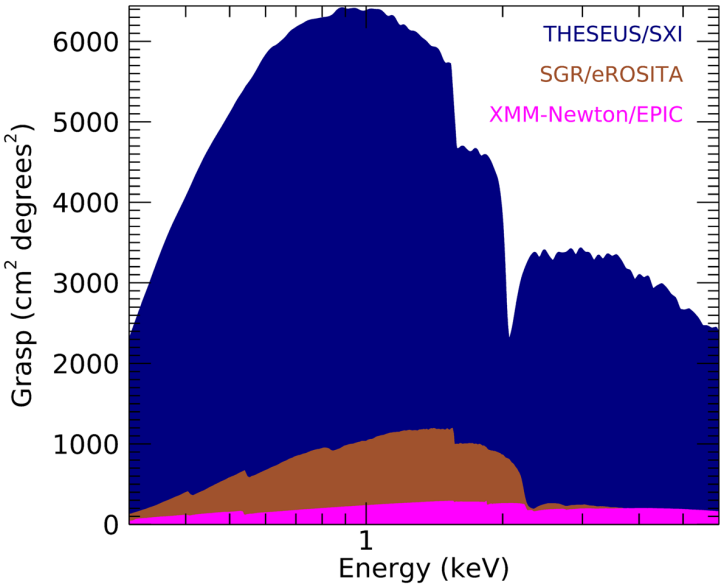

Figure 2.7: *THESEUS/SXI grasp (blue area) as a function of energy compared to that of major X-ray focusing telescopes like the X-ray survey mission SRG/eROSITA (brown) and XMM-Newton/EPIC (magenta). The SXI grasp exceeds that of any existing or planned focusing X-ray telescope by over one order of magnitude (Amati et al., 2021).*

weak, making redshift measurements, with these lines, impossible within the IRT spectral range (0.8–1.6 μm).

- Background stability: in the keV to MeV energy range, the stability of the background over a time scale of about 10 minutes is essential to allow a very sensitive triggering capability. In addition, a background as stable as possible is crucial for optimizing the characterization of the transient, in particular the measurement of key physical parameters like fluence, duration, beginning and end of the phenomenon.

- Positional accuracy: the need of having a reasonable probability to locate a trigger within the IRT field-of-view sets the requirements on the positional accuracy. In the case of SXI, a 2 arcminute positional uncertainty is needed to be confidently placed within the IRT FoV, whereas for XGIS requirement applies to short GRBs only and 15 arcminutes localization accuracy is sufficient for reducing substantially the error region provided by GW detectors even in the 30 s and allowing identification of host galaxy with ground-based telescopes.

In order to optimize THESEUS capabilities, each instrument Data Handling Unit (DHU) will operate in synergy.

The following subsections are dedicated to a detailed description of the payload.

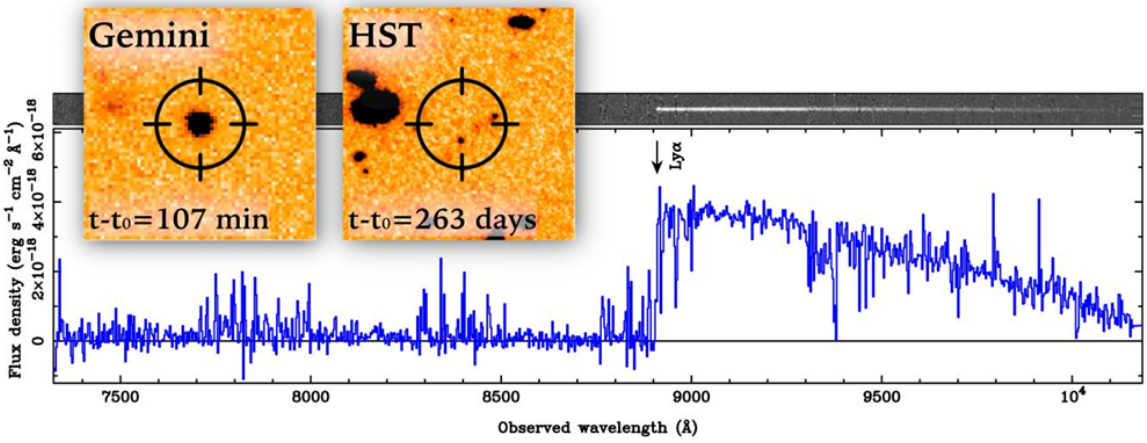

Figure 2.8: *The bright afterglow of GRB140515A at $z = 6.3$ imaged by Gemini (left inset) contrasts with the much deeper HST image of the same region (right), which provides marginal evidence for a host galaxy. The Gran Telescopio Canarias (GTC) afterglow spectrum (main panel) shows a sharp break at Ly-alpha, and detailed analysis of the spectrum places limits on the metallicity of $Z < 0.1 Z_{\odot}$ (Amati et al., 2021).*

2.3.1 Soft X-ray Imager

The Soft X-ray Imager (SXI) instrument is one of the two wide-field monitors on THESEUS and is being developed by a consortium of scientists from ESA member states, led by the UK, including Belgium, Spain, Switzerland and the Czech Republic (O'Brien et al., 2021). The SXI instrument comprises two identical wide-field modules (Fig. 2.9) aligned in order to overlap by 1° and be co-aligned with the IRT FoV. They are two "Lobster eye" X-ray telescopes, using the X-ray imaging principle, first described by Angel (1979), focusing X-ray imaging system with an effective area maintained across the entire FOV and a localization accuracy of the order of arcminute. This configuration increases the sensitivity to fast transients by several orders of magnitude. The optics aperture for the SXI modules is formed by an array of 8×8 square micro pore optics (MPOs) mounted on a spherical frame with a radius of curvature of 600 mm. X-rays which reflect off the square pore sides form a central focus, for even number of reflections, or a line focus, for odd number, resulting in a four cross-arm PSF shown in Fig. 2.10b. A brief overview of the main characteristics of SXI is reported in Tab. 2.1. In this configuration, some 75% of the incident X-rays are focused, with detailed simulations showing the optics provide the required $<2'$ transient location accuracy. Thanks to its advanced capabilities, the SXI will enable the detection of hundreds of X-ray transients per year, it will have high sensitivity to GRBs at high redshifts, search for X-ray transients linked to multi-messenger events, and monitor the X-ray sky across a wide range of timescales. Additionally, it will provide valuable targets for future observational instruments.

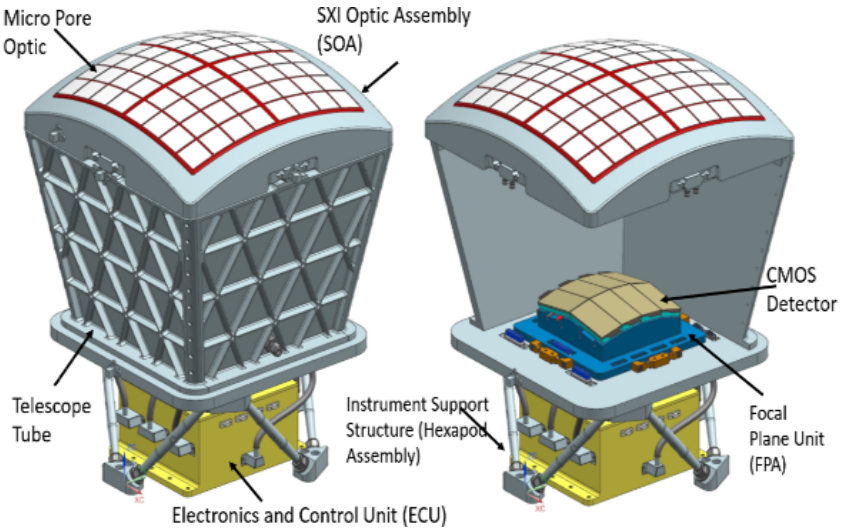

Figure 2.9: *The left panel shows the SXI module exterior view, while the right panel shows the focal plane assembly, comprising 8 CMOS detectors, located below the optics assembly. The electronics box is below the focal plane within the structure which mounts to the spacecraft. The SXI module is enclosed in MLI, multi-layer insulation, in order to maintain thermal control (O'Brien et al., 2021).*

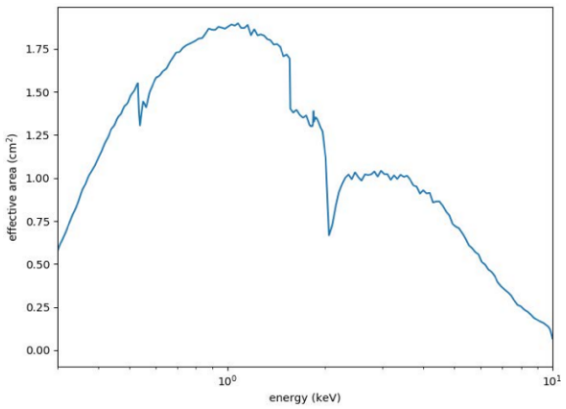

(a) *SXI half total effective area peaks at 1 keV, where the optics exhibit a FWHM of ∼6 arcmin. Using the effective area combined with an estimate of the particle and sky background rates, the minimum detectable flux level and the localization accuracy achieved as a function of time can be determined (O'Brien et al., 2021).*

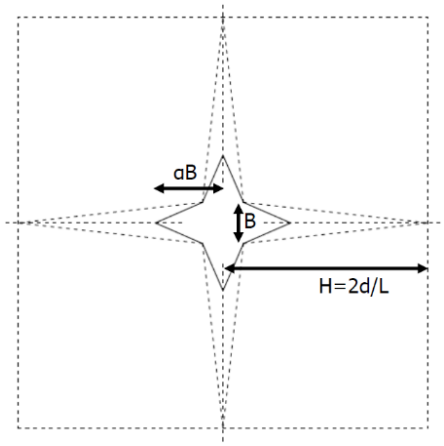

(b) *A schematic of the Lobster-eye cross-beam shape representing the PSF. The parameters B and a depend on the quality of the optics, and can be optimized with exposure time. H is the distance to the first minimum in the arms. If the parameters are set such that the source flux is limited to 50% of the total, B is a robust measure of the half energy width of the PSF (O'Brien et al., 2021).*

Table 2.1: *Main structural and functional characteristics of SXI.*

SXI	
Energy band (keV)	0.3–5
MPO size (mm^2)	40×40
Focal lenght (mm)	300
Module optics configuration	8×8 MPOs
Module FoV (sr)	∼0.25
SXI FoV (sr)	∼0.5
SXI mass (kg)	82
Transient localization accuracy	$<2'$

2.3.2 X/Gamma-ray Imaging Spectrometer

The XGIS system consists of two coded-mask X-/γ-ray cameras operating in the 2 keV–10 MeV energy range with spectrometric and timing capabilities. It operates also as an imager in the range 2 keV–150 keV beyond which the mask becomes transparent to radiation (Labanti et al., 2020). The XGIS FoV, which overlaps the SXI one, is defined as the solid angle through which a detector is sensitive to electromagnetic radiation. It can be fully or partially coded (Fig. 2.11), depending on whether the direction of radiation is comprised in the FoV of detector+collimator or if it is below it, resulting in incident radiation hitting the side of the collimator and being partially detected by the instrument detection plane.

Table 2.2: *Main structural and functional characteristics of XGIS.*

XGIS		
Energy band (keV)	2–150 keV	150–1000 keV
FoV	117°×77°	∼6 sr
Effective area (cm^2)	∼500	∼1000
Angular resolution	$<120'$	-
Transient localization accuracy	$\leq 15'$	-
Energy resolution	≤1200 eV FWHM at 6 keV	≤ 6% FWHM at 600 keV
XGIS mass (kg)	190	

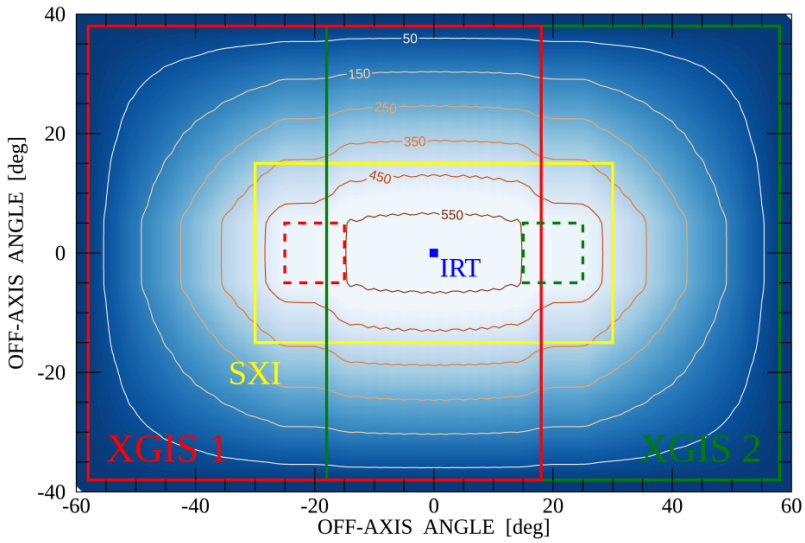

Figure 2.11: *Fields of view of the THESEUS instruments. The red (left) and green (right) squares indicate the partially coded FoV (77×77 deg^2, solid lines) and fully coded FoV (11×11 deg^2, dashed lines) of the two XGIS units. The yellow rectangle is the SXI FoV (61×31 deg^2). The blue square indicates the pointing direction of the IRT. The contour lines indicate the effective area at 10 keV provided by the sum of the two XGIS units, assuming a 50% open fraction for the coded masks (Mereghetti et al., 2021).*

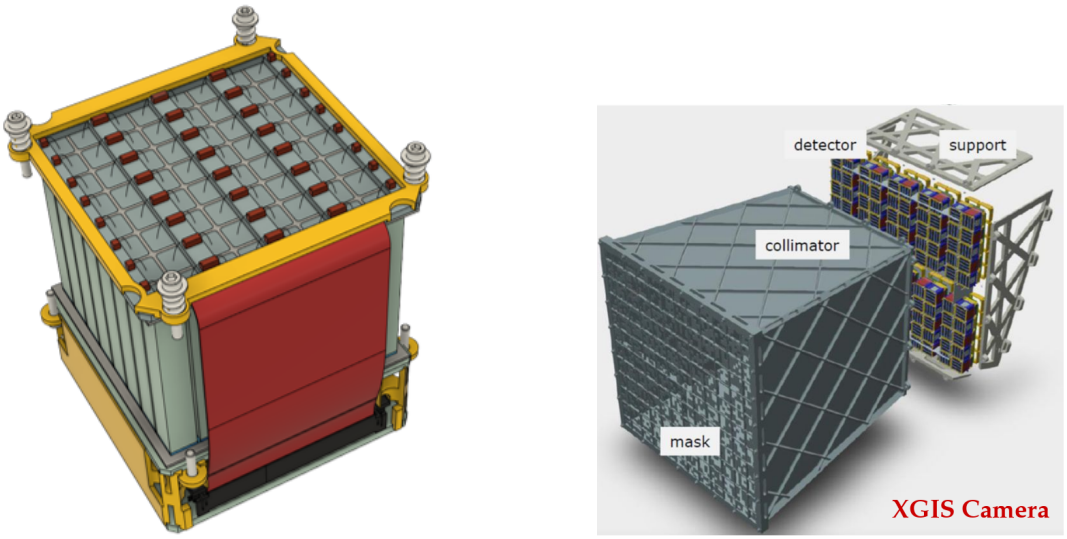

Figure 2.12: *Constitutive elements of XGIS instrument. Left Panel: XGIS module: square SDDs on top and scintillator visible from the side. Right Panel: XGIS camera, with labelled components (Labanti et al., 2020).*

The detector plane contains 10×10 modules arranged side by side. A module contains 8×8 Silicon Drift Detectors coupled to CsI(Tl) crystal scintillator bars, 3 cm long, shown in Fig. 2.12. The SDDs operate in an energy band of 2–30 keV, while the scintillators operate between 20 keV and 10 MeV. The imaging system of the XGIS is based on the coded-mask technique, made of tungsten, and located 63 cm above the detection plane. It has a random pattern with mask elements size of 2 times the detection pixel size (square pixels, of size 5×5 mm^2), providing an angular resolution of $\sim 1^\circ$ and a source localization accuracy $\leq 15'$. The two cameras are misaligned by $\pm 20^\circ$ with respect to SXI and IRT, thus providing a total FoV of $117^\circ \times 77^\circ$. Above 150 keV, the FoV of an XGIS camera can be considered of the order of ∼6 sr (almost half of the total sky). A summary of the main characteristics of XGIS is presented in Tab. 2.2. The large extension of the energy band (2 keV–10 MeV) allows XGIS to provide unique insights on the physics of the emission of GRBs through sensitive timing (milliseconds scale) and spectroscopy: it can be used complementary to SXI to detect and localize both short GRBs (also determining the hard spectrum of these events, which makes them mostly undetectable with SXI) and high-redshift GRBs (thanks to the large effective area). The structure and working principle of XGIS will be discussed in more detail in Chapt. 3.

2.3.3 InfraRed Telescope

The main goal of the IRT is to identify, accurately localize ($\leq 1''$) and measure the distance of the NIR counterparts (redshift determination to an accuracy $\leq 10\%$) of the high-energy sources discovered by XGIS and SXI. In addition, the IRT will be used to characterize the afterglows through spectroscopy and as a multi-purpose agile NIR observatory in space. The instrument responsibility is shared among a consortium led by Italy in collaboration with France, Switzerland and Germany (Götz et al., 2020). The IRT telescope is a 70 cm focusing three-mirror Korsch telescope with an off-axis (0.884°) field. The optical design will implement two separated Fields of View: one for photometry with a size of $15' \times 15'$ and one for spectroscopy of $2' \times 2'$. Using the photometric FoV, IRT will be able to acquire images using five different filters (I, Z, Y, J and H), while with the spectroscopic FoV it will provide moderate resolution ($R \sim 400$ at 1.1 μm) slit-less spectroscopy in the 0.8–1.6 μm range. The different observation modes will be implemented through the IRT Camera, which includes a filter wheel, carrying the different optical filters and a grism, which will allow for spectroscopy. The main characteristics of IRT are presented in Tab. 2.3 Thanks to its capabilities, the IRT will enable onboard, real-time redshift measurements of GRB afterglows, with a focus on high-redshift events. It will play a key role in detecting, localizing, and determining the distance of cosmological GRBs. Additionally, through spectroscopy, the IRT will characterize afterglows, providing essential data for facilities exploring deep-universe science in the 2030s.

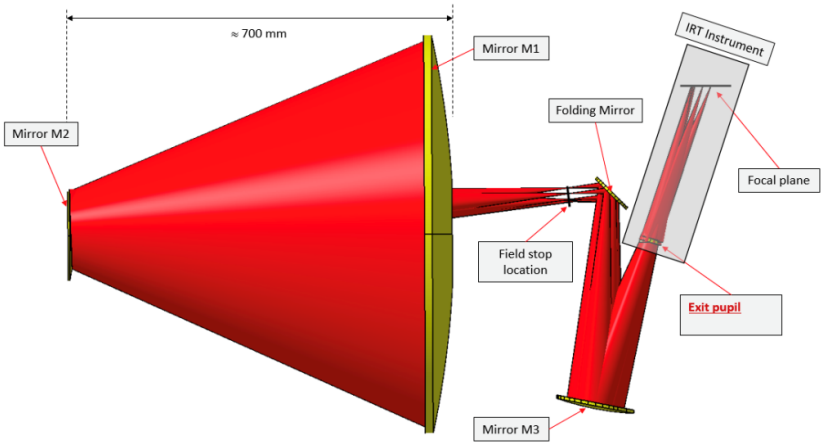

Figure 2.13: *IRT Optical scheme. M1, M2, M3 are under Italy responsibility. The exit pupil represents the optical interface with the IRT Camera provided by the consortium (Götz et al., 2020).*

Table 2.3: *Main structural and functional characteristics of IRT.*

IRT	
Photometric wavelength range (μm)	0.7–1.8
Photometric FoV	$15' \times 15'$
Photometric z accuracy	<10%
Collecting area (m^2)	>0.34
Spectroscopic wavelength range (μm)	0.8–1.6
Spectroscopic FoV	$2' \times 2'$
Resolving power	∼400
Focal length (mm)	6188
Pixel scale	$0.6''$
IRT mass (kg)	220

2.4 Observational strategy

THESEUS is designed to detect high-energy transients and rapidly transmit the most important information to the ground, such as trigger time, position, and redshift, together with full resolution data within a few hours.

Most of the mission lifetime will be spent in the so-called *"Survey Mode"*, where the two wide-field X-ray monitors (XGIS and SXI) observe the accessible portions of the sky searching for X-ray transients. Once an on-board trigger occurs due to the on-set of an impulsive X- and/or gamma-ray event, the spacecraft will switch to the *"Burst Mode"* and an automatic slew is initiated in order to place the transient, localized by either XGIS or SXI (or both), within the field of view of IRT. Then, during the *"Follow-up Mode"*, IRT will first acquire a sequence of images in different filters (lasting about 12 minutes) aimed at identifying the counterpart of the source, narrowing down its localization to arcsec accuracy, and providing a first indication of a possible high-redshift event ($z \gtrsim 6$). The spacecraft will then enter either the *"Characterization Mode"*, during which the IRT will acquire a sequence of deeper images in different filters and spectra or the *"Deep Imaging Mode"* during which only images in different filters will be acquired (depending mainly on the IR brightness of the identified counterpart). These two latter sequences aim at determining on-board the redshift of the transient source. If the counterpart identified by the IRT is a known transient or a variable source not associated with a GRB, the spacecraft will go back to the Survey Mode. The Survey Mode is anyway restored after the Characterization or Deep Imaging Mode is completed. During the Follow-up, Characterization, and Deep Imaging modes, the monitors will continue collecting data. THESEUS is also designed to operate in *"External Trigger Mode"* to rapidly respond to triggers provided by other facilities. Coordinates of an interesting source are provided from the ground to the on-board computer, and at least 4 hours after the trigger, the spacecraft is re-pointed. Depending on the specific nature of the event a custom version of the IRT characterization mode is initiated. Fig. 2.14 shows a summary of the THESEUS observational strategy.

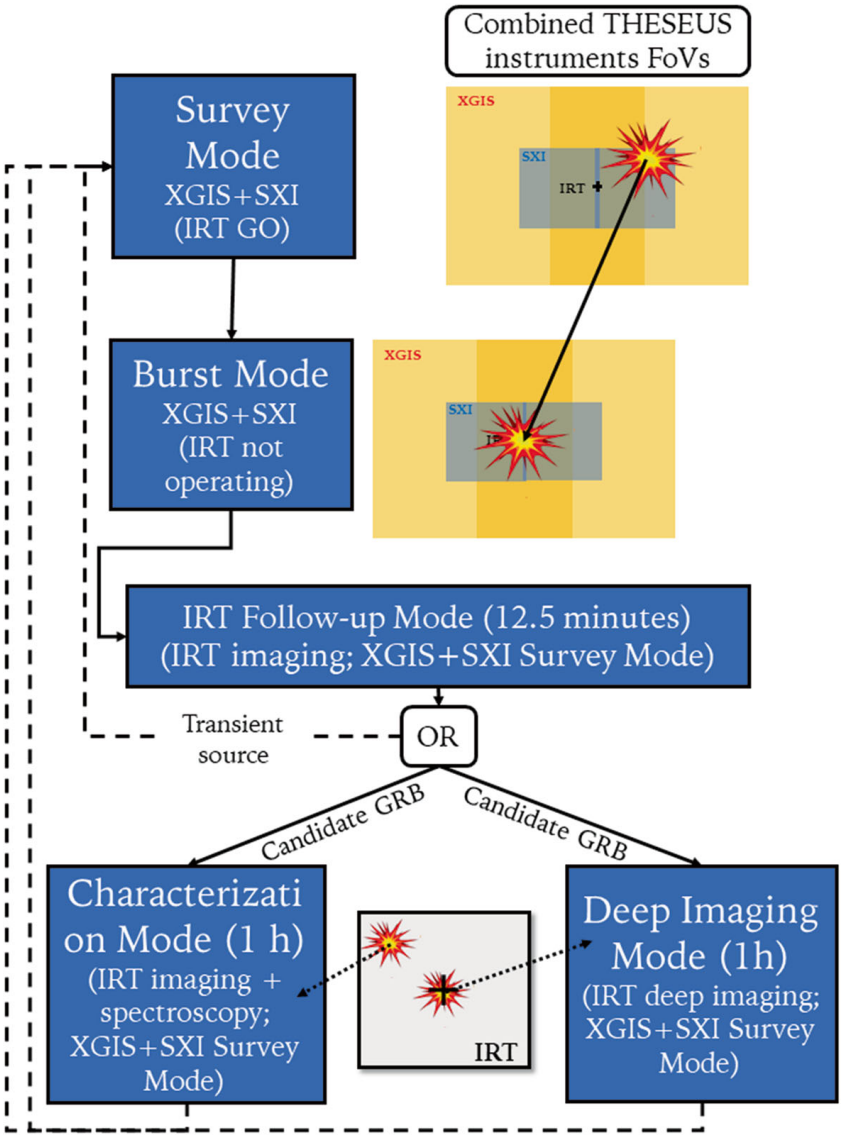

Figure 2.14: *THESEUS observational modes and strategy during the detection, follow-up and characterization of an internal trigger (i.e. an event detected by either the XGIS or the SXI, or both). Note that only a specific portion of the IRT FoV can be used for IR spectroscopy, therefore a further small slew is required (Amati et al., 2021).*

Chapter 3

XGIS: design, simulations and performance

In this chapter, the performance of XGIS, the THESEUS instrument on which this thesis focuses, is evaluated. A detailed explanation of its operating principles and construction design is provided, along with an in-depth discussion of the coded mask technique employed by the instrument for imaging.

The instrument performance is evaluated in terms of effective area and response matrix, employing Monte Carlo simulations that were conducted by me using the Geant4 software, which simulates the passage of particles through matter. This tool is a standard resource used by, among others, space agencies to assess the performance of space-based X-ray and gamma-ray instrumentation.

After describing in detail the "siswich" detection principle employed by XGIS, the methods by which Geant4 records events are presented, along with the different instrument mass models used in the simulations, starting from the simplest one and analyzing the various updates that I have introduced, until reaching a model more faithful to the current design.

Thus, for each mass model, the corresponding effective area and response matrix will be presented, which I have further generated as standard FITS format files, (ARF, Ancillary Response File, and RMF, Redistribution Matrix File).

The simulations have been carried out leveraging the computing power and storage capacity of the INAF/OAS computing cluster. These required an effective use of parallel computing capabilities (multiprocessing), as well as technical tools such as Docker. Overall, the entire set of simulations required approximately one week of computation time and around 70 GB of memory storage.

The study of the effective area and the evaluation of the instrument response, which in this work I have conducted for a single XGIS camera, are crucial in determining the performance of any instrument and, therefore, for validating the scientific requirements of the mission.

3.1 XGIS design and scientific requirements

The main objective of the XGIS instrument is to detect and identify transient sources, characterizing them across an unprecedented wide energy band, thus offering unique insights into their emission physics and underlying mechanisms (see Sect. 2.3). The advanced technology employed in the fabrication of its detection elements will yield a position-sensitive detection plane with a large effective area spanning a broad energy pass-band from soft X-rays to soft γ-rays (Labanti et al., 2020).

If the THESEUS mission were to be approved, the XGIS instrument, designed for both imaging and spectroscopy, would provide the scientific community with a state-of-the-art tool capable of providing a major contribution to high-energy astrophysics.

The integration in the THESEUS payload of a broad field of view (>2 sr) hard X/soft γ-ray detection system, which includes that of the SXI, and extends the energy band from a few keV up to several MeV with an effective area of several hundred cm^2, is critical for several reasons (Amati et al., 2022):

a It enables the detection and precise localization of short GRBs, which are pivotal for multi-messenger astrophysics, as they represent the most likely and, to date, the only detected electromagnetic counterparts of gravitational wave signals (in particular from NS-NS and NS-BH mergers); moreover, their hard spectra make them undetectable by the SXI.

b It complements the SXI capabilities by providing improved detection and localization of high-z GRBs, thanks to its large effective area at <10 keV compared to previous and current GRB detectors.

c It offers unique constraints on the emission physics and geometry of GRBs and other bright X-ray transients via sensitive timing and spectral measurements over an unprecedentedly wide energy range.

d It enables the detection of absorption features in the low-energy spectra of GRBs, which can be useful for probing the circum-burst environment, shedding light on the nature of the progenitor star, and inferring the redshift.

e It allows for a comprehensive spectral and timing characterization of GRB prompt emission over four orders of magnitude in energy, significantly expanding THESEUS scientific return by enabling tests of fundamental physics (such as Lorentz Invariance Violation) and the application of GRBs as cosmological probes for measuring cosmological parameters (through spectrum–energy correlations).

The architecture of the XGIS system, as already discussed in Sect. 2.3, consists of two X/γ-ray cameras, two power supply units (XSU), a Data Handling Unit (DHU) and harness. Each XGIS camera is powered from its dedicated XSU and is directly connected

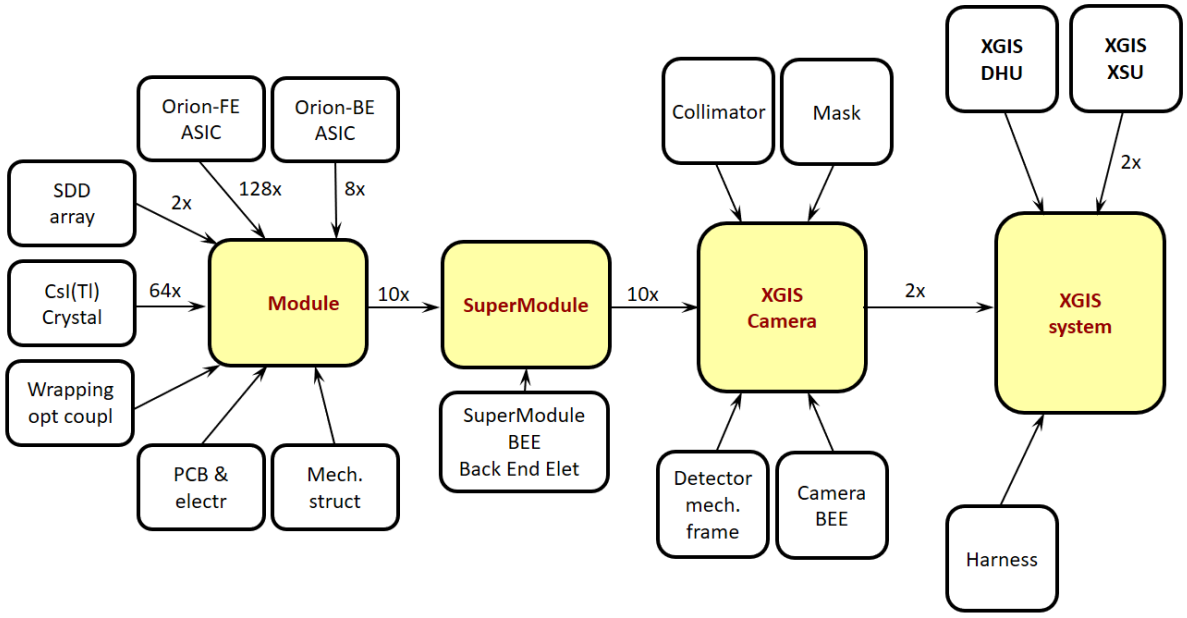

Figure 3.1: *Block diagram of the XGIS system (Labanti et al., 2020).*

to the DHU, which is the interface of XGIS with the spacecraft for commands, data downloading and power that is then delivered to the XSUs. A schematic view of the whole XGIS system is presented in Fig. 3.1.

The design of the XGIS instrument is such that it can autonomously execute the THESEUS science-driven operational modes, explained in Chapt. 2. XGIS operation modes are managed by the DHU as follows: during Survey Mode, monitoring and looking, with different methods, i.e., for GRBs within the FoV, XGIS data will be partially in photon-by-photon mode in which full information for every detected event is downloaded, and partially in time-integrated images and spectra; in Burst Mode, when a GRB is detected, XGIS switches to the photon-by-photon mode; during IRT Follow-up and Observatory Mode, and External Trigger Mode, XGIS operates as in Survey Mode.

To fulfill the scientific objectives of the THESEUS mission, XGIS must adhere to stringent requirements outlined in Chapt. 2 and summarized in Tab. 2.2. In particular, the scientific requirement that will be validated in this work states that:
"XGIS shall be able to detect photons for scientific analysis in the energy range between 2 keV and 10 MeV, assuming that the effective area at 500 keV, 1 MeV, and 10 MeV is 75%, 60%, and 40%, respectively, of the maximum value of $\sim$*1600 cm*^{2}*"* [1].

This problem is addressed using a Monte Carlo approach, which is particularly powerful for evaluating the effective area of an X-ray and γ-ray detector. Given the complexity of the interactions involved, an analytical calculation would be unfeasible. Instead, the

[1]THESEUS Report: XGIS Instrument Performance Budget.

Monte Carlo method allows for a statistical sampling of the full probability distribution of the relevant physical quantities, providing an accurate and efficient way to estimate the effective area and response.

In the next Section, the software used to perform the simulations is briefly presented, highlighting its most important aspects.

3.1.1 Geant4

Geant4[2] (GEometry ANd Tracking) toolkit is a C++ based particle transport code for simulating the passage of particles through matter using Monte Carlo methods. It includes a complete range of functionality including tracking, geometry, physics models and hits. The physics processes offered cover a comprehensive range, including electromagnetic, hadronic and optical processes, a large set of long-lived particles, materials and elements, over a wide energy range starting, in some cases, from 250 eV and extending in others to the TeV energy range. It has been designed and constructed to expose the physics models utilized, to handle complex geometries (Fig. 3.2), and to enable its easy adaptation for optimal use in different sets of applications. The toolkit is the result of a worldwide collaboration, led by CERN, of physicists and software engineers. It has been created exploiting software engineering and object-oriented technology and implemented in the C++ programming language. It runs on Linux, Mac OS, Windows and different types of UNIX flavours, 32 or 64 bits, and on modern parallel architectures. It has been used in applications in particle physics, nuclear physics, accelerator design, space engineering and medical physics (Agostinelli et al., 2003; Allison et al., 2006, 2016). Geant4 has become the standard tool used by many space agencies (e.g., NASA, ESA) in the simulation of the background and instrument performance of all major X-ray space telescopes, such as Chandra, XMM-Newton, Suzaku, Athena, eROSITA.

Applications built on Geant4 can simulate any setup or detector and radiation source, and record chosen output of physical quantities due to source particles and secondaries interacting with the material of the setup. It provides complete functionality for all areas of the simulation of particle transport. It can be used to:

- create a model of a geometry with shapes and materials,
- locate points and navigate tracks in that model,
- apply the effects of physics interactions and generate secondary particles,
- record selected information either as tallies or create hits (that are used to generate detector response),
- visualize a setup geometry and the particle tracks passing through it,

[2] `https://geant4.web.cern.ch/`

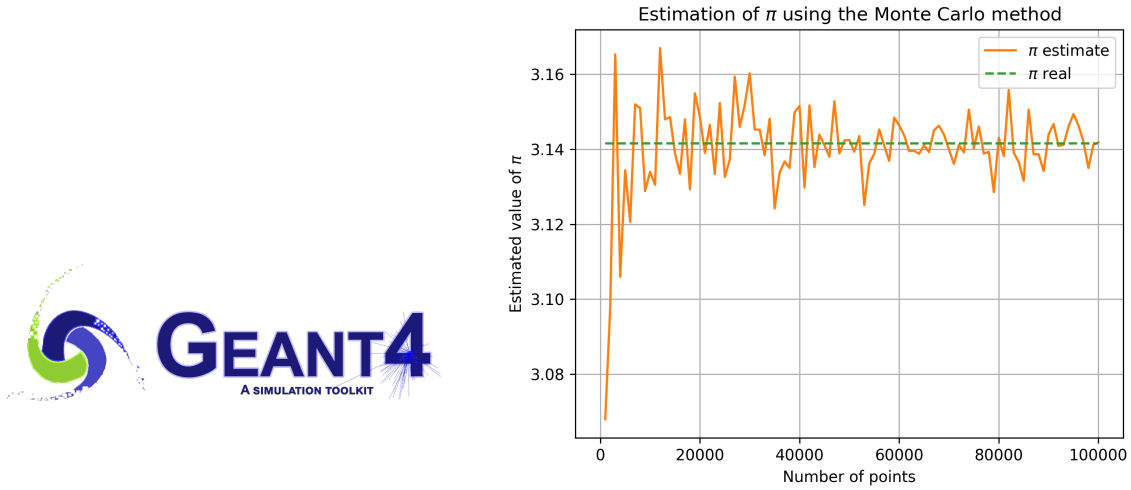

Figure 3.2: *Left: The logo of Geant4. Right: Monte Carlo method implemented for the calculation of π, obtained as four times the ratio between the number of randomly generated points inside a circle and those randomly generated inside a square.*

- interact with an application via an extensible terminal or graphical user interface.

It includes a complete set of physics processes for electromagnetic, strong and weak interactions of particles in matter over an energy range that starts from milli-eV (for thermal neutrons), eV (electrons) or typically keV (hadrons), up to hundreds of GeV (or even in part up to 100 TeV). For each type of interaction, a complete set of physics model implementations is provided. Some choices of modeling approaches are available and ready to be used as coherent configurations (named "physics lists").

Geant4 source code is available under an open source license. Any Geant4 application can and must choose whether to preconfigure, select or input beam/source parameters or details of its setup, and whether to record information using standard counts or create custom ways to collect and output quantities of interest.

The file organization of the Geant4 codes follows the structure of the *Class Categories*, smaller logical units, that are clusters of classes that are themselves cohesive, but are loosely coupled relative to other clusters. The class category diagram designed for Geant4 is shown in Fig. 3.3.

A Geant4 simulation can be launched in *Interactive Mode*, in which it is possible to visualize the detector mass model, the particle or photon source, and the tracks left by these; it can be launched in *Batch Mode*, without direct visualization, implementing commands through *macro* text files; or directly implemented hard-coded, via classes to set up the desired configuration. Nonetheless, the Geant4 toolkit provides all the components but does not provide a `main()`, that must be implemented by the user, in

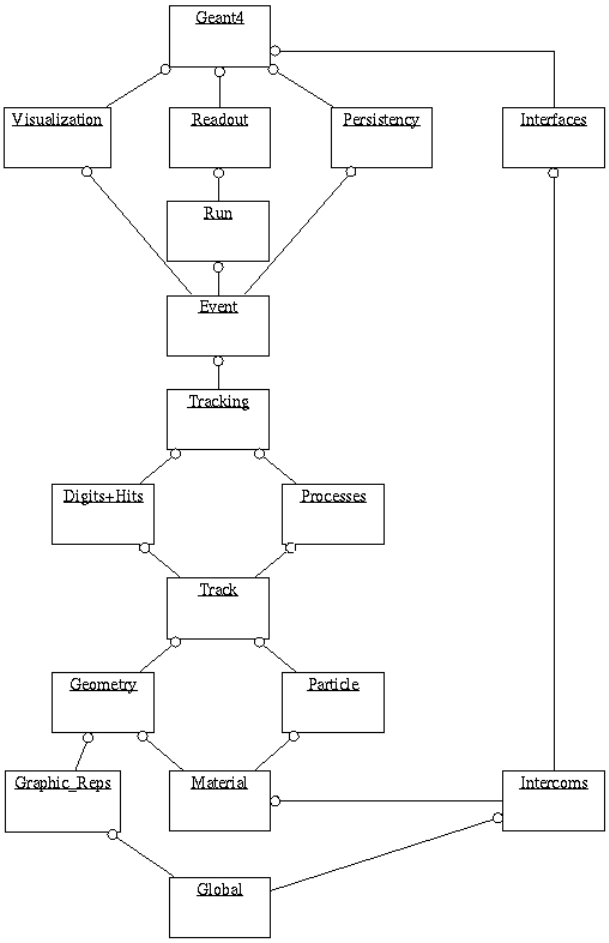

Figure 3.3: *Class categories in Geant4. 1) Run and Event: related to the generation of events, interfaces to event generators, and any secondary particles produced. 2) Tracking and Track: related to propagating a particle by analyzing the factors limiting the step and applying the relevant physics processes; this latter could perform actions long a tracking step, either localized in space, or in time. 3) Geometry and Magnetic Field: these manage the geometrical definition of a detector (solid modeling), the computation of distances to solids and also the presence of a magnetic field. 4) Particle Definition and Matter: these manage the definition of materials and particles. 5) Physics: it manages all physics processes participating in the interactions of particles in matter. 6) Hits and Digitization: related to the creation of hits and their use for the digitization phase; volumes (not necessarily the ones used by the tracking) are aggregated in sensitive detectors, while hits collections represent the logical read out of the detector. 7) Visualization: this manages the visualization of solids, trajectories and hits, and interacts with underlying graphical libraries. 8) Interfaces: it handles the production of the graphical user interface (GUI) and the interactions with external software (from Book For Application Developers).*

order to build his own application. Further details about `main()` function I provided for the application and the structure of the scripts used to launch the simulation are provided in the Appendix A.

The example presented in the following listing shows the simplest code required to build a simulation program. The `main()` method must be implemented by these classes:

- `G4RunManager` is the only manager class which should be explicitly constructed; it controls the flow of the program and manages the event loop(s) within a run. It can handle also multithreading mode.
- `G4UImanager` handles the user graphical interfaces.
- `DetectorConstruction` describes the entire detector setup, including position of volumes, geometry, materials, a definition of its sensitive regions, the readout schemes of the sensitive regions.
- `PhysicsList` defines the particles to be used in the simulation and all the physics processes to be simulated. In this work, the list `FTFP_BERT` is used, a model that simulates hadronic interactions by combining high-energy string fragmentation, and low-energy cascades, covering a wide range of interaction types between hadrons and nuclei.
- `ActionInitialization` defines the basic user action classes. These classes are also provided: `RunAction`, `EventAction`, `TrackingAction`, `SteppingAction`, which define, from the broadest to the most specific, the trajectory of the simulated particles (see Fig. 3.4).

```
#include "DetectorConstruction.hh"
#include "PhysicsList.hh"
#include "ActionInitialization01.hh"
#include "G4RunManagerFactory.hh"
#include "G4UImanager.hh"

int main()
{
    // construct the default run manager
    auto runManager = G4RunManagerFactory::CreateRunManager();
    // set mandatory initialization classes
    runManager->SetUserInitialization(new DetectorConstruction);
    runManager->SetUserInitialization(new PhysicsList);
    runManager->SetUserInitialization(new ActionInitialization);
    // initialize G4 kernel
    runManager->Initialize();
    // get the pointer to the UI manager and set verbosities
    G4UImanager* UI = G4UImanager::GetUIpointer();
    UI->ApplyCommand("/run/verbose 1");
```

```
20      UI->ApplyCommand("/event/verbose 1");
21      UI->ApplyCommand("/tracking/verbose 1");
22      // start a run
23      int numberOfEvent = 3;
24      runManager->BeamOn(numberOfEvent);
25      // job termination
26      delete runManager;
27      return 0;
28  }
```

Listing 3.1: Simplest example of main().

In Fig. 3.4, the operating principle and the main relationships between the class categories of Geant4 are shown.

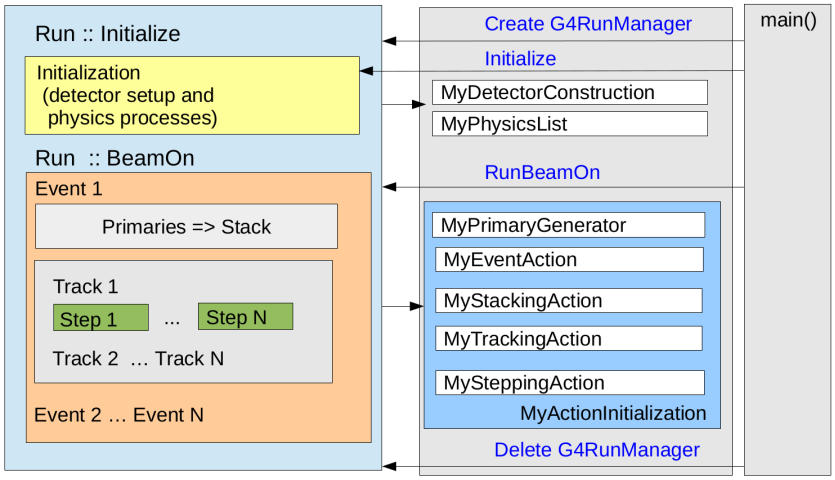

Figure 3.4: *Geant4 loops. Relation among different user classes. A simulation job starts with Geant4 kernel initialization; then one or several runs are launched; after defining the particles and the detector, a Run loops on events, defined with the command* ***/run/beamOn*** *and specifing the number of the events (e.g. 1, 100, 100000...). An Event generates primary particles and loops for their tracking and all subsequent secondary particles. A Track loops on steps, propagating a particle object, up to the point this particle "dies" or leave the detector world volume. A Step loops over the tracks to which physical processes are applied in order to simulate physics interactions; it generates secondary particles, computes energy deposit across the step. Credits: Geant4 Tutorial.*

The next listing shows an example of a macro file that is processed by the Geant4 executable: it includes the description of the primary particle source, in this case, a gamma-ray photon at 800 keV emitted from a square planar source with a side length of 140 cm. The position of the source is 200 cm away from the origin, the tilt angles, and the direction it points towards are defined. Additionally, extra physical processes

beyond the default ones provided by Geant4 are specified, such as fluorescence and Auger electron emission. Finally, the number of primary events is specified.

This type of macro has been used for the simulations to obtain the effective area and the response matrix.

```
/gps/particle gamma

/gps/pos/type Plane
/gps/pos/shape Square
/gps/pos/halfx 70 cm
/gps/pos/halfy 70 cm

/process/em/fluo true
/process/em/auger true
/process/em/pixe false

/gps/pos/centre 0.000 0.000 200.000
/gps/pos/rot1 -0.000 1.000 0.000
/gps/pos/rot2 1.000 0.000 -0.000
/gps/direction -0.000 -0.000 -1.000

/gps/energy 10.0 keV
/run/beamOn 800
```

Mass models are representations of the instruments, with varying degrees of fidelity, designed to provide an effective, albeit not necessarily perfect, model of the device. They are implemented using appropriate C++ classes: in this work, the `DetectorConstruction.cc` has been updated, and `MaskParameterisation.cc` and `PCBParameterisation.cc` have been added for the inclusion of the mask pattern and the detector structure (see next section).

The mass model used in the simulations is a simplification of the actual design of the instrument. The simulations carried out for the M5 Phase A employed a mass model featuring a simple checkerboard pattern for the coded mask with a 50% aperture. In this work, the outline of the model provided by the THESEUS collaboration during the M5 study has been initially used, to which the mask pattern[3] shown in Fig. 3.5 has been added. Subsequently, several upgrades were made to the model, which will be presented in the following Sections.

The model is composed of:

- coded mask as a tungsten (W, 19.25 g/cm^3) layer, 500 μm thick, with a random pattern and an open fraction of 50%. The mask pattern is read out from an external file;

[3]Kindly provided by Dr. Sandro Mereghetti and Dr. Edoardo Arrigoni, INAF/IASF-Milano.

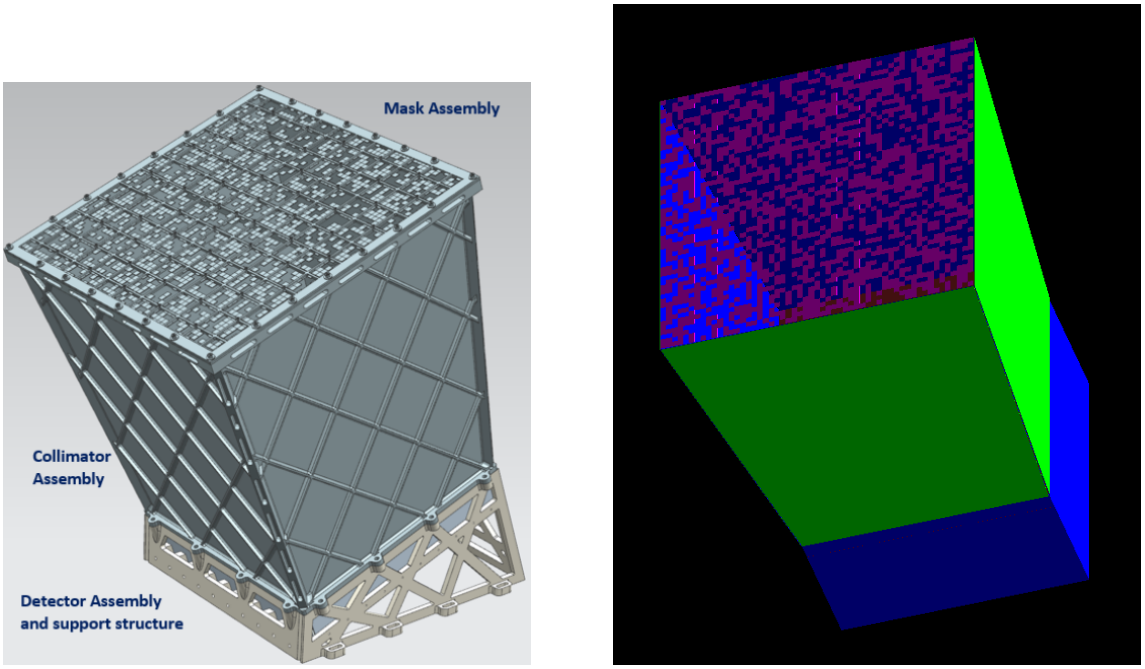

Figure 3.5: *Comparison between XGIS camera design (left) from Labanti et al. (2020) and the employed Geant4 mass model (right). In the official design, the main structures of XGIS are shown, such as the coded mask, the collimator, the detector assembly, and the support structure, which provides rigidity and stability to the detector. In the mass model, the collimator, made of tungsten, is in green, the support structure, made of aluminum, which contains the detector, is in blue, and the mask pattern is in pink.*

- detection plane with 6400 $4.5 \times 4.5 \times 30$ mm^3 CsI(Tl) scintillator bars coupled to two 450 μm thick silicon (Si) layers at both ends, the top and bottom SDDs;
- optical coupling layers, 1 mm thick, made of silicone (Dow Corning 93-500 component), between both SDDs and scintillators;
- side collimators with Al + W layers, respectively 1000 μm and 250 μm thick;
- front-end and back-end electronics (FEE/BEE) as a simplified Al box;
- simplified bus structure as an Al box with effective density.

All the model dimensions (thicknesses, relative placements, etc.) and materials are parameterized and can be read out at runtime from an external file `detectorParam.inp` and the overall model is also saved in `geometry.gdml` file.

The following section will provide a detailed view and an in-depth description of the operating principles underlying XGIS.

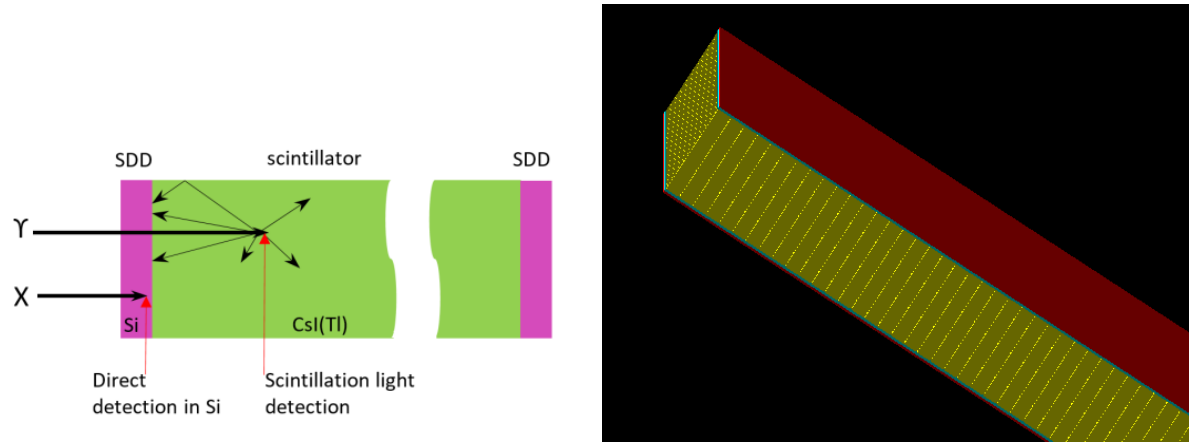

Figure 3.6: *Left: Pixel operation principle: an X-ray photon is detected directly by the upper SDD (exposed to incoming radiation, on the left in the figure), while a gamma-ray photon passes through the SDD and interacts with the scintillator. The produced scintillation light is then recorded by both the upper and lower SDD (on the left and on the right in the image; Labanti et al. (2020)). Right: Siswich mass model employed in Geant4; the SDD, in red, is modeled as a unique layer, instead of an assembly of different pixels. Scintillators, shown in yellow, form a single block array, instead of different modules. The optical coupler, reported in cyan, is in the middle.*

3.2 Siswich principle and basic detector physics

The detection of high-energy (HE) photons relies on their interaction with matter, which induces measurable changes in the detector, such as variations in current, charge, temperature, physical or chemical properties, or emitted light. These changes are then digitized through data recording and analysis. From each HE photon, four key pieces of information can be extracted: energy, which determines energy resolution; direction, which defines spatial resolution and imaging capabilities; time of arrival, which provides temporal resolution; and polarization angle, which enables polarimetric sensitivity. An ideal detector would maximize efficiency in capturing all these parameters, though no real detector achieves perfection.

As explained in Chap. 2, the fundamental detection unit of XGIS consists of two Silicon Drift Detectors and a scintillator bar (Fig. 3.6). This system is integrated with electronics designed to process the signals generated by the different components of the detection element. The signal acquisition follows the so-called "siswich" (silicon-sandwich) principle.

3.2.1 Silicon drift detectors

Solid-state detectors began to be used as the primary detection medium in devices in the early 1960s. This technology enabled significant improvements in physical size, energy resolution, and timing performance compared to gaseous detectors (Knoll, 2010; Tsoulfanidis, 2015). One of the key advantages of solid-state detectors is their compact size, made possible by their much higher density compared to gaseous detectors. High-energy charged particles can deposit their full energy within a relatively small volume of semiconductor material. Additionally, generating charge carriers (electron-hole pairs) in a semiconductor requires less energy than creating ions in a gaseous detector (Castoldi and Guazzoni, 2012). As a result, a larger number of charge carriers are produced for a given incident radiation, leading to enhanced energy resolution. Furthermore, the faster movement of electrons in semiconductors compared to gas improves time resolution.

In low-energy radiation spectroscopy, semiconductor detectors offer the best energy resolution, making them the ideal choice for detecting X-ray photons in XGIS. In fact, energy and temporal resolution depend on the amplitude of the signal received and on the associated noise, two factors that are dependent on the device. Silicon Drift Detectors (SDDs) were chosen for this application because of their excellent efficiency in detecting soft X-rays, their high quantum efficiency for light (enhanced by the thin and uniform shape), such as that emitted by a scintillator, and their ability to minimize noise during signal readout, making them more effective than other types of photodetectors.

The technology underlying the SDDs was introduced by Gatti and Rehak (1984), who proposed a novel charge transport method in which the charge transport field operates independently of the depletion field.

An SDD consists of an n-type silicon wafer with a concentric pattern of p^+ junctions covering its surface (Fig. 3.7). At the center of the innermost cathode ring lies the anode, which collects the signal. A voltage is applied across the wafer to deplete the detector, while an additional electric field facilitates charge transport. When particles pass through the detector, they generate electron-hole pairs that drift toward the electrodes under the influence of the external field (Gatti and Rehak, 1984; Castoldi and Guazzoni, 2012). This process creates a potential "gutter" within the semiconductor, guiding the electrons, generated by radiation interaction, from their point of generation to the anode (Fig. 3.8).

This design allows for a very small-sized anode that is independent of the SDD photon-sensitive surface, which collects the incident ionizing radiation. Therefore, the anode has a low capacitance, which minimizes amplifier noise and improves charge measurement accuracy.

The SDDs used in XGIS were designed and manufactured by the Istituto Nazionale di Fisica Nucleare (INFN), Sezione di Trieste, and Fondazione Bruno Kessler (FBK) as part of a collaboration with INAF/OAS and other institutions under the ReDSoX (Research Drift for Soft X-Rays) program, where research and technological innovations concerning SDDs were born and developed.

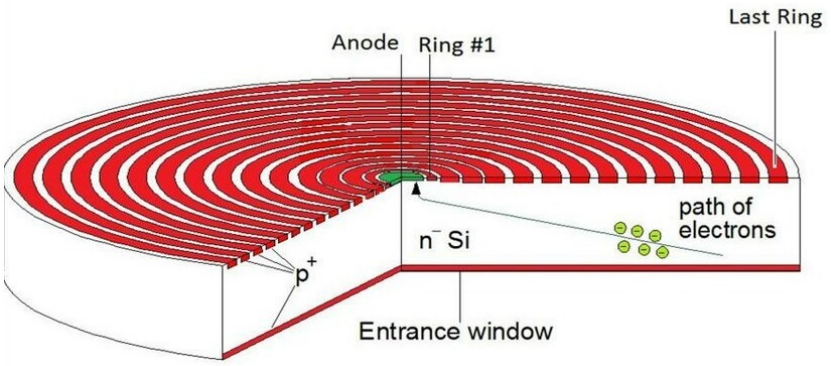

Figure 3.7: *Schematic structure of a circular-cell SDD. The concentric p+ junction strips are in red, while, in green, the central anode, toward which the electrons are drifted (Macchia, 2015).*

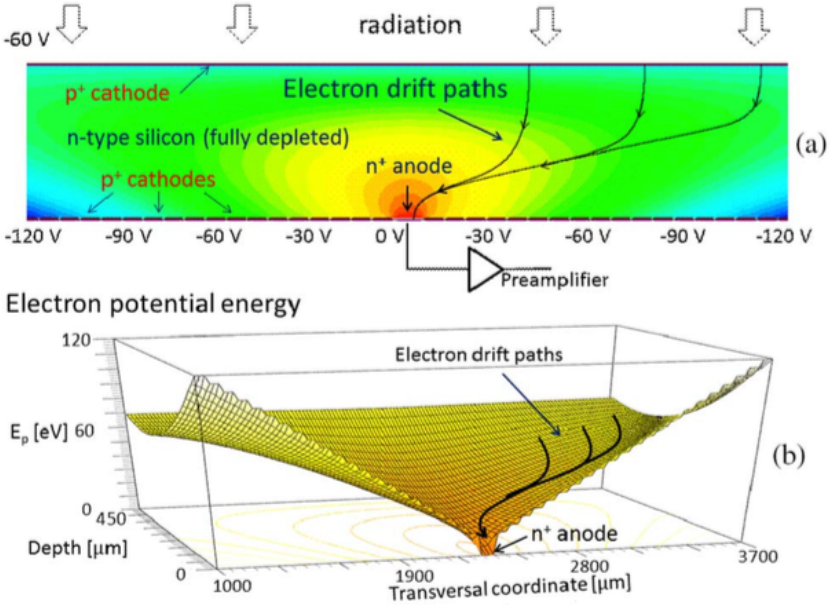

Figure 3.8: *Potential gutter within the SDD. A high negative potential is applied between the external p+ junction strip and the junction near the anode, consequently electrons move (drift) toward the anode Credits: THESEUS collaboration.*

Fig. 3.9 illustrates the 8×8 SDD cells array that will be used in XGIS. The XGIS detection plane consists of an 10×10 array of such SDD elements, for a total of 6400 independent cells. The anode side (n-side, right panel) serves as the input for incident X-ray radiation, while the window side (p-side, left panel) collects light from the scintillator. Wire bonding connects the SDD anode to the pre-amplifier, i.e., the first stage of the front-end electronics (FEE), ensuring proper signal processing.

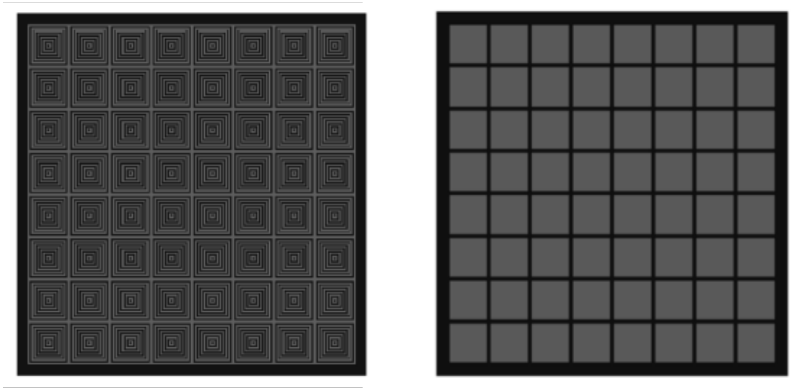

Figure 3.9: *XGIS SDD array with 8×8 individual SDDs. The n-side (entrance window), input side for X-ray radiation, with collecting anodes (left); the p-side, input side for scintillation light, optically coupled to scintillators (right) (Fuschino et al., 2020).*

3.2.2 Scintillators

Scintillation detectors, like semiconductor devices, provide a solid detection medium and are widely used for measuring nuclear radiation, particles, and photons. They convert the energy of incoming radiation into light, which then reaches a photodetector and is finally transformed into an electrical signal for further processing. The amount of light generated is proportional to the deposited energy (Knoll, 2010).

The ideal scintillator shall have:

- high efficiency in converting an energy deposit in optical photons;
- linearity, thus the energy deposit is directly proportional to the number of photons by a constant factor;
- transparency (no self-absorption of emitted light);
- fast light emission;
- good refractive index for optical coupling with photosensor:

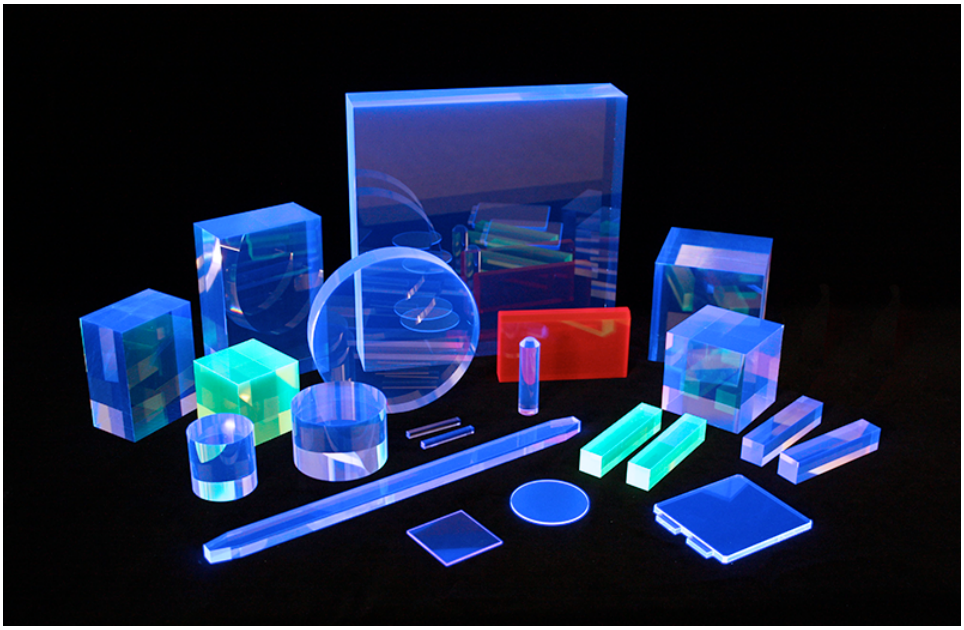

Figure 3.10: *Different types of scintillators varying in shape, material and density. Credits: Eljen Technology website.*

- high stopping power;
- no radioactive components (self-background).

No real scintillator satisfies all these criteria, and the choice for a specific application is always a trade-off depending on the focus of the experiment (e.g. fast response, high energy resolution). Selecting the appropriate scintillator is crucial also because its efficiency depends on the type of radiation it is designed to detect (Fig. 3.10). In the case of XGIS, a γ-ray detector is needed to complement the soft X-ray range. It must be composed of high-density elements, such as CsI(Tl), (Thallium-doped Cesium Iodide, 4.5×10^3 kg/m^3) to effectively absorb as much of the incident photon energy as possible. The detection of γ-ray photons is possible because they interact with the scintillator material, transferring all or part of their energy to electrons within the absorbing medium (Iyudin et al., 2022). Moreover, since the energy resolution is directly influenced by the amplitude of the detected signal, it is heavily dependent on the *Light Output (LO)*, which is measured as the number of scintillation photons emitted per keV of energy deposited in the material.

The detection of γ-rays in scintillators occurs through the three primary interaction mechanisms of high-energy photons with atoms, nuclei and electrons (Longair, 2011):

- *Photoelectric absorption*: the incident γ-ray transfers its entire energy to an electron bound within an atom of the scintillator material. Photoelectric absorption

can occur when the energy of the incident photon is larger than the binding energy of the shell electron. The electron is ejected from its atomic shell and acquires a kinetic energy $E_{\text{kin}} = E_\gamma - E_B$ where E_γ is the energy of the incident photon and E_B the electron binding energy. This process is most dominant for low-energy γ-rays (up to hundreds of keV);

- *Pair production*: when γ-rays exceed 1.02 MeV, twice the rest mass energy of an electron ($2m_e c^2$), they can disappear upon interaction with the scintillator, producing an electron-positron pair that carries the excess energy, shared among their kinetic energy $E_{e^+} + E_{e^-} = E_\gamma$. Because the positron will subsequently annihilate after slowing down in the scintillator, two annihilation photons are normally produced as secondary products of the interaction. This process becomes dominant for high-energy γ-rays (above 5–10 MeV).

- *Compton scattering*: The γ-ray transfers only part of its energy to an electron in the scintillator and is deflected through an angle θ with respect to its original trajectory. As the photon energy is higher than the electron binding energy, the latter can be ignored and the electrons can be considered essentially free. By applying energy and momentum conservation, the relation between E_γ, the gamma energy before, and $E_{\gamma'}$, the energy after, the collision can be derived.

$$\frac{1}{E_{\gamma'}} - \frac{1}{E_\gamma} = \frac{1 - \cos\theta}{m_e c^2} \tag{3.1}$$

  Because all scattering angles are possible, the energy transferred to the electron can vary from zero to a large fraction of the gamma-ray energy. The maximum kinetic energy that a Compton scattered electron can acquire, results from a "head-on" collision, which occurs when the gamma-ray photon is scattered backwards ($\theta = 180°$) (minimum kinetic energy for $\theta = 0°$). The Compton edge represents this maximum kinetic energy transferred to the electron. This interaction is the most probable in the intermediate energy range between the two previous processes, as can be seen in Fig. 3.11.

For low-energy γ-rays (where pair production is not significant), the resulting spectrum consists only of the combined effects of Compton scattering and photoelectric absorption (Fig. 3.12a). The continuum of energies associated with Compton-scattered electrons is known as the *Compton continuum*, while the narrow peak corresponding to photoelectrons is referred to as the *photopeak*.

At intermediate energies, multiple Compton scattering events may occur, sometimes followed by the escape of the final scattered photon (Fig. 3.12d). These events can partially fill the gap between the Compton edge and the photopeak and can distort the expected continuum shape for single scattering (Fig. 3.12b).

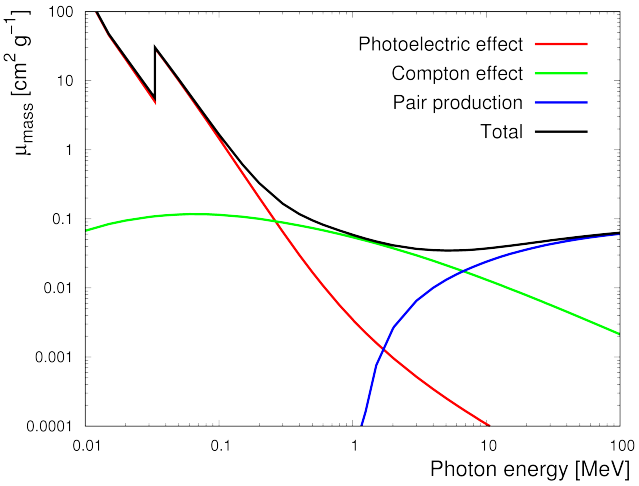

Figure 3.11: *Graph of the mass attenuation coefficient as function of the photon energy. Photoelectric effect, Compton scattering and pair production are the dominant interaction mechanisms respectively at low (E_γ <0.1 MeV), medium (0.1< E_γ <10 MeV) and high (E_γ >10 MeV) gamma energies. Attenuation properties of absorbing materials are expressed in terms of the mass attenuation coefficient μ/ρ (cm^2/g), corresponding to the ratio between the linear attenuation coefficient (μ) and the material density (Credits: Laboratory for Nuclear Technologies).*

For higher γ-ray energies, where pair production becomes significant, a more complex spectral structure emerges (Fig. 3.12c). The resulting annihilation photons may either escape or undergo further interactions within the detector, leading to partial or complete energy absorption of one or both photons. If both annihilation photons escape, only the kinetic energy of the electron and positron is deposited, producing a *double escape peak*. If one annihilation photon escapes while the other is fully absorbed, a single escape peak appears in the spectrum at an energy of 0.511 MeV below the photopeak. A broad continuum, lying between the double escape peak and the photopeak, also forms due to various intermediate scenarios where one or both annihilation photons undergo Compton scattering before escaping. These spectral features result from the different physical interactions occurring between γ-ray photons and the scintillator material, as illustrated in Fig. 3.12d (Knoll, 2010).

To ensure optimal performance, a scintillator-based detector must be designed to maximize light collection by the photodetector, in this case, the SDDs. Various techniques, such as polishing, surface treatment, or roughening, can be applied to the scintillator to enhance light transmission. Typically, the scintillator is surrounded by a light reflective or diffusive material on all sides except the one coupled to the photodetector. In the optical coupler, between SDDs and scintillators, the light transfer is maximized

using a transparent medium (epoxy or silicone), which adapts to the refraction indices of the different media.

For space applications, additional factors must be considered when selecting materials, including thermal expansion properties, lifetime (resistance to aging or yellowing), outgassing behavior in a vacuum, hygroscopic characteristics, weight, and cost (Iyudin et al., 2022).

The scintillator bars used in XGIS are made of CsI(Tl) with a square cross-section of 4.5×4.5 mm^2 and a length of 3 cm. The surfaces in contact with the SDDs are polished, while the remaining sides are left rough. Each bar is individually wrapped with reflective paper, except for the surfaces coupled to the SDDs. This design ensures that scintillation light is effectively directed into the photodetector through an optical coupling made of a transparent and flexible silicone pad, which is less than 1 mm thick.

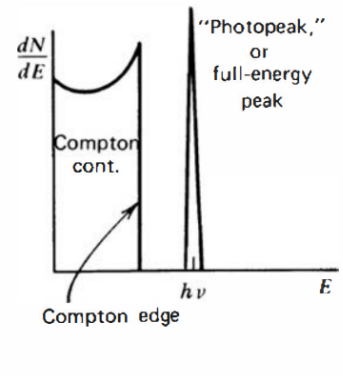

(a) The processes of photoelectric absorption and single Compton scattering give rise to the low-energy spectrum.

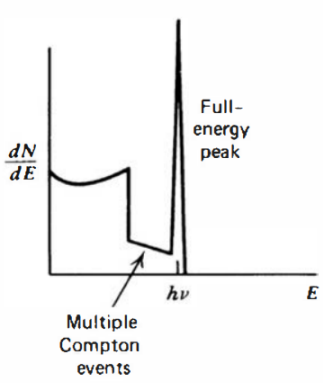

(b) In addition to the continuum from single Compton scattering and the full-energy peak, the spectrum at medium energies shows the influence of multiple Compton events.

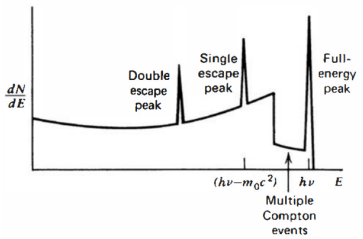

(c) The single escape peak corresponds to initial pair production interactions in which only one annihilation photon leaves the detector without further interaction. A double escape peak will also be present due to those pair production events in which both annihilation photons escape.

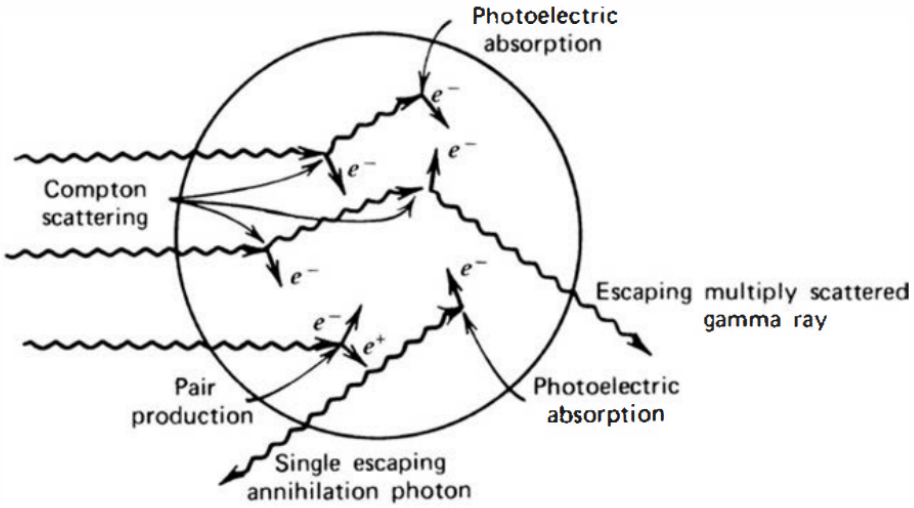

(d) Representation of the possible interactions between γ-ray photons and scintillator material.

Figure 3.12: *Representation of spectra for low, medium and high γ-energy photons in Fig. 3.12a, 3.12b and 3.12c, with respective physical interactions in Fig. 3.12d (Knoll, 2010).*

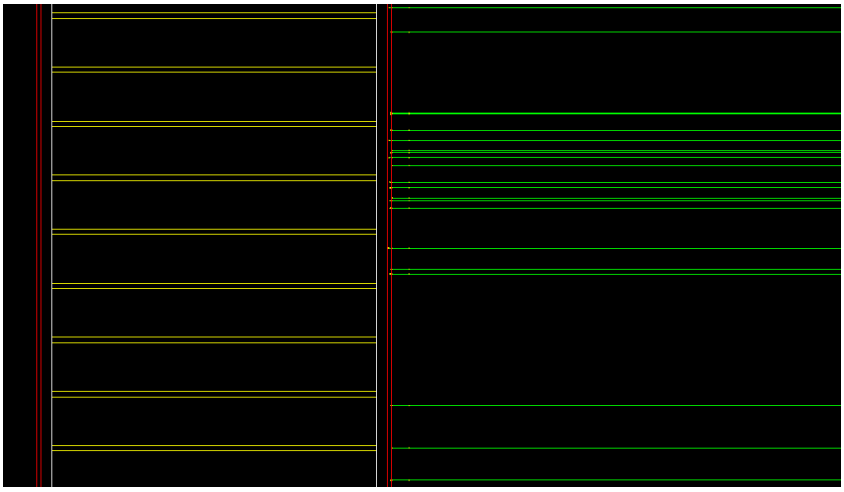

Figure 3.13: *Geant4 interactive mode simulation. The SDDs, in red, and the scintillators, in yellow, are viewed from the side. Photons with an energy of 10 keV, shown in green and coming from the right, are provided as input for the simulation. In these range of energies, the photons are completely absorbed in the SDD and classified as "X-mode events".*

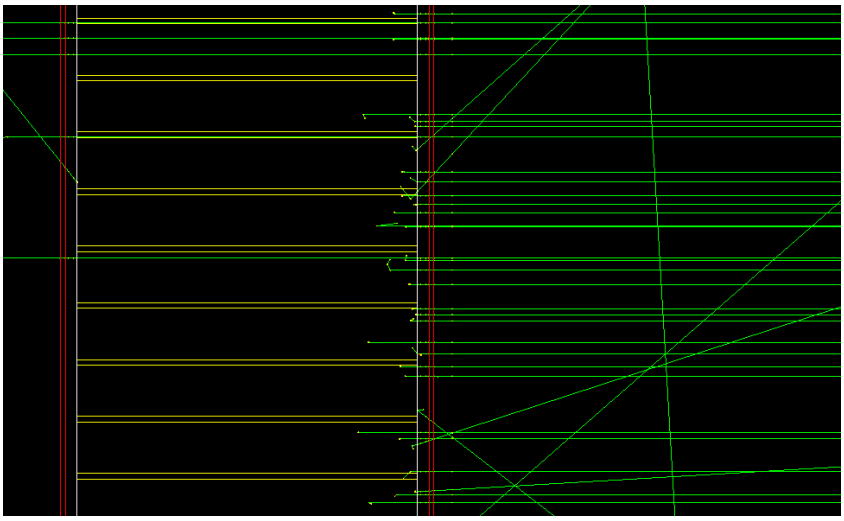

Figure 3.14: *Simulation performed using 120 keV photons, coming from the right. At these energies, the photon energy is deposited in the scintillators (yellow cells) through photoelectric absorption and classified as "S events". Parallel green lines are primary photons while oblique ones correspond to photons scattered by the collimator. In red the two SDDs.*

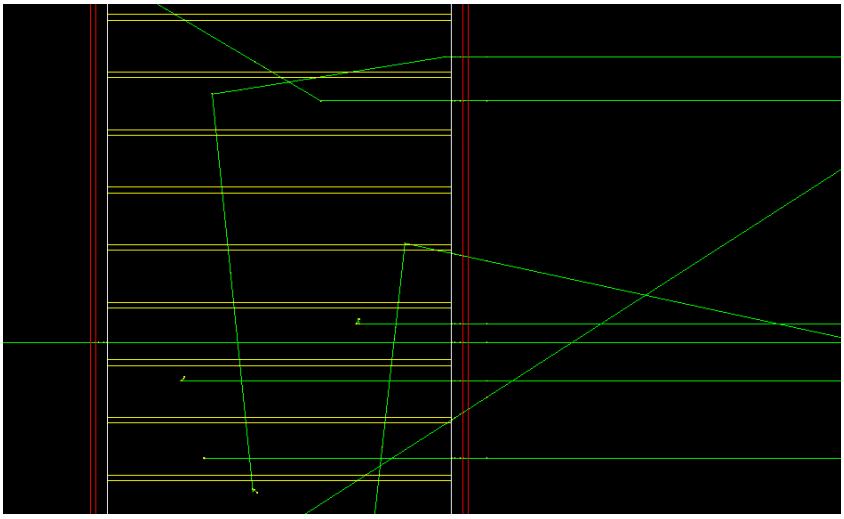

Figure 3.15: *Simulation performed using 500 keV photons. Different (Compton) scattering angles can be seen as broken green lines. X events now are rare since the SDD is no more capable to directly absorb them, while S-mode are dominant. The simulation is not yet able to record the height at which the interaction occurs within the scintillator bar (3 cm long). This feature will be implemented in future upgrades.*

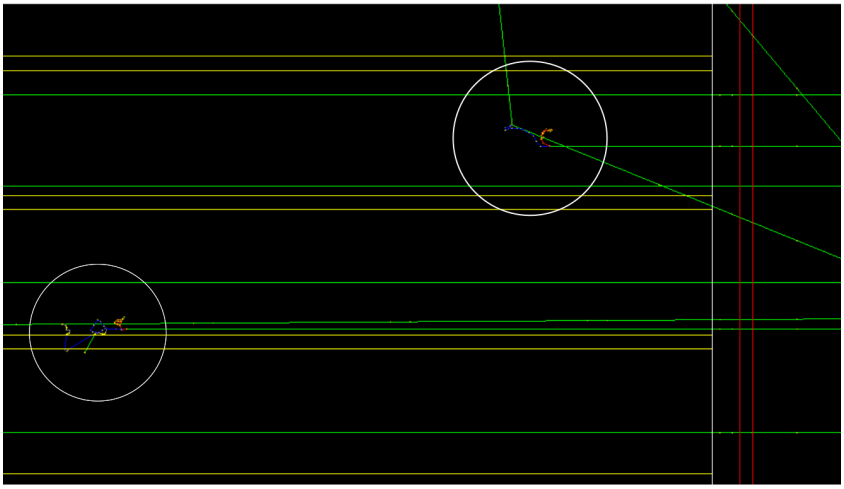

Figure 3.16: *Simulation performed using 5000 keV photons. Detection occurs thanks to pair production within the scintillators, visible two times here: a single photons (green line) suddenly disappears leaving an electron (red line) and a positron (blue line).*

3.2.3 Siswich principle

A γ-ray detector utilizing a CsI(Tl) scintillating crystal coupled with a silicon photodetector also functions as a direct X-ray detector, as radiation interacting within silicon

enables the simultaneous detection of both X-rays and γ-rays using a single, compact device. Given that the energy threshold and spectroscopic performance of such a detector are primarily influenced by the electronic noise of the photodetector, an SDD was chosen due to its significantly lower intrinsic electronic noise. This type of detector compact design makes it a practical solution for meeting the strict weight and volume limitations of space missions (Marisaldi et al., 2005).

The fundamental concept behind the siswich principle (an acronym that translates to "Silicon Sandwich", Fig. 3.17) involves coupling two SDDs, one positioned above and the other below a CsI(Tl) scintillator bar, forming a single detection unit known as a pixel. Each pixel simultaneously operates through direct conversion for detecting low-energy X-rays (2–30 keV) and indirect conversion for higher-energy X-ray and γ-ray photons (20 keV–10 MeV). Incident low-energy photons entering from the top window are absorbed and detected by the upper SDD; photons with energies exceeding $\sim$20 keV pass through the top SDD and reach the scintillator crystal, where the emitted scintillation light propagates toward both SDDs: the total energy deposited in the scintillator is determined by summing the signals measured by the top and bottom SDDs.

It is essential to account for the differing energy requirements for charge generation in silicon and CsI(Tl), which are 3.66 eV/e^- and 70 eV/e^- (collected by one SDD), respectively. Therefore, distinguishing the interaction location is crucial for accurately determining the deposited energy (Mele et al., 2021).

Future implementations of the code will include the possibility of determining the height at which the interaction occurs within the scintillating bar, allowing for an efficient distinction between counts from the source and those from background sources (see next chapter).

Signals generated in silicon and CsI(Tl) differ not only in amplitude but also in timing characteristics. The creation of electron-hole pairs from X-ray interactions in silicon leads to a rapid signal response ($\sim$10 ns rise time), whereas scintillation light collection is governed by the de-excitation time of fluorescence states, necessitating a shaping time of a few microseconds to prevent significant "ballistic deficit" (Marisaldi et al., 2005).

Figures 3.13, 3.14, 3.15, 3.16 show a side view of the detector, hit by photon beams with energies of 10 keV, 120 keV, 500 keV, and 5000 keV, respectively. Each figure illustrates the most probable high-energy photon interaction mechanisms with matter for the given energy range. The simulation identifies an X-mode event (X-ray) and an S-mode event (γ-ray), depending on whether the photon is absorbed by the SDD or the scintillator.

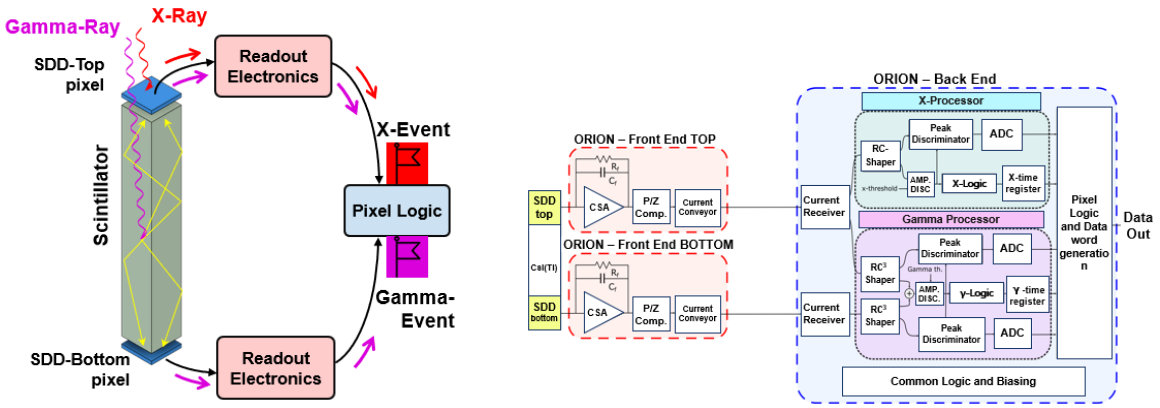

Figure 3.17: *Left: schematic view of an XGIS pixel, composed of two SDDs, a CsI(Tl) crystal bar and two front-end readout chips (ORION-FE) and one back-end multichannel processor (ORION-BE). The event is processed by the Readout Electronics, ORION-FE, and a single multichannel processor for the event identification, ORION-BE. Right: Block-diagram of a single ORION readout electronics for the readout of a single XGIS pixel, composed by two ORION-FE (top and bottom) and one ORION-BE with separate X and γ processing channels (Srivastava et al., 2024).*

3.2.4 Data workflow

The implemented Monte Carlo simulator does not register scintillation light photons as shown in the previous figures, but it effectively separates the events into *X-mode* and *S-mode*, meaning the X and γ photons. Specifically, energy deposits inside the SDD are classified as X-mode events, while those in the scintillators are classified as S-mode events. Simulating the production of the optical scintillation photons within Geant4 would introduce excessive complexity, not only in the computational burden given by the tracking of an extremely large number of optical photon, but also in the accuracy of the description of the optical interfaces between each volume in the mass model.

Fig. 3.18 shows the workflow of the simulations performed in this work.

The output of the simulation is a file `scorefile.root`, which is directly converted into a FITS[4] file format and contains all the information recorded in the simulation, as shown in Fig. 3.19. The output FITS file contains the following information related to the simulation:

- the `EventID`, which identifies the primary event generated, ranges from 0 to the number of primary events initially generated. In the table, only the ones that were actually recorded are reported.

[4]Flexible Image Transport System, the standard data format used in astronomy, endorsed by NASA and the International Astronomical Union.

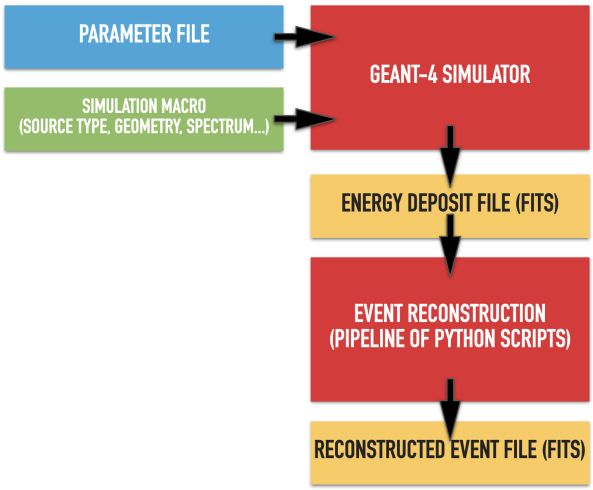

Figure 3.18: *Workflow of the simulations performed in this work.*

TOPCAT(1): Table Browser

Window Rows Help

Table Browser for 1: scorefile_1256.0_0.0_0.0.fits

	EventID	En_dep	Scint_ID	Pixel_ID	X_Pixel	Y_Pixel	Z_Pixel	X_Primary	Y_Primary	Z_Primary	Theta_Pri...	Phi_Primary	En_Primary	Event_time
1	1	1255,49972	2892	-1000	0,	-6,	0,	0,21842	-6,13632	200,	0,	0,	1256,	6,
2	8	0,12388	1090	-1000	-11,	-16,	0,	-10,8947	-16,13843	200,	0,	0,	1256,	6,
3	8	239,10413	1093	-1000	-9,5	-16,	0,	-10,8947	-16,13843	200,	0,	0,	1256,	6,
4	8	720,59995	1004	-1000	-9,5	-16,5	0,	-10,8947	-16,13843	200,	0,	0,	1256,	6,
5	106	0,09534	7300	-1000	-21,	19,	0,	-20,89197	18,84706	200,	0,	0,	1256,	6,
6	106	0,06356	7210	-1000	-21,5	18,5	0,	-20,89197	18,84706	200,	0,	0,	1256,	6,
7	106	473,99235	7209	-1000	-22,	18,5	0,	-20,89197	18,84706	200,	0,	0,	1256,	6,
8	106	437,69685	7211	-1000	-21,	18,5	0,	-20,89197	18,84706	200,	0,	0,	1256,	6,
9	141	210,36334	4608	-1000	12,5	3,5	0,	25,45393	-13,79244	200,	0,	0,	1256,	6,
10	149	258,78735	6484	-1000	16,	14,	0,	16,45288	15,35748	200,	0,	0,	1256,	6,
11	161	172,39776	7306	-1000	-18,	19,	0,	-19,25559	13,77671	200,	0,	0,	1256,	7,
12	171	0,19328	6816	-1000	4,	16,	0,	4,21655	16,07892	200,	0,	0,	1256,	6,
13	171	123,62232	6728	-1000	4,5	15,5	0,	4,21655	16,07892	200,	0,	0,	1256,	6,
14	177	530,49876	-1000	5112	-2,5	6,5	-1000,	-3,51908	24,44059	200,	0,	0,	1256,	6,
15	212	0,09664	2413	-1000	-17,	-8,5	0,	-17,22246	-8,3873	200,	0,	0,	1256,	6,
16	212	0,21554	2147	-1000	-16,5	-10,	0,	-17,22246	-8,3873	200,	0,	0,	1256,	6,
17	212	1254,96379	2054	-1000	-18,5	-10,5	0,	-17,22246	-8,3873	200,	0,	0,	1256,	6,
18	236	99,89115	3043	-1000	-13,5	-5,	0,	-14,50913	-2,48699	200,	0,	0,	1256,	7,
19	245	582,83782	2789	-1000	-7,	-6,5	0,	-7,56146	0,83083	200,	0,	0,	1256,	6,
20	270	232,36391	4771	-1000	5,	4,5	0,	5,38534	5,40814	200,	0,	0,	1256,	6,
21	312	1255,71277	2696	-1000	-9,	-7,	0,	-9,11151	-6,85453	200,	0,	0,	1256,	6,
22	352	1013,83891	2592	-1000	-16,5	-7,5	0,	-16,18605	-9,512	200,	0,	0,	1256,	6,
23	352	0,06356	2237	-1000	-16,	-9,5	0,	-16,18605	-9,512	200,	0,	0,	1256,	6,
24	364	10,08784	-1000	3145	-7,	-4,5	-1000,	-7,07263	-4,34595	200,	0,	0,	1256,	6,
25	451	222,15536	7483	-1000	-18,5	20,	0,	-14,9957	20,7388	200,	0,	0,	1256,	7,
26	452	156,7301	2923	-1000	15,5	-6,	0,	14,46068	-4,87965	200,	0,	0,	1256,	6,
27	461	936,55617	4463	-1000	-15,5	3,	0,	-10,0602	26,19277	200,	0,	0,	1256,	6,
28	544	0,05104	3939	-1000	-10,5	0,	0,	-10,6668	-0,02524	200,	0,	0,	1256,	6,
29	544	0,39926	3936	-1000	-12,	0,	0,	-10,6668	-0,02524	200,	0,	0,	1256,	6,
30	544	1254,99746	4025	-1000	-12,	0,5	0,	-10,6668	-0,02524	200,	0,	0,	1256,	6,
31	553	1254,91823	6084	-1000	-6,	12,	0,	-7,92502	9,69889	200,	0,	0,	1256,	6,
32	553	0,09664	5814	-1000	-7,5	10,5	0	-7,92502	9,69889	200	0	0	1256	6

Total: 138.214 Visible: 138.214 Selected: 0

Figure 3.19: *Data output example (from Topcat) of an on-axis simulation using 1256 keV photons. Several multiple interaction are reported: EventID 8, 106, 171, 212, 352, 544, 553. Multiple interactions must be filtered out to avoid excessive counting of detected photons.*

- `En_dep` is the energy deposit for each photon interaction, in keV.
- `Scint_ID` and `Pixel_ID` identify the location where the recorded interaction occurred. `Scint_ID` refers to the individual scintillator bar, while `Pixel_ID` refers to the individual SDD cell. Both numbers are integers ranging from 0 to the total number of pixels simulated. If `Scint_ID`$=-1000$, this is a flag indicating *X-mode events*. On the other hand, if `Pixel_ID`$=-1000$, this flag indicates an *S-mode event*, and the scintillator where the interaction occurred is recorded.
- `X_Pixel`, `Y_Pixel`, `Z_Pixel` refer to the physical position (in cm) of the interaction. These are measured relative to the center of the coordinate system, which is placed at the central point of the detector.
- `X_Primary`, `Y_Primary`, and `Z_Primary` are the coordinates where the primary event originated, and they are all within the geometry of the defined source. Additionally, `Theta_Primary` and `Phi_Primary` represent the zenithal and azimuthal emission angles, respectively, relative to the surface of the source.
- `En_Primary` is the energy of the primary event in keV.
- `Event_time` refers to the time at which the detection occurs measured from the start of the simulation, in nanoseconds.

This raw data FITS file is subsequently cleaned using a Python script. The data is processed by reconstructing the primary events. In fact, if a photon is recorded in different parts of the detector, it is considered as a multiple detection. It would be an error to treat each multiple detection as separate individual photons recorded. Therefore, the newly produced data file allows for event reconstruction by summing the energy deposits for events with the same ID, leaving only events with unique event IDs in the final FITS file. Examples of multiple interactions are shown in Fig. 3.20

At this point, the cleaned data file is further processed to create two additional FITS files, which contain respectively the X-mode and S-mode events. This separation is carried out by following the flagging method already explained.

Noise effect In addition to the energy deposits for X-mode and S-mode events, the contribution from the intrinsic noise of the instrument has been added, as it affects the energy deposits.

The quality of the performance of a detection system used for energy measurements is, indeed, characterized by the width of the pulse-height distribution (i.e., the amount of detectable voltage produced by a given energy deposit) obtained with particles of the same energy. Even in the case where each particle deposits exactly the same energy in the detector, the pulse-height distribution will not be a single line, as expected for

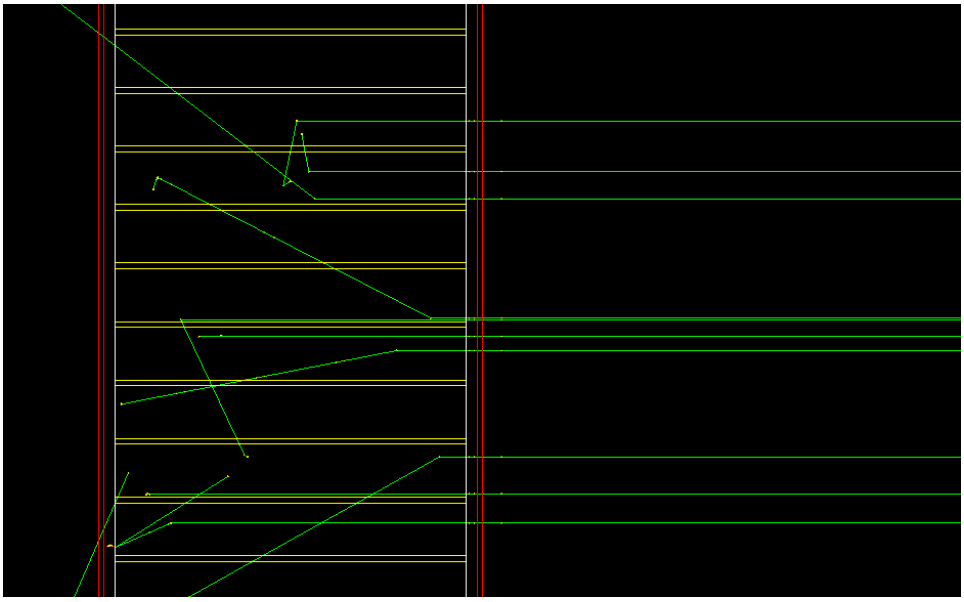

Figure 3.20: *Simulation carried out using 500 keV photons. Each Compton scattering event (broken green lines) marks a photon detection within the scintillators, where the interactions occur. The scattered photons, undergoing photoelectric absorption, disappear within another scintillator, marking an additional detection for the same primary event. The code has been updated to reconstruct the energy of the primary event and prevent the incorrect registration of multiple detections.*

a monoenergetic source (Tsoulfanidis, 2015); instead, it will have a certain finite width due to:

a statistical fluctuations in the number of charge carriers produced in the detector;

b electronic noise in the detector itself;

c incomplete collection of the charge produced in the detector.

For both X-mode and S-mode events, the effect of the noise, assumed to be a random process, is introduced by sampling from a Gaussian distribution centered at the input value of the energy deposit, E_{dep}. Different methods to compute the standard deviation have been used.

For X-mode, it has been calculated as:

$$\sigma_X = \frac{w\sigma}{1000} \quad [\text{keV}] \qquad \text{where} \quad \sigma = \sqrt{\sigma_{\text{Fano}}^2 + \sigma_{\text{el}}^2} \quad [\text{e}^- \text{rms}] \tag{3.2}$$

$w = 3.66$ eV/e$^-$ is the average energy needed to produce one e$^-$/hole pair in silicon[5];

[5]In silicon the energy gap is E_{gap}=1.1 eV. The difference between w and E_{gap} shows that part of the energy of the incident photons is dissipated into processes that do not generate charge carriers.

$\sigma_{\text{Fano}} = \sqrt{F\,E_{\text{dep}}/w}$ represents the statistical fluctuation expressed in terms of the *Fano Factor* F (0.125 for silicon[6]); $\sigma_{\text{el}} = 30$ e$^-$rms represents the electronic noise in the detector itself.

For *S-mode*, the standard deviation is:

$$\sigma_S = \frac{\sigma}{1000} \quad [\text{keV}] \qquad \text{where} \quad \sigma = \sqrt{\sigma_{\text{stat}}^2 + 2\sigma_{el}^2} \quad [\text{e}^-\text{rms}] \tag{3.3}$$

$\sigma_{\text{stat}} = L_{\text{eff}}\,E_{\text{dep}}$, the statistical fluctuation in terms of the light efficiency, $L_{\text{eff}} = 25$ e$^-$/keV, which is the amount of electrons, drifting toward the anode in the SDD, produced per energy deposited in the scintillator. This value is affected by the efficiency of the optical coupling between the scintillating bar and the SDD. The factor of 2 in the electronic noise contribution is the sum in quadrature for both SDDs (upper and lower) which detect the scintillation light.

The precaution is maintained that if a negative number is sampled, the output will be the same as the input energy deposit.

3.3 Response files

The working philosophy of a typical X-ray or γ-ray instrument is to register properties of individual photon events that hit the detector material and produce a certain amount of current/charge, registered as counted photons. Thus, the raw data is essentially a table where each column describes a different attribute of an event. These include basic properties like the time of the event, the amount of charge generated by the event (known as the Pulse Height Amplitude or PHA), and in the case of detectors with imaging capability, the raw coordinates of the event in units of detector pixels. A major portion of data processing/cleaning is to convert these event attributes into astrophysically relevant quantities (Jiang and Pasham, 2020).

The instrumental response of an X-ray experiment is usually expressed by the *effective area* and by the *redistribution matrix*. These quantities are condensed in the so-called ARM and RMF files, which are included among the results of this work:

- the Ancillary Response File (ARF) consists of a 1-D array as a function of energy stored as a table extension in a FITS file. It contains the combined telescope/filter/detector areas, the effective area (cm^2), and the quantum efficiency (QE is the probability to convert a single incident photon into an observed detector count) as a function of energy. When an input spectrum is multiplied by the ARF, the result is the distribution of counts that would be seen by a detector with perfect (i.e.

[6] F is the ratio between the actual standard deviation of the number of pairs produced and the number of pairs produced. $F = 0$ means no statistical fluctuation in the number of pairs produced; $F = 1$ the numbers of pairs produced is governed by Poisson statistics.

infinite) energy resolution. The RMF is then needed to produce the final observed spectrum. The sensitivity of the detector to photons of known energy can be also a function of the position in the field of view;

- the Redistribution Matrix File (RMF) contains information about energy redistribution. Photons of a given incident energy may have a measured pulse height that differs significantly from the nominal incident energy. It consists of two FITS extensions: the `MATRIX` extension, 2-D array, energy vs PHA channels, which provides, for each incident photon energy, a probability of being measured at each possible pulse height; and the `EBOUNDS` extension that explicitly lists the nominal energy range of each PHA channel. The RMF is created by folding together individual components due to the detector gain and the detector energy resolution.

In the next sections, the XGIS effective area will be evaluated by employing different mass models in the simulations, starting with a simple model with a more realistic mask pattern, and gradually incorporating additional layers, each briefly described, until reaching the final detector configuration.

Then, the response matrix for the simple model and the completely upgraded model will be discussed.

3.3.1 Effective area

The effective area quantifies the capability of a telescope to collect photons. In the case of XGIS, it depends on the characteristics of the camera, such as the geometry, physical dimensions, and materials of the coded mask, the collimator, and the detector, as well as the incidence angle of the incoming radiation. In general, for an X-ray experiment (which can be at the focal plane of focusing optics, or can be a collimated instrument), the effective area is expressed by the formula:

$$A_{\text{eff}}(E, \theta, x, y) = A_{\text{geom}} \times R(E) \times V(E, \theta) \times QE(E, x, y) \tag{3.4}$$

where A_{geom} is the geometric area of the detector, $R(E)$ is the fraction of photons reflected by the mirror (which depends on the radiation energy, but also on the polishing and material), $V(E, \theta)$ is the vignetting function, which expresses the dependence of the collected flux on θ, the off-axis angle, and $QE(E, x, y)$ is the quantum efficiency, the fraction of incident photons effectively registered, which depends on the photon energy and its position on the detector (x, y).

All these contributions can be also differently expressed in terms of their overall effect, as:

$$A_{\text{eff}} = A_{\text{geom}} \times \epsilon(E, \theta, \phi) \tag{3.5}$$

where the effective area A_{eff} of a telescope, from a given direction, is given by the geometric area A_{geom} exposed to the incoming flux, convoluted with the efficiency ϵ in

collecting and detecting photons from the (θ, ϕ) direction. One can further assume that every location (x, y) in the detector plane has the same sensitivity.

In this thesis work, the simulations performed to evaluate the effective area required the development of a Python script pipeline that automatically launches the Geant4 executable from the terminal. The data obtained from the simulation were then processed as described earlier, and subsequently, the ARF (and RMF, see the next section) files were generated.

The pipeline, through an initial Bash script, utilizes a three-loop structure to run simulations with different input energies and varying photon incidence angles. This script generates a macro file that is then directly passed to the Geant4 application, which is executed in *Batch Mode*. The output is a `root` file, `scorefile.root`, which is subsequently converted into FITS format.

The `for` loop runs a total of 6624 simulations in order to evaluate the effective area and the response matrix, with the following inputs:

- monochromatic energies: from 2 to 30 keV with a step of 0.5 keV, from 32 to 150 keV with a step of 2 keV, from 152 to 600 keV with a step of 4 keV, and finally from 616 to 5000 keV with a step of 32 keV;
- zenith angles θ from 0° to 120° with a step of 15°;
- azimuthal angles ϕ of 0° and 45°.

The energy, θ and ϕ space was determined through a trade-off between statistical accuracy and computation time. In future improvements, simulations could sample this space more finely, leading to a better representation of physical phenomena, higher accuracy in results, and the possibility of identifying secondary effects. However, this leads to higher computational costs.

For all simulations, a total of 1.470.000 primary events was used, generated from a square-shaped plane source with an area of 140×140 cm^2, employed to ensure full detector coverage and corresponding to a photon density of 75 photons/cm^2. A parallel beam was used to simulate a point source located at an infinite distance. Fig. 3.21 shows an example of simulation.

The effective area was evaluated using simulations for a single XGIS camera using the following formula:

$$A_{\text{eff}} = \frac{N_{\text{det}}}{\rho_{\text{source}}} \times \left(\frac{80}{89}\right)^2 \tag{3.6}$$

where N_{det} is the number of events detected (in X-mode or S-mode) while ρ_{source} depends on the number of primary events and the area of the source. The multiplicative factor is introduced to account for "dead pixels". The XGIS design, indeed, includes the division into Modules and Supermodules (see Chapt. 2), thus a passive space one-pixel wide

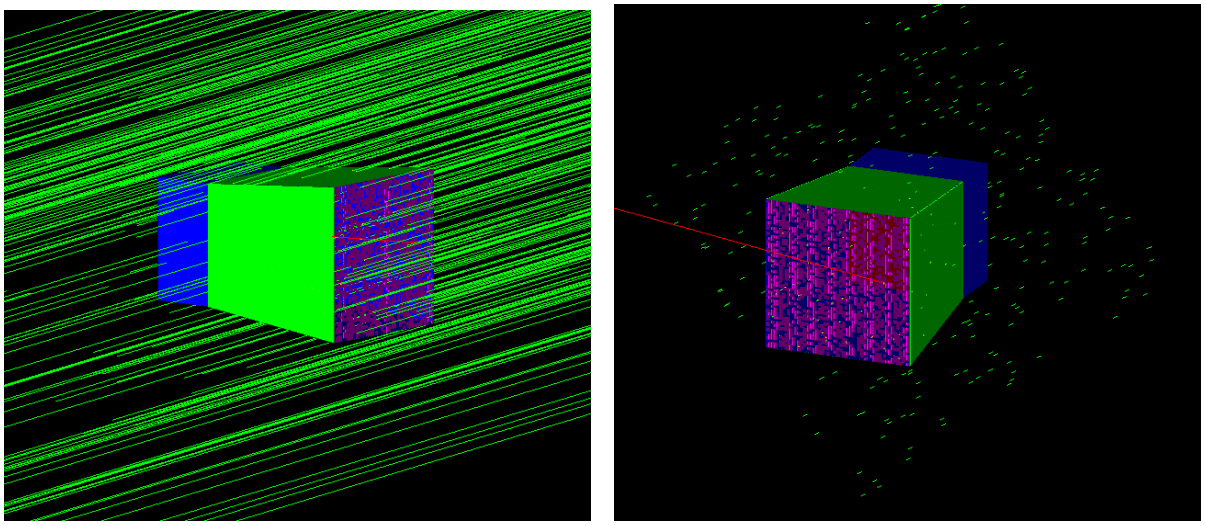

Figure 3.21: *The images show the same simulation at 10 keV with $\theta = 30°$ (zenith angle) and $\phi = 40°$ (azimuthal angle) from different viewing angles. Left: XGIS detector exposed to the parallel photon beam. Right: The square shape of the source, covering the entire detector, is visible. The red track corresponds to an electron ejected from a mask element due to the photoelectric effect; in order for the electron to be ejected, the interaction must have occurred very close to the surface, otherwise, it would have been absorbed by the other tungsten atoms within a few microns.*

separates each Module from the adjacent ones. This results in 9 "dead" rows and 9 "dead" columns in the plane. To account for this construction effect, since the mass model considers for simplicity a unique 89×89 block of scintillator bars, this correction factor has been introduced in the calculation of the effective area to match the real design.

In the following paragraphs, a description of the different elements added to the mass model used in the simulations is provided, along with the corresponding effective areas obtained.

Simple mass model

The first round of simulations has been performed using a simple mass model derived from the M5-era one provided by the THESEUS Collaboration, with the addition of a realistic coded mask pattern, as previously described. The mask pattern, readout from an external file, has been implemented using appropriate C++ classes. Below is a brief description of the functioning of the coded mask, which is further discussed in the Appendix B.

An X-/γ-ray detector becomes an X-/γ-ray telescope when it is able to measure the

direction, energy and arrival time of celestial X-rays. Since GRBs are bright only for short time intervals and arrive at unpredictable times from random directions in the sky (see Chapt. 1), to maximize the expected number and redshift distribution of the detectable GRBs, XGIS is designed to optimize several factors: the fraction of the sky that it is capable of monitoring; the localization accuracy to perform follow-up observations as soon as possible; the energy range to characterize the GRB spectral shape that extends to low energies to favor high-z sources. The optimized design must take into account the payload budget resources for a Medium class satellite mission (i.e., mass, dimension, power, telemetry; see design trade-offs from Mereghetti et al. 2020).

In order to perform imaging, XGIS utilizes the coded mask technique because, as successfully demonstrated by many past and current missions, an excellent trade-off between the aforementioned requirements can be achieved. A design consisting of two identical units ("cameras") with partially overlapping fields of view was adopted. The two cameras will be pointed in directions offset by $\pm 20^\circ$ from the satellite boresight direction, which coincides with the IRT pointing direction. Coded mask imaging requires a position-sensitive detector, previously described, able to record the shadows of the aperture pattern cast by the sources in the field of view. The recorded "shadowgrams" can then be deconvolved to reconstruct images of the sky.

The coded mask is an array of square elements, made of tungsten with a thickness of 1 mm, placed at a distance of 63 cm from the top surface of the detector. The dimensions of the mask pattern are 56.5×56.5 cm^2. The mask is supported by a mechanical Al structure, 1 mm thick, that connects it to the detector and is reinforced inside by the collimator, which consists of four slabs of a 250 μm thick layer made of tungsten. This latter is crucial to ensure that no unencoded radiation reaches the detector and also acts as a passive shield to delimit the field of view at low energies.

In coded mask imaging systems, the field of view (FoV) is defined by the dimensions of the mask (D_M), of the detector (D_D) and their distance (H). The central part of the FoV, corresponding to directions for which the whole source flux recorded by the detector has been modulated by the mask pattern, is called *Fully Coded FoV* (FCFoV). The *Partially Coded FoV* corresponds instead to directions for which only part of the detected source flux has passed through the mask pattern. The sensitivity is nearly uniform in the FCFoV, while it gradually decreases in the PCFoV, as a result of the decrease of detector area used to record the source counts (Fig. 3.22).

For a given spatial resolution of the detector, which in the XGIS case corresponds to the distance between the centers of adjacent SDD pixels (i.e., the pitch, $P = 5$ mm), the angular resolution Θ of a coded mask imaging system depends on the mask distance ($H = 63$ cm), and on the size of the mask elements ($M = 1.027$ cm), a value that will be optimized during the Phase B study. For on-axis sources it can be approximated by $\Theta \sim \sqrt{(M/H)^2 + (P/H)^2} \sim 1.04^\circ$. The final value of M has not been decided yet, since it will be optimized with a careful trade-off during the phase-B study, when further design elements will be defined. However, it can be anticipated that the ratio M/P will

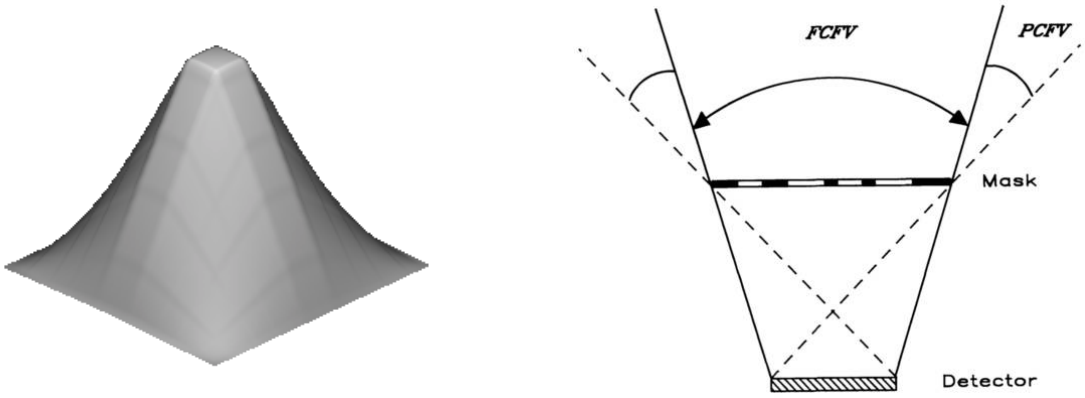

Figure 3.22: *Left: Angular dependence of the detector working area (i.e. the detector geometric surface that records a source flux modulated by the mask pattern) for one XGIS camera. The top value is achieved in the Fully Coded FoV of* $\sim 10^\circ \times 10^\circ$. *The zero response has a size of* $77^\circ \times 77^\circ$ *(Mereghetti et al., 2020). Right: Division of the field of view of a coded-mask instrument, such as XGIS. Within tha FCFoV, the radiation is totally coded, while within PCFoV, part of the incoming radiation does not reach the detector plane (Caroli et al., 1987).*

likely be in the range 1.5–2.5, leading to $\Theta \sim 0.8^\circ$–1.2°. The source location accuracy (SLA) is generally much better than the angular resolution because it depends also on the statistical significance (SNR) of the source detection. In particular, the location accuracy is given approximately by SLA $= \lambda\Theta/\mathrm{SNR}$. The factor λ, of the order of a few, depends on how the SLA and source significance are defined, as well as on the imaging properties of the mask, that in general are not those of an ideal system.

Coded mask imaging relies on the fact that part of the detection plane measures the source plus background contribution, while the remaining part measures only the background. This is true in an ideal instrument, where the mask closed elements are completely opaque and the open elements are completely transparent. In a real system, the closed mask elements become increasingly transparent as the photon energy increases, as shown for XGIS mask in Fig. 3.23, 3.24. On the other hand, the open elements are not completely open due to the need to mechanically support the mask, and therefore they are increasingly opaque as the photon energy decreases. These two effects are encoded by the transparency functions $T_C(E)$ and $T_O(E)$ of the closed and open mask elements. The detector sensitivity as a function of energy thus depends on these two functions.

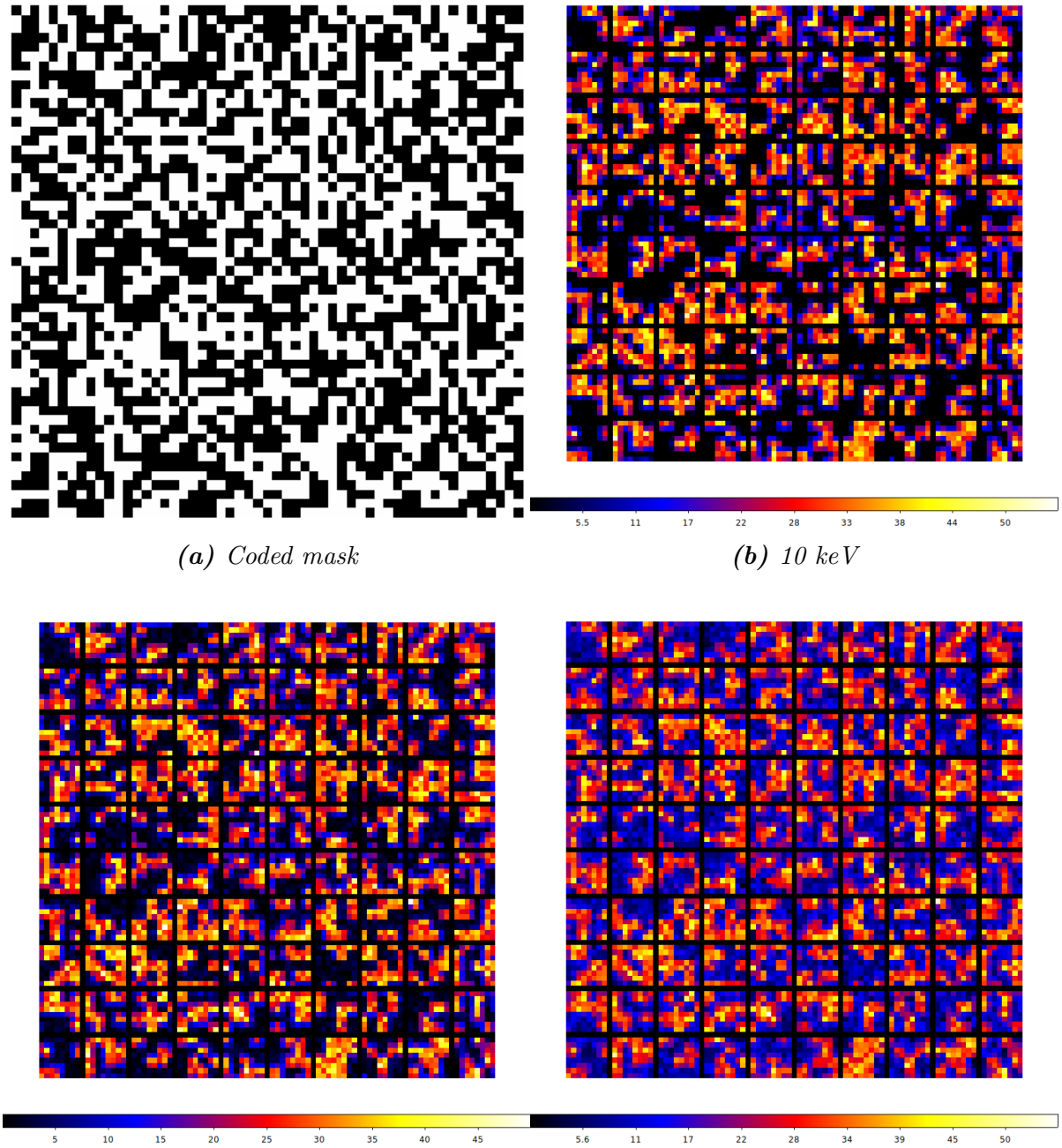

(a) *Coded mask* ***(b)*** *10 keV*

(c) *100 keV* ***(d)*** *150 keV*

Figure 3.23: *The random pattern coded mask employed; black pixels correspond to closed elements (top left panel). The images of the detector are shown in sequence, representing the number of counts per pixel for on-axis simulations using 10 keV, 100 keV, and 150 keV, respectively (for a 500 μm thickness of the mask). Within these energy ranges, the XGIS works as imager, as the mask elements are opaque to such energy range. At 150 keV, pixels that did not register counts at lower energies begin to light up.*

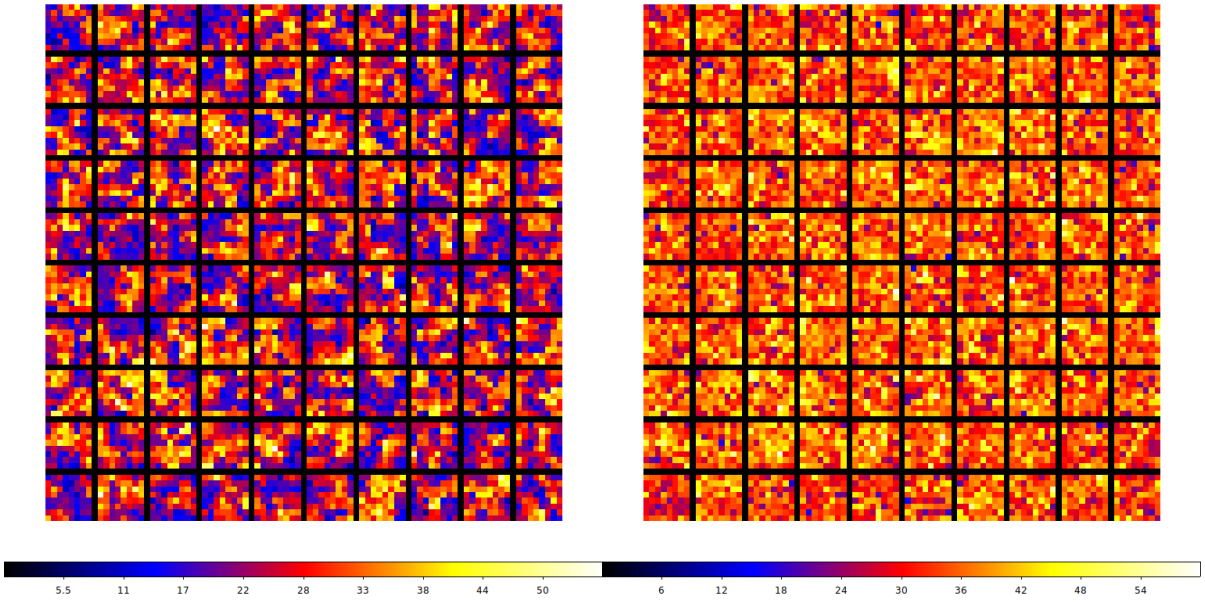

(a) *200 keV* ***(b)*** *500 keV*

Figure 3.24: *Images of the detector at for input energies of 200 keV and 500 keV, above the energy range of XGIS imaging capability (for a 500 µm thickness of the mask). The pixel counts result more uniform because, at high energies, the closed mask elements become transparent. Therefore, the effective area increases, as it is limited only by the passive elements of the spacecraft and no longer by the mask-collimator system. The images, like the one in Fig. 3.23, has been produced taking into account the 9×9 rows of dead pixels that reproduce the XGIS design*

Another factor that affects the sensitivity is the mask open fraction, that is defined as the number of open mask elements divided by the total number of mask elements. The optimal mask fraction that maximizes the sensitivity (usually in the 25% to 50% range) depends on the nature of the background.

The coded mask pattern has been implemented in the mass model using an external FITS file. It has an open fraction of 50% (Fig. 3.23a). The mask tiles have a side length of 1.027 cm, avoiding a size exactly twice the pixel one to allow for finer sampling of the shadowgram. In fact, if the dimensions were a multiple of the pixel size, the deconvolution process for image reconstruction could introduce artifacts. Additionally, it is not guaranteed that there are no sky directions that project the same shadow or very similar shadows (identical shadows, generated by different sources, turn out into identical deconvolved images). The sensitivity is also influenced by the relative size of the mask and detector elements. Since these also affect the angular resolution (and source location accuracy), it is necessary to make a trade-off between these properties

and the sensitivity. Finally, one must take into account that the imaging properties, and in particular the so-called "coding noise", depending on the chosen mask pattern have an influence on the sensitivity. This is because, in general, the instrumental response to a point source is not a delta function but consists of a central peak with structured sidelobes (see Appendix B).

Fig. 3.36, 3.37 and 3.38 show examples of the shadowgrams of the mask projected onto the detector and the corresponding deconvolved images[7]. The source is a GRB with a typical Band function spectrum with slope $\alpha = -1$, $\beta = -3$, and $E_{\rm break} = 300$ keV, simulated firstly on-axis, then at $\theta = 30°$ and $\phi = 30°$, and finally, they are overlapped.

In Fig. 3.25, the effective area for the simple mass model is shown for different off-axis angles, considering both azimuthal angles $\phi = 0°$ and $\phi = 45°$.

The on-axis effective area at low energies (black line) is $\sim$800 cm^2 reflects how, in this energy range, the main limitation is due to the presence of the coded mask, which blocks about half of the incoming radiation detected in *X-mode*, up to 10 keV. Starting from 20–30 keV, events detected in *S-mode* become dominant.

Notably, from 150 keV onward, the energy threshold for imaging in XGIS, the effective area increases significantly because the FoV is no longer constrained by the tungsten collimator and coded mask, which become nearly transparent, and is instead determined only by other passive elements of the satellite. At very high energies, the detector response becomes mostly isotropic ($\sim$6 sr), dominated by the simple cosine effect.

A distinct feature can also be observed at $\sim$67 keV, corresponding to the increase in the mask opacity due to the K-shell edge of tungsten.

Above 400 keV, the effective area starts decreasing due to the declining efficiency in photon detection (low cross section interactions). As the zenith angle θ increases, the effective area decreases across the entire energy range.

A sharp drop in the effective area is observed at angles of $\sim 30°$, as at these angles, a source is within the partially coded region of the FOV. Consequently, the illuminated portion of the detector is smaller because it is partially covered by the collimator. At 45°, instead, a source is entirely outside the XGIS FOV, resulting in a null effective area.

[7]Kindly provided by Edoardo Arrigoni, INAF-IASF Milano.

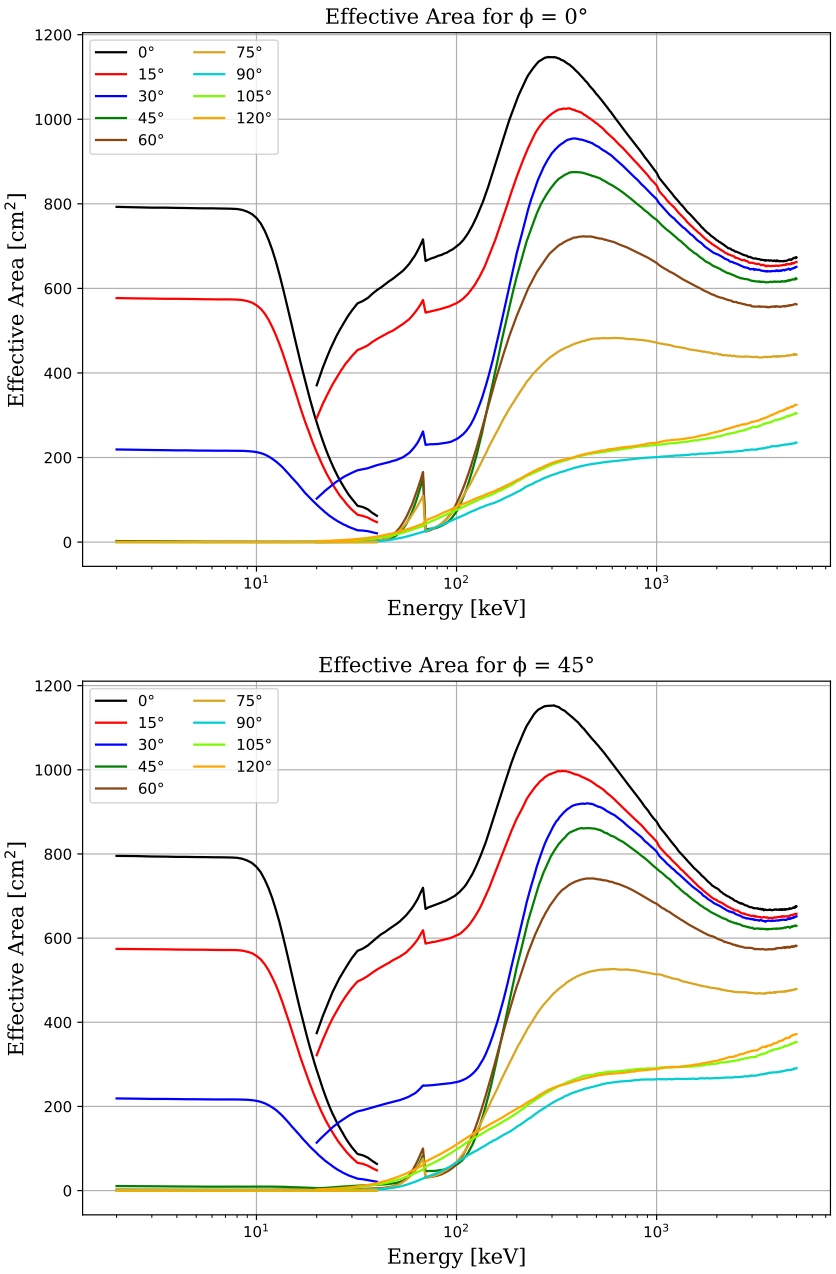

Figure 3.25: *Effective area with the simple mass model and a random mask pattern, for $\phi = 0°$ (left) and $\phi = 45°$ (right). The curves, up to 40 keV, show X-mode events, while at higher energies they show S-mode events. For off-axis angles above 45°, the effective area at low energies is null, whereas at higher energies, detection remains possible even for large off-axis sources. At ∼67 keV the K-shell edge of tungsten is noticeable.*

Preliminary test

During the XGIS M5 design phase, various trade-offs have been made to optimize its performance (Mereghetti et al., 2020). Among these, the choice of the tungsten mask thickness has played a crucial role, as it determines the mask transparency to radiation (transparency functions $T_C(E)$ and $T_O(E)$) and the energy range over which the XGIS instrument operates as an imager.

Therefore, a preliminary study on the thickness of the coded mask has been carried out in this work to evaluate its impact on the effective area. This has been assessed through on-axis simulations for two different mask thicknesses: 200 μm and 1000 μm. These cases have also been compared to the previously simulated 500 μm case, which is currently the reference value adopted in the XGIS design. The results of the effective area analysis are presented in Fig. 3.26.

For energies below 30 keV, the effective area remains unchanged, as tungsten efficiently blocks low-energy photons regardless of thickness. However, significant differences emerge at higher energies, where photons are detected in S-mode.

For a 200 μm thick mask, transparency increases at lower energies. This is evident from the fact that, around 40 keV, the effective area increases, reaching and exceeding 50% of the geometric area ($\sim$800cm^2). This indicates that the mask elements begin to transmit radiation. A drop in effective area is observed due to the K-shell absorption edge of tungsten at $\sim$67 keV, after which the effective area starts increasing again. In this scenario, the detector operates in imaging mode up to 100 keV, above which the FOV is no longer limited by the collimator. Moreover, the peak effective area is reached at lower energies and attains higher values, exceeding 1200 cm^2.

Considering that a thinner 200 μm mask weighs only 0.61 kg compared to 1.54 kg for the 500 μm mask, reducing the mask thickness would lower the payload mass. This could benefit the XGIS instrument, potentially allowing mass reallocation to other payload components. However, this reduction comes at the expense of a narrower imaging range.

Conversely, for a mask thickness of 1000 μm, the imaging range extends up to approximately 200 keV. However, this comes with a significant increase in payload mass and higher material costs, reaching 3.07 kg. One effect of this increased thickness is the disappearance of the K-shell edge feature due to the complete absorption of photons within its energy range. Additionally, the peak effective area is lower and shifted to higher energies.

This analysis confirms that, in the design phase of a space mission, the trade-offs involved are numerous and highly complex, requiring careful evaluation of multiple interdependent factors.

A tungsten mask with a thickness of 500 μm offers an excellent balance of performance.

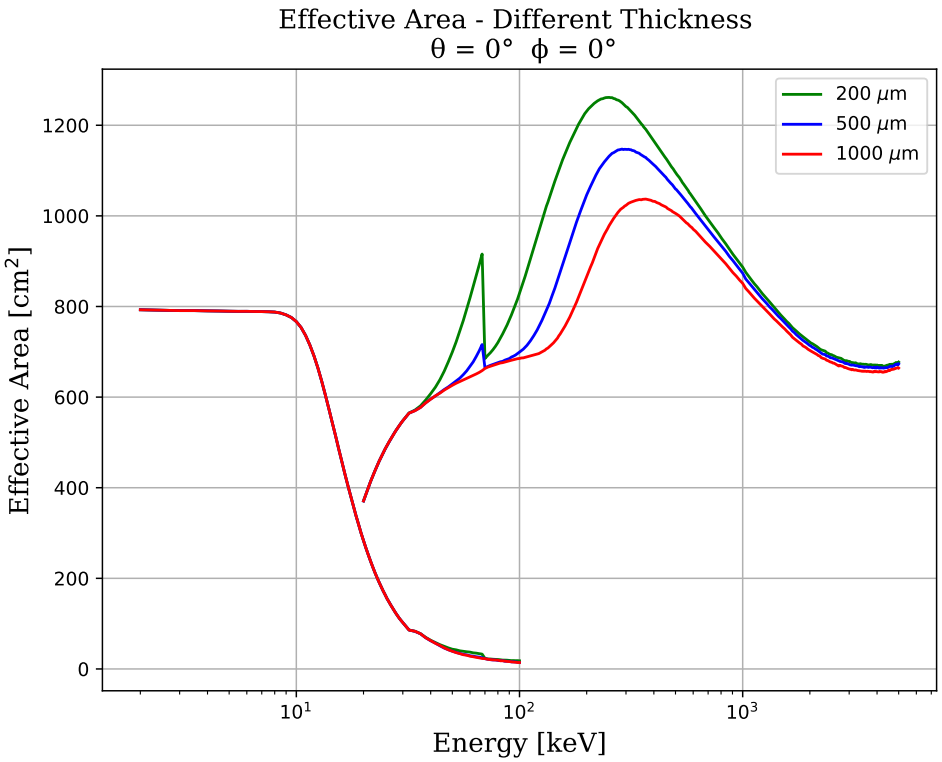

Figure 3.26: *Effective area obtained through on-axis simulations using mask thicknesses of 200, 500, and 1000 microns. While no differences are observed at low energies, for energies above 30 keV, the thickness affects the transparency of the mask, progressively increasing the imaging range of XGIS.*

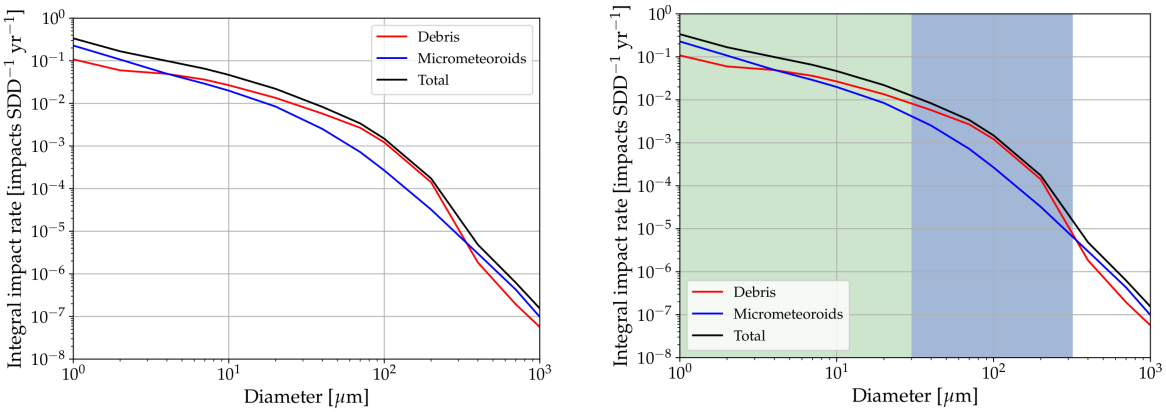

Figure 3.27: *Left: Expected integral rate of debris (red) and micrometeoroids (blue) on the XGIS SDDs without shielding. Right: Expected integral rate of debris (red solid line) and micrometeoroids (blue solid line) on XGIS SDDs with the combined shielding discussed in the text. The black solid line indicates the total integral flux (debris and micrometeoroids). The region in green indicates the diameters of the particles that are stopped either if the beryllium layer is above the detection plane or below the coded mask. The region in blue indicates the parameters of the particles that are stopped only if the beryllium layer is above the detection plane but are able to pass through if the beryllium is below the coded mask. Source: THESEUS Collaboration.*

Upgrades to simple mass model

The decision to add new elements to the mass model, not included in the original design, comes from further studies within the THESEUS Collaboration[8] aimed at shielding the detector from potential hypervelocity particle impacts, specifically from micrometeoroids and orbital debris (MMODs), to which spacecraft in Earth orbit are exposed. The study considered specific models of debris and micrometeoroid fluxes, which are defined as the number of intercepted objects per unit time and area. The relevant area for this flux is the actual outer surface area of a spacecraft element, for which an isotropic distribution of MMODs is assumed. For the analysis of impacts from debris, the model by Oswald et al. (2005) is assumed, considering a particle density of 2.8 g/cm^3 and a velocity of 13 km/s. The flux of micrometeoroids is estimated using the model by Grün et al. (1985), assuming particles with a density of 2.5 g/cm^3 impacting at normal incidence with a velocity of 20 km/s.

The number of impacts expected on the detection plane of XGIS is primarily due to its large FoV. A significant fraction of XGIS SDDs is estimated to experience at least one impact per year from debris and micrometeoroids, roughly one SDD every five. Since the majority of these impacts will create craters deeper than the thickness of the passive

[8]Reported in the THESEUS Technical Note: XGIS Instrument Radiation Effects

layers covering the SDD, thus reaching the silicon bulk, a shielding system for XGIS was studied.

The study identified the *Whipple Wall* as the most effective shielding strategy. A Whipple Wall consists of a thin bumper and a rear wall, separated by an interior spacing. For XGIS, the *multi-layer insulation* (MLI), that would have been introduced anyway for thermal-control purposes, would serve as the bumper, while a *Polypropylene* layer would act as the rear wall. The MLI is composed of a 7.6 μm Kapton layer coated with 100 nm of Aluminum. For an orthogonal component of the particle velocity v_{particle} >7 km/s, the minimum critical diameter (d_{crit}) of particles capable of penetrating the structure is given by Christiansen et al. (2009):

$$d_{\text{crit}} = 3.918\, t_{\text{Wall}}^{2/3}\, \rho_{\text{particle}}^{-1/3}\, \rho_{\text{bumper}}^{-1/9} (v_{\text{particle}}\, \cos\theta)^{-2/3}\, d^{1/3} (\sigma_{\text{Wall}}/70)^{1/3} \tag{3.7}$$

where t_{Wall} is the thickness of the rear wall in cm, ρ_{particle} is the density of the particle in g/cm^3, ρ_{bumper} the density of the bumper in g/cm^3, v_{particle} the velocity of the particle (assumed as orthogonal to the shield) in km/s, d is the distance between the bumper and the rear wall in cm, and σ_{Wall} the yield stress of the rear wall in kilobarn[9].

The critical diameter is ∼0.7 μm for debris and ∼0.6 μm for micrometeoroids in the case of the XGIS MLI. This estimation indicates that even small particles can pass through the XGIS MLI.

To mitigate the expected number of MMODs impacts, an additional rear wall made of a 25 μm layer of beryllium or, equivalently and more conveniently from a mechanical point of view, a 15 μm polypropylene layer was introduced, positioned 10 cm above the SDDs (53 cm below the MLI). With this additional shielding, the critical diameter increases to ∼230 μm for debris and ∼130 μm for micrometeoroids, resulting in an expected cumulative impact rate of 1.5×10^{-5} impacts/SDD/year.

In conclusion, the expected rate of MMODs capable of reaching the XGIS SDDs is extremely low when adopting a Kapton-beryllium or Kapton-polypropylene Whipple Wall shielding, remaining below 10^{-5}, as shown in Fig 3.27.

The following figures show how the effective area changes due to the implementation, in the simple mass model, for on-axis simulations, of the MLI (Fig. 3.28), the polypropylene layer (Fig. 3.29), and their combined effect (Fig. 3.30). The impacts are mainly noticeable at energies up to 10 keV: a drop in the effective area is observed compared to the simulation done with the mask only. This is consistent with the transmission curves, which foresee at 2 keV, for the polypropylene layer, a transmission of ∼70% of the radiation, while for the Kapton and aluminum layer, it is ∼56%, considering the previously mentioned thicknesses.

When combining the total effect of the Whipple Wall, an overall more pronounced reduction of the effective area at low energies is noticeable, with a total transmission effect

[9]The barn is the unit of cross-section measurement. 1 barn=10^{-24} cm^2.

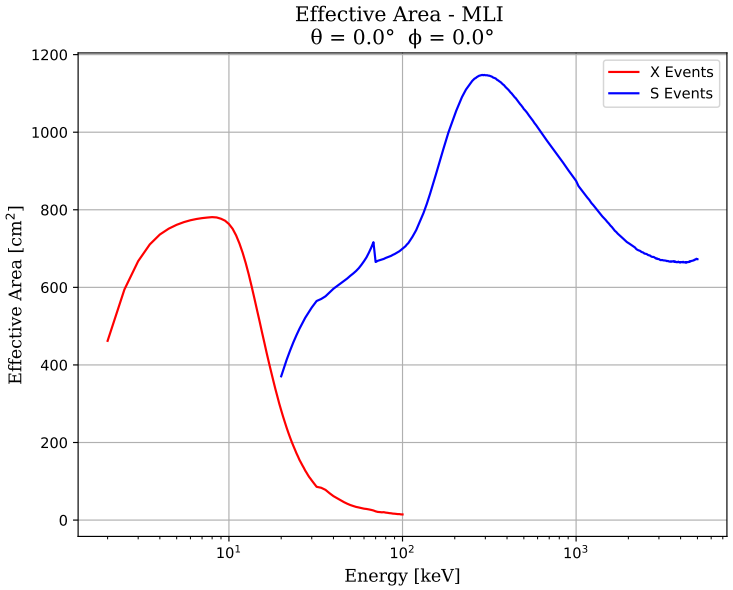

Figure 3.28: *Effective area obtained through on-axis simulations with the addition of MLI in the mass model; the reduction effect is noticeable at low energies.*

of 45%. The effect is practically absent for the S-mode. The reduction in the effective area at low energies, however, does not significantly affect the imaging capabilities of XGIS.

The last volume to be added concerns part of the Top Front End (Top FE) *printed circuit board* (PCB), which houses the preamplifiers that carry the signal to the bottom back-end electronics. The choice to place them above the illuminated detector area, thus partially obstructing the SDDs, is driven by the fact that the closer they are to the SDD anodes, the lower the induced electronic noise, as the connection wires will be shorter.

The PCB has been implemented in the mass model as plates covering the entire length of the detector, with a width of 3 mm and a thickness of 1.6 mm, obstructing a total of 30% of the detector. The material used, FR4 (a mixture of glass fiber and epoxy resins), with the chosen thickness, has the effect of sharply cutting off the detection of low-energy photons in the areas obscured by these structures.

Complete mass model

In Fig. 3.32, the volumes added to the mass model are shown: the Whipple Wall, composed of MLI and polypropylene, and the PCB located above the detector plane.

In Fig. 3.33, the effective area is shown for all 18 simulated directions with the complete mass model. The main difference compared to the effective area of the simple

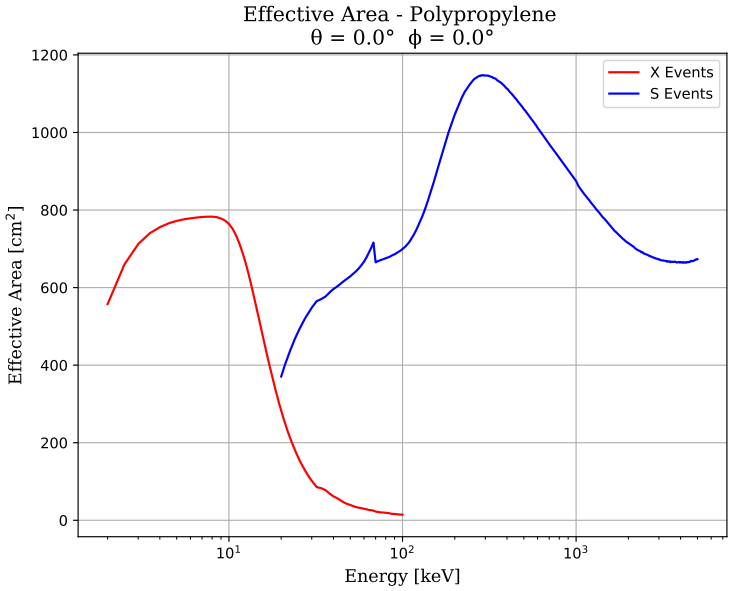

Figure 3.29: *Effective area obtained through on-axis simulations with the addition of polypropylene layer in the mass model; the reduction effect is noticeable at low energies.*

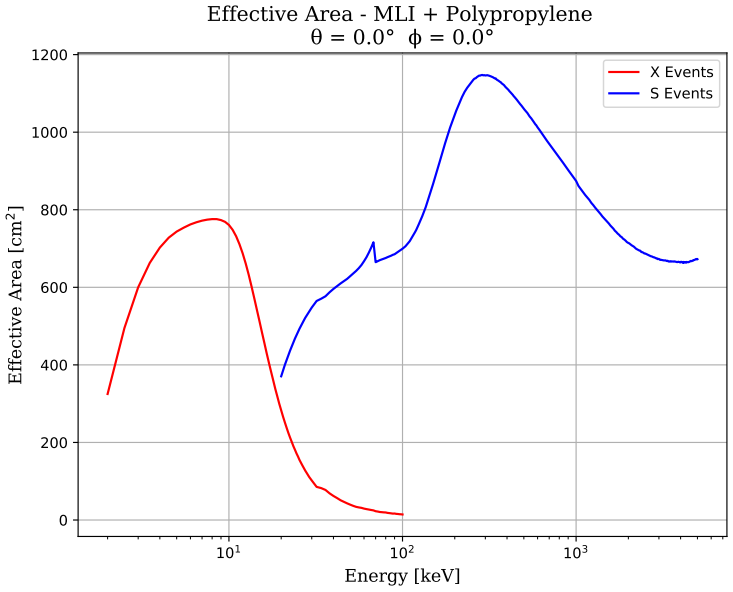

Figure 3.30: *Effective area obtained through on-axis simulations with the addition of MLI + polypropylene layer in the mass model; the overall reduction effect is noticeable at low energies.*

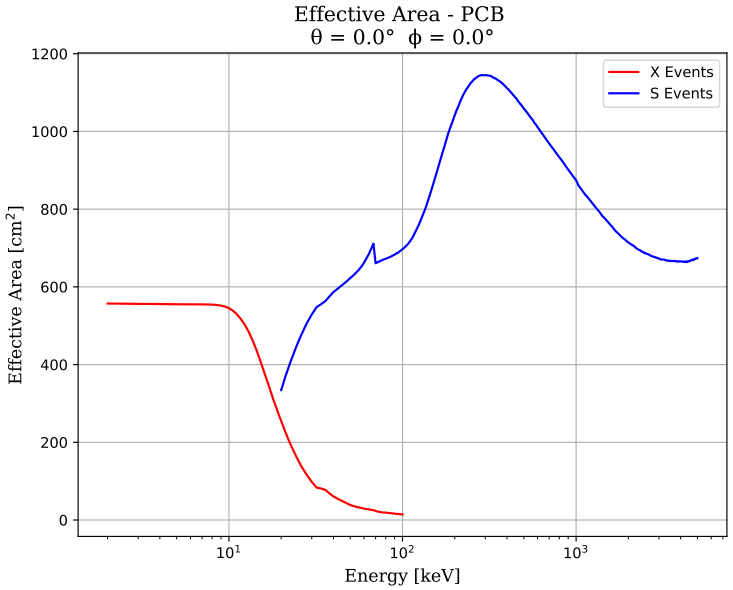

Figure 3.31: *Effective area obtained through on-axis simulations with the addition of PCB in the mass model; the sharp reduction effect is noticeable at low energies.*

model is observed for low-energy events detected in X-mode. The effects of the additional structures, analyzed earlier, are significant up to 10 keV. At higher energies, the complete mass model does not obstruct the transparency of the structures, and the effective area increases similarly to the simple model.

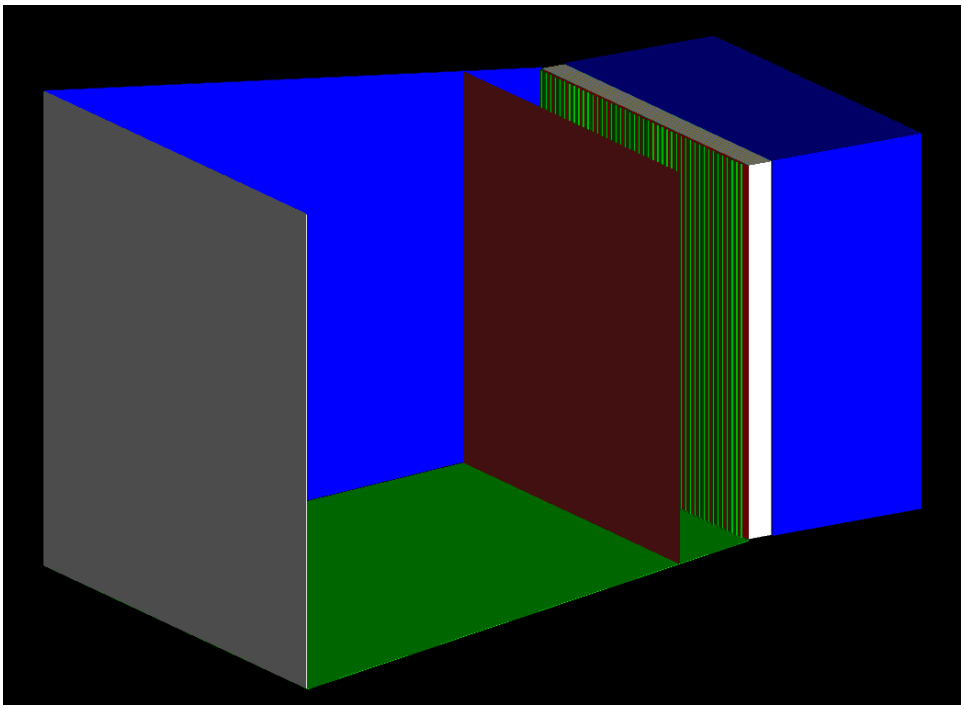

Figure 3.32: *Internal view of the XGIS mass model. Starting from the left, the MLI is shown in gray, completely covering the coded mask. The polypropylene layer is in brown, and the vertical bars of the PCB are in green. The green plane at the bottom represents the tungsten collimator structure, adjacent to which, in blue, is the aluminum structure that provides stability. The white structure contains the scintillators, while the blue aluminum structure connects XGIS to the spacecraft.*

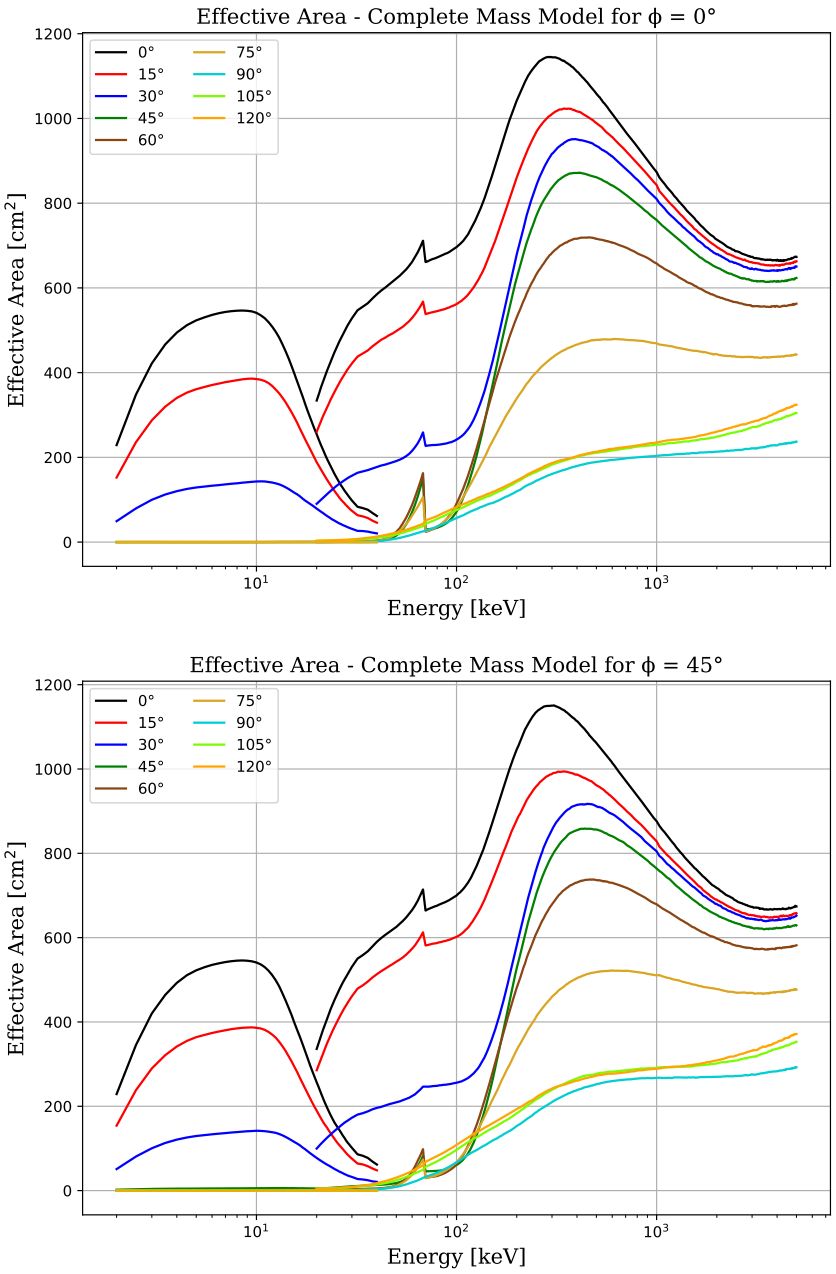

Figure 3.33: *Effective area with the complete mass model and the random mask pattern, for $\phi = 0°$ (top) and $\phi = 45°$ (bottom). The curves, up to 40 keV, show X-mode events, while at higher energies S-mode events are displayed. For off-axis angles beyond 45°, the effective area at low energies is null, whereas at higher energies, detection remains possible even for large off-axis sources.*

3.3.2 Response matrix

Depending on the type and energy of the incident particle, as well as the detector type, a monoenergetic source produces a pulse-height distribution that may be Gaussian or follow a more complex function. In either case, although all particles are emitted with the same energy at the source, there is a probability that they may be recorded within a range of energies. This implies that an event in a given detector PHA channel does not directly reveal any meaningful information about the astrophysical object being observed; rather, it encodes the energy of the incident photon according to a relationship that depends on both the photon energy and the position on the detector where it is recorded. This information is encapsulated in the detector Response Matrix, also called the Redistribution Matrix.

The astrophysically relevant information is obtained by unfolding the measured spectrum using the Redistribution Matrix. In fact, the measured spectrum of the source $M(E)dE$, which represents the number of particles recorded with energies between E and $E + dE$ and coincides with the pulse-height distribution, in linear approximation, is given by (Tsoulfanidis, 2015):

$$M(E) = \int_0^\infty R(E, E')\, S(E')\, dE' \tag{3.8}$$

where:

- $R(E, E')dE$ is the probability that a particle emitted by the source with energy E' will be recorded with an energy between E and $E + dE$; it can be expressed also in terms of $A(E)$, effective area as a function of energy;
- $S(E)dE$ is the source spectrum, i.e., the number of particles emitted by the source with energy between E and $E + dE$.

In this work, in order to determine the response function of XGIS within its energy range, the simulations described in the previous section have been performed.

In the ideal case, the redistribution matrix is a sharp and diagonal function, which is possible to invert to get the detector response. Actually, as found for XGIS, this is not a diagonal function, and the measured spectra should be fitted taking into account this non-diagonal response. This arises from the fact that the detector response will have a low-energy tail and various other spectral components for a given input energy.

In Fig. 3.34 and Fig. 3.35, the response matrices obtained, on-axis, using the simple and complete mass models are compared, respectively, for X-mode and S-mode. Input energies versus PI channel are plotted; in particular, 57 channels have been used for X-mode, while 317 channels for S-mode.

The response matrix for X-mode is essentially diagonal, being dominated by photoelectric full-energy depositions. Instead, the response for S-mode has a significant

contribution from non-diagonal elements (low-energy tail) due to the effects discussed in Sect. 3.2.2 such as the photopeak with its intrinsic broadening, single and double-escape peaks, Compton scattering and fluorescence.

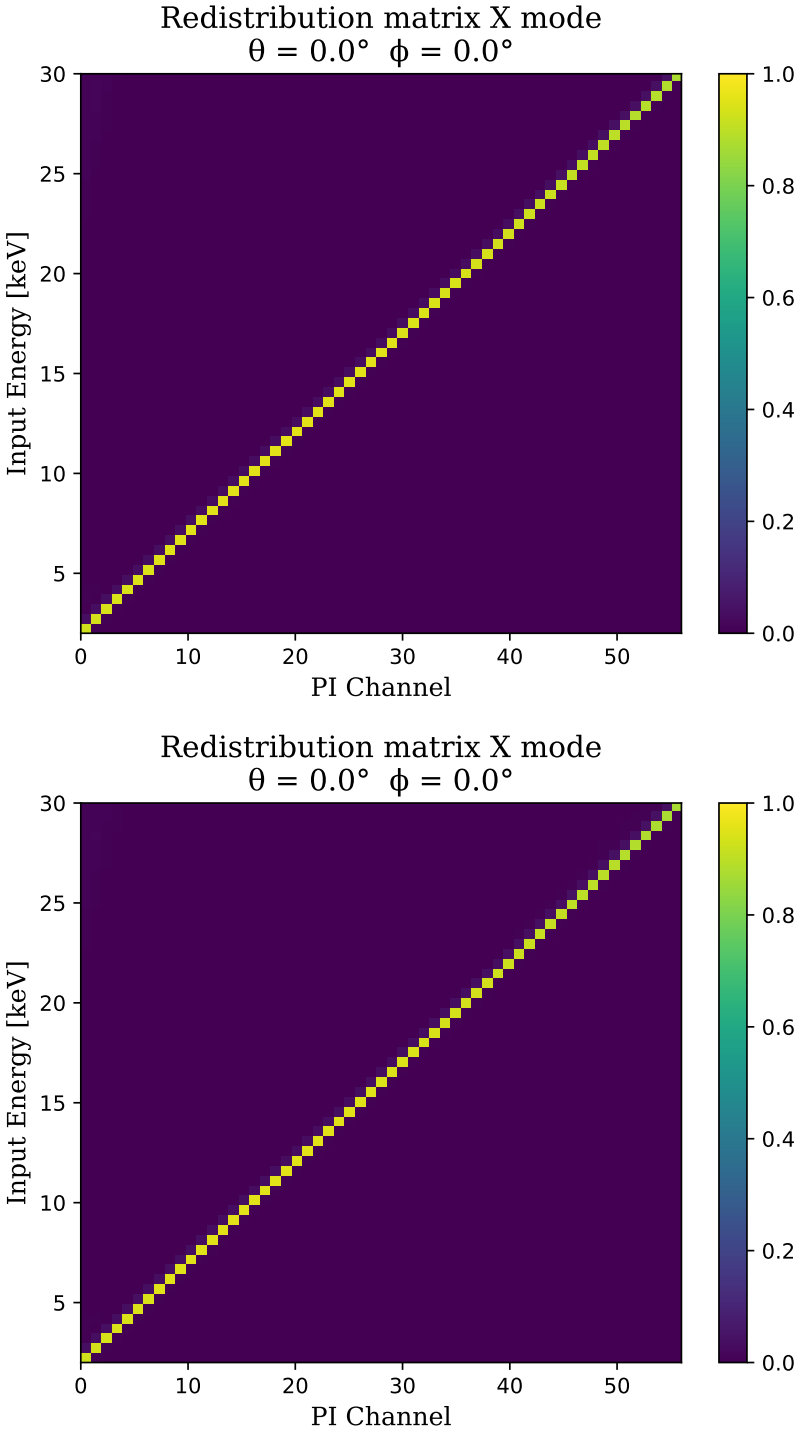

Figure 3.34: *Response matrix for X-mode with simple (top panel) and complete (bottom panel) mass model. In this energy range, the redistribution is essentially diagonal, being dominated by photoelectric full-energy depositions.*

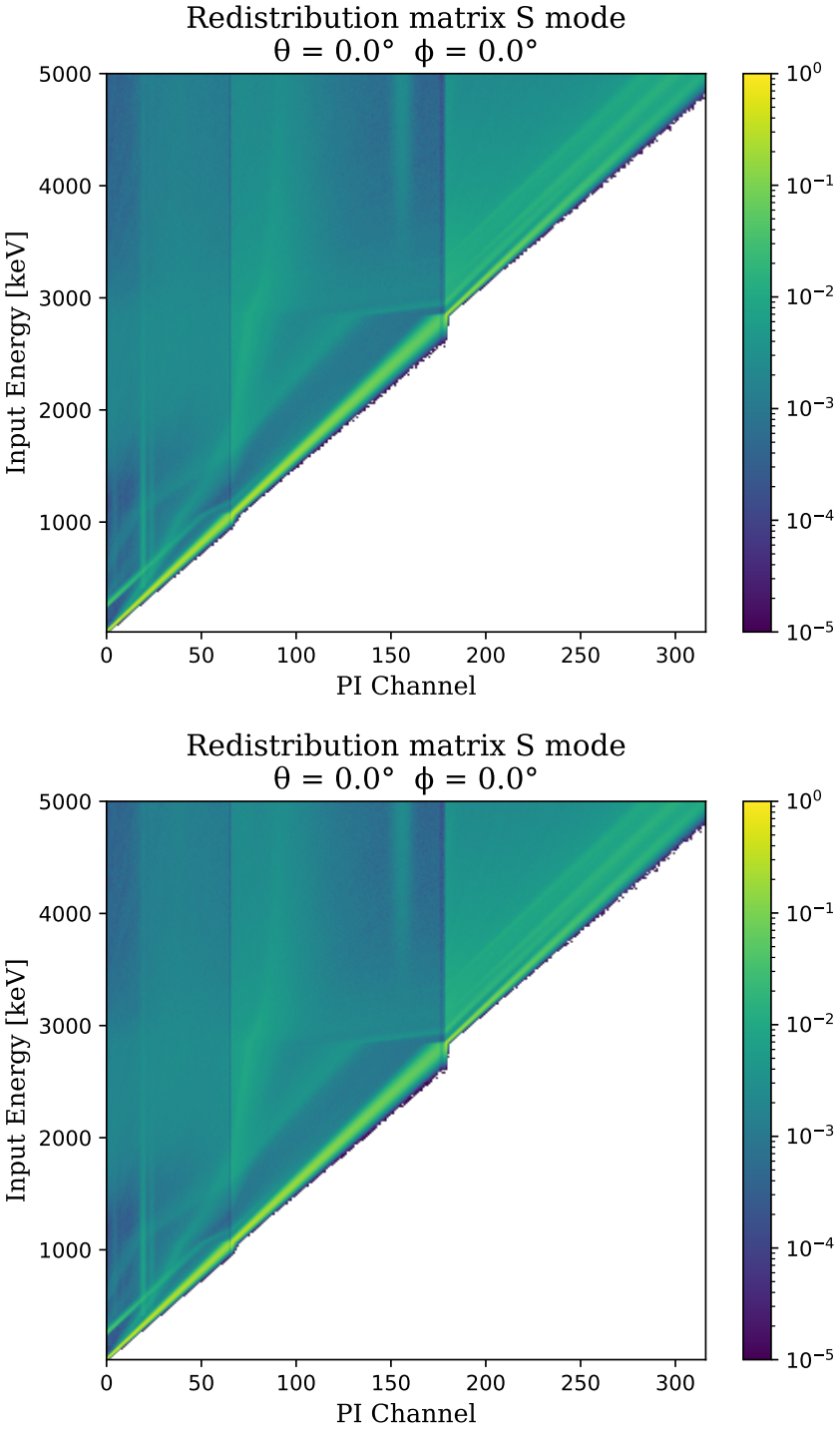

Figure 3.35: *Response matrix for S-mode with the simple (top panel) and complete (bottom panel) mass model. Note the logarithmic color scale which emphasizes the off-diagonal elements of the redistribution, mostly due to Compton-scattered events.*

3.4 Summary

The performance of XGIS has been evaluated in terms of effective area and instrument response through Monte Carlo simulations conducted with Geant4, a standard tool for such analyses. The performance was assessed separately for detection in X-mode (2–30 keV) and in S mode (20–5000 keV).

The simulations have been performed using the mass model developed during the THESEUS M5 study, to which a random mask pattern has been added (with different thickness values), and then compared with the same model after several improvements in modeling accuracy have been introduced. In particular, the simplest model with random pattern mask yields an effective area of $\sim$800 cm^2 in X-mode, consistent with the fact that the mask pattern has an open fraction of 50%. Instead, the effective area for the updated model is in line with a 72% reduction in count rate in the whole 2–30 keV band, attributable to the diminished contributions of each introduced component (MLI, polypropylene, PCB).

No differences were observed between the two mass models for the in S-mode effective area, which peaks at slightly less than 1200 cm^2 at $\sim$300 keV, since the implemented additional layers affect only low energies.

The effective area is verified to be compliant with the mission requirements.

Finally, the response matrices were found: for X-mode, it is essentially diagonal, while for S-mode, in addition to the diagonal contribution, a low-energy tail is present.

Upcoming improvements to the performance evaluations will include finer sampling of the energy, zenith angle, and azimuthal angle space, as well as simulations involving a larger number of primary events (at least an order of magnitude greater). A better mass model (derived from CAD model) for the simulations will be exploited, provided by the University of Valencia working group responsible for the XGIS coded mask design and implementation. Furthermore, the height within the scintillator bars where the interaction occurs will be introduced as part of the simulation outputs, allowing for a more accurate event reconstruction (also from an electronic noise point of view). The effective area of the XGIS system will also be studied by combining the contributions from both XGIS cameras.

The outputs obtained here are useful for upcoming scientific simulations of XGIS performance and actively contribute to the current study phase of the entire M7 THESEUS mission, contributing to the update of the official documents provided to ESA for this phase.

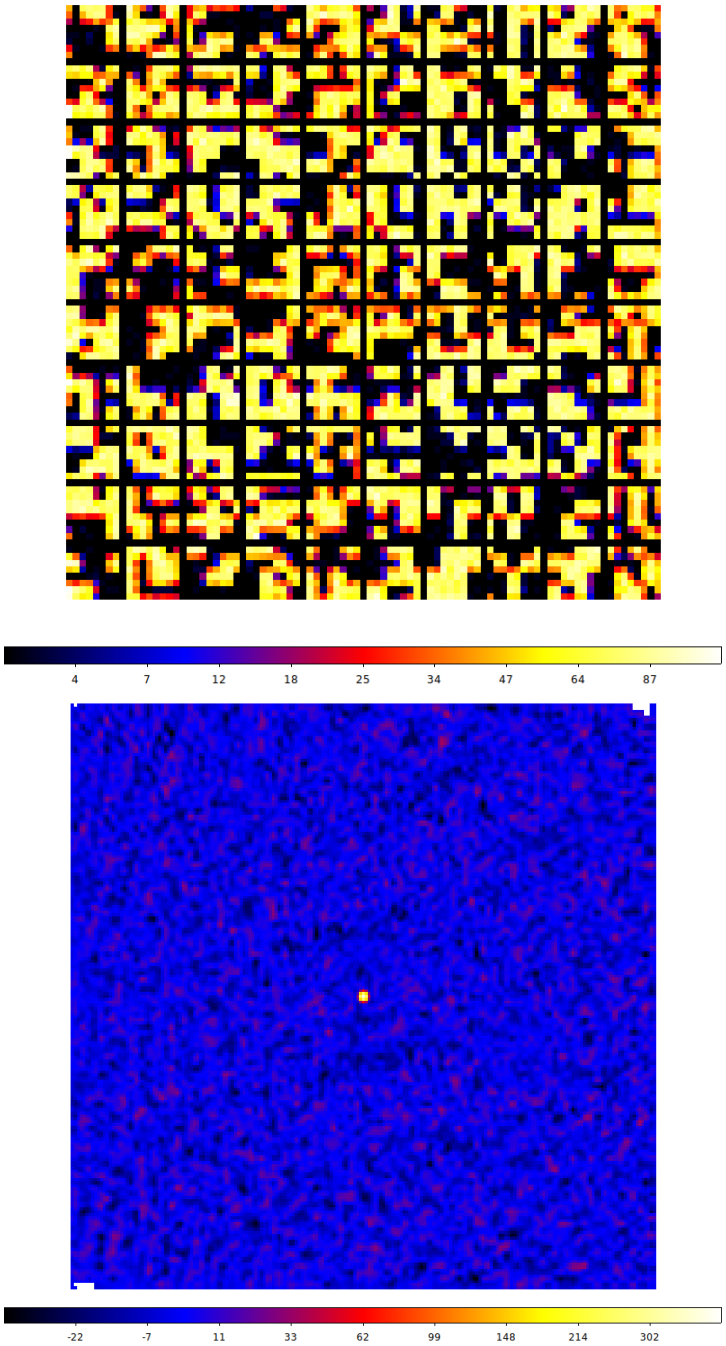

Figure 3.36: *(Top) Shadowgram projected by a simulated GRB on-axis with a typical Band function spectrum (see Sect. 1.1) with slope $\alpha = -1$, $\beta = -3$, and E_{break}=300 keV. (Bottom) Deconvolved image showing a count spike corresponding to the point-like GRB. The images have an asinh color scale.*

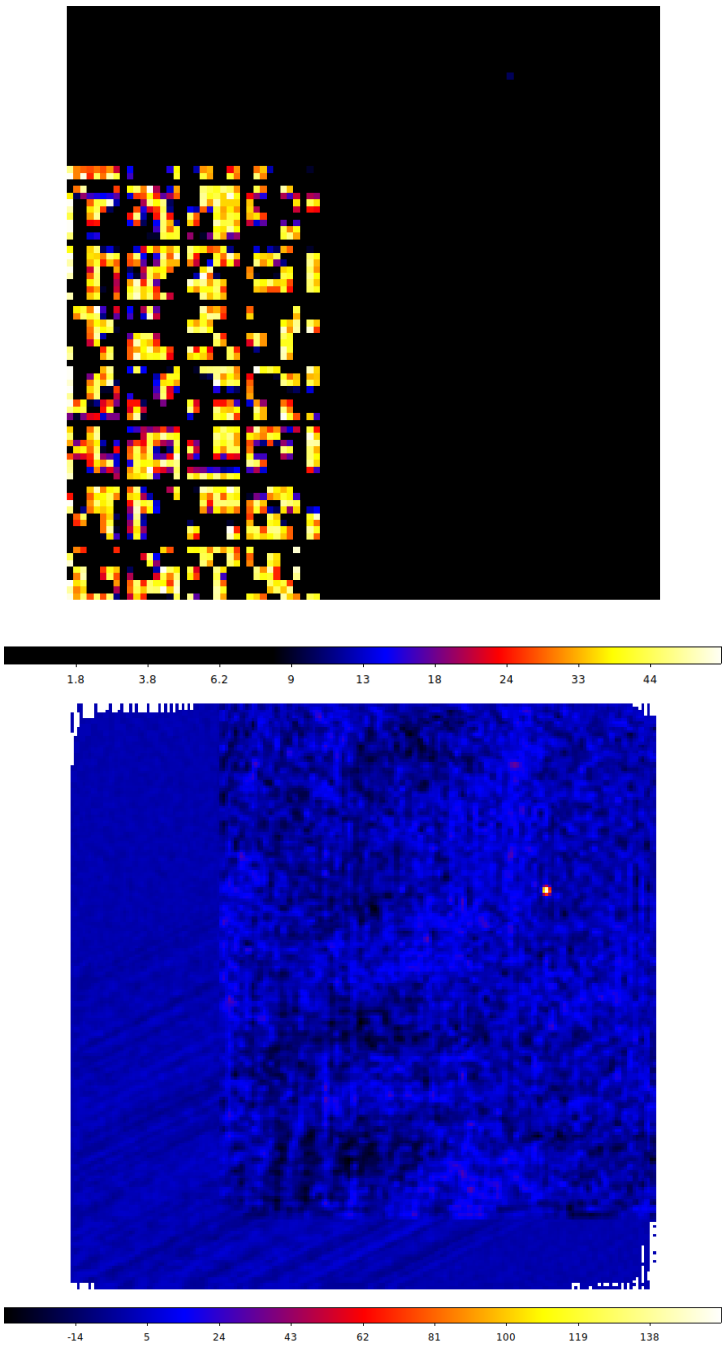

Figure 3.37: *(Top) Shifted shadowgram projected by a simulated GRB off-axis ($\theta = 30°$, $\phi = 30°$) with a typical Band function spectrum with slope $\alpha = -1$, $\beta = -3$, and E_{break}=300 keV (linear color scale). (Bottom) Deconvolved image showing in the top-left part a count spike corresponding to the point-like GRB; secondary structures are also visible around the GRB (asinh color scale).*

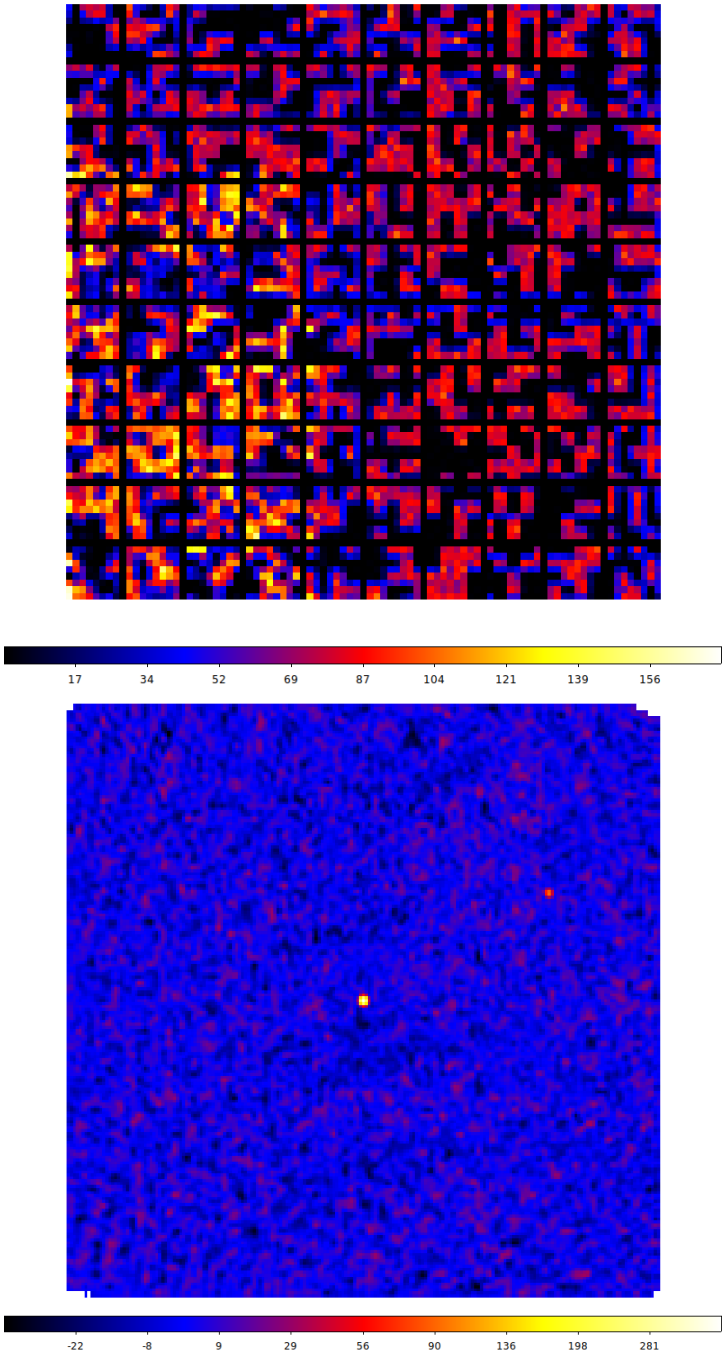

Figure 3.38: *(Top) Overlapped shadowgrams projected both by a simulated on-axis and off-axis GRB ($\theta = 30°$, $\phi = 30°$) with a typical Band function spectrum with slope $\alpha = -1$, $\beta = -3$, and $E_{\rm break}$=100 keV. (Bottom) Deconvolved image showing both counts spike of the two GRBs. The images have linear color scale.*

Chapter 4

In-orbit background simulations

In this chapter, Monte Carlo simulations performed using Geant4 have been exploited to evaluate the contribution of different background sources to XGIS, separately for X-mode and S-mode.

An accurate assessment of the expected in-orbit instrumental background is essential for evaluating the scientific performance of the experiment. The sensitivity of XGIS, in fact, depends on the combination of several factors, the most important of which are the effective area and the background itself.

As already discussed in Chapt. 2, an essential requirement for the THESEUS mission is the stability of background levels. Ensuring a stability larger than 10% on a timescale of 10 minutes is crucial to enable a highly sensitive triggering capability and to optimize the characterization of transients, in particular for measuring key physical parameters such as fluence, duration, the start and end times of the phenomenon.

Therefore, after a detailed description (Campana, 2022) of the background sources affecting all high-energy detectors operating in Low Earth Orbit (LEO) and used as input for the simulations, the contributions of each background source will be presented, leveraging both the simple mass model and the complete mass model described in Chap. 3.

Finally, the strategies implemented in the XGIS design to reduce the background noise will be discussed.

4.1 Background sources in Low Earth Orbits

The sensitivity of an instrument is influenced not only by intrinsic noise (see Chapt. 3) but also by external factors: every detector experiences extrinsic noise originating from the environment in which it operates, that can affect its ability to measure signals and impact its observations of cosmic sources. The photon counts resulting from an observation that do not originate from the source under study are referred to as background.

The properties of the background are determined by the detector design, the charac-

teristics of the operational environment, and the type of measurements being conducted. To ensure an accurate interpretation of scientific data, a thorough understanding of the background is essential (Campana, 2022).

The raw data from the observations, indeed, include events resulting from high-energy photons as well as high-energy particles interacting with the detector. These particle events can originate from various sources and, upon interacting with the detector, generate charge that mimics the behavior of high-energy photons, leading to spurious counts.

XGIS will operate at a nominal altitude between 550 km and 640 km, corresponding to a mostly circular Low Earth Orbit (LEO), with a low inclination of 5.4° and an orbital period of about 97 minutes. This specific inclination, combined with the chosen operational altitude, ensures a suitable environment for THESEUS performance, as already shown by previous missions such as BeppoSAX and AGILE. The lower altitude limit for an orbit is determined by atmospheric braking-induced orbital decay.

The spacecraft design enables payload operations also during eclipses, which occur once per orbital revolution around the Earth, last about 35 minutes under the nominal reference orbit parameters, with duration variations of approximately 10 seconds for every 50 km change in altitude (Fig. 4.1).

LEOs offer several advantages, primarily by providing a low and relatively stable overall background environment, which is essential for satisfying the XGIS requirements: "stability shall remains within 10% over timescales of <10 minutes throughout the mission in-orbit lifetime and outside the South Atlantic Anomaly region"[1].

Several past and current GRB experiments operating in the 10–20 keV to a few MeV energy range aboard space missions such as CGRO/BATSE, BeppoSAX/GRBM, Swift/-BAT, Fermi/GBM, and Konus/WIND have demonstrated that a stable background over this timescale is crucial for enabling sensitive triggering capabilities. Even though typical GRBs dominate the background during their peak and bulk emissions, the more interesting events are typically the weakest.

Another important aspect of LEOs is that the required launcher Δv, i.e. the impulse per unit mass needed for orbital insertion (a measure of the fuel required for the launch), is relatively small. This results in higher allowable payload masses, making it more efficient for carrying larger instruments or payloads.

Being close to Earth surface means to receive significant radiation emitted by the Earth itself, known as albedo radiation. Additionally, at altitudes around 600 km, about 30% of the sky is obstructed by the Earth (see next Section), leading to considerable source occultation time. A well-planned pointing strategy can help reducing this effect (see caption in Fig. 4.1)

Moreover, orbiting close to Earth, in particular at low equatorial inclinations, provides near-complete shielding of the spacecraft by the geomagnetic field against damaging

[1]THESEUS/M7: Science Requirements Document.

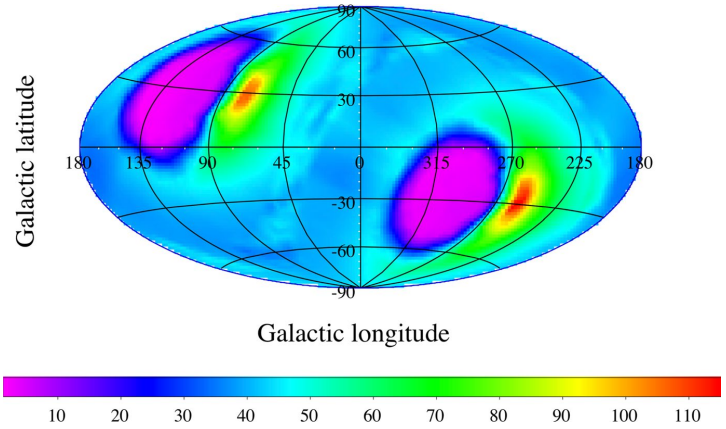

Figure 4.1: *The expected sky exposure for the SXI instrument, computed from simulations assuming a nominal mission duration of 4 years. The color scale represents exposure in units of days. Due to its larger FoV, the sky exposure of XGIS is significantly larger. In Survey Mode, SXI and XGIS will be capable of detecting GRBs and other transient sources within their FoV. Various pointing strategies have been evaluated to optimize the trade-off between maximizing the number of detected GRBs and ensuring a distribution of their sky positions easily accessible to large ground-based facilities. To minimize Earth occultation of the FoV, two exposures are planned for each satellite orbit, directed toward positions with opposite right ascension (i.e., RA_i and RA_i +12h) and a declination of $\pm 30°$, depending on the season. This observing strategy will result in a non-uniform sky coverage, with most Survey Mode pointings lasting around 2.3 ks. (Mereghetti et al., 2021).*

solar particle events and Galactic cosmic rays, compared to much higher orbits such as HEO (Highly Elliptical Orbits, apogee >36.000 km, Fig. 4.2). Another advantage is the possibility to exploit the Earth magnetic field for fast slewing of the spacecraft (by exploiting reactions wheels and magnetic torquers), as well as the facilitation of prompt transmission of transient triggers and positions to the ground. For THESEUS, the main ground station will be located in Malindi (Kenya) and will be operated by the Italian Space Agency.

The Earth is surrounded by its geomagnetic field, which is generated by the convection currents in the molten outer core. At the surface of the Earth, the strength of the field is ∼0.5 G. In a simplified model (particularly accurate at lower altitudes), the geomagnetic field can be approximated as a tilted dipole, offset from the Earth center by around 500 km, and inclined by about 10° relative to the planet rotation axis. The complex interaction between the solar wind, cosmic rays and the geomagnetic field leads to the creation of two distinct regions where charged particles become trapped: *the Van Allen radiation belts*, distinguished into an in inner and an outer region (Fig. 4.3). The inner radiation belt spans from approximately 1.000 km to 12.000 km in altitude, primarily

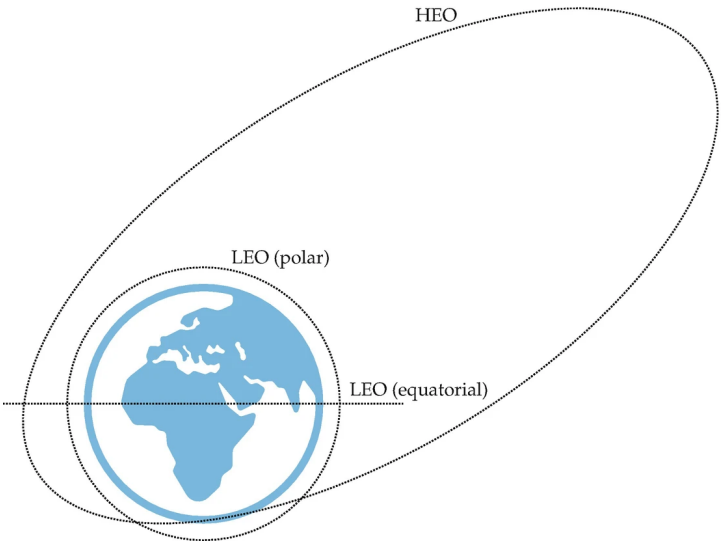

Figure 4.2: *Various types of Earth orbits: LEO polar, equatorial, and HEO (Campana, 2022).*

containing high-energy protons, with energies from MeV to GeV, and electrons up to a few MeV. The outer radiation belt extends from about 12.000 km to 60.000 km and is mainly composed of high-energy electrons with energies in the hundred of MeV.

The low altitude and inclination chosen for THESEUS allow to minimize the exposure to the Van Allen trapped charged particles encountered by the spacecraft, in particular avoiding the South Atlantic Anomaly (SAA).

The SAA is a region roughly located above the coasts of Brazil and the South Atlantic Ocean, where the magnetic field is weaker compared to an idealized Earth-centered dipole field, therefore Earth inner Van Allen radiation belt comes closest to the surface, reaching altitudes of 200 km. As a result, the flux of energetic particles in this region is elevated, exposing orbiting satellites to higher levels of radiation. The SAA is defined as the region of space where the flux of particles with energy >20 MeV exceeds the threshold of 1 proton cm^{-2} s^{-1} (European Space Agency (ESA), 2021). The geomagnetically trapped electrons and protons inside the inner Van Allen radiation belt (originating from solar winds and cosmic rays) populate this region and are responsible for the radioactivation of the instruments and spacecraft structures, as well as for the radiation damage to the detector itself.

The activation-induced background represents a minor, albeit non-negligible, contribution to the overall background (Campana et al., 2020). Nevertheless, this has not been simulated in the present work.

As shown in Fig. 4.4, the THESEUS low-inclination orbit will only graze the SAA in its outermost regions. This results in shorter transit durations and much lower trapped particle fluxes compared to a satellite in a higher inclination orbit which would pass

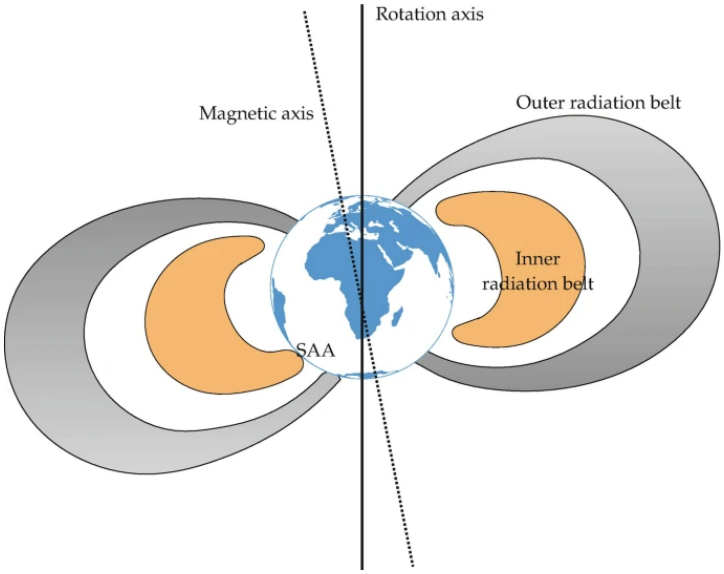

Figure 4.3: *The Van Allen radiation belts, including both the inner and outer radiation belts, are depicted, as well as the SAA region (Campana, 2022).*

through the "core" of the SAA. However, data collected by XGIS during the passage through the SAA will be discarded.

In the following sections, the main populations of *particles* and *photons* that contribute to the on-board *background* are described, and have been employed as the inputs for the Monte Carlo simulations.

4.1.1 Primary cosmic rays

The cosmic rays, composed by high-energy protons (∼85%), ions (∼13%), and electrons (∼2%) (Longair, 2011), are particles accelerated to relativistic velocities in different processes, originating from galactic and extragalactic sources. Interacting with the atmosphere, cosmic rays produce showers of secondary particles, which can reach the Earth surface but can also be reflected back into space.

The primary cosmic ray spectrum extends from an energy of a few MeV/nucleon to extremely high energies, above 10^{20} eV/nucleon. The differential spectrum is well described, above ∼1 GeV/nucleon, by a power-law distribution,

$$F(E) = dN/dE \propto E^{-\gamma}$$

where $\gamma \sim 2.7$.

The intensity of the cosmic ray flux is modulated by the 11-year solar cycle, with a variation in the total integral flux of cosmic rays at the Earth location of about a factor of two between solar minimum and maximum. The magnetic fields transported by the solar

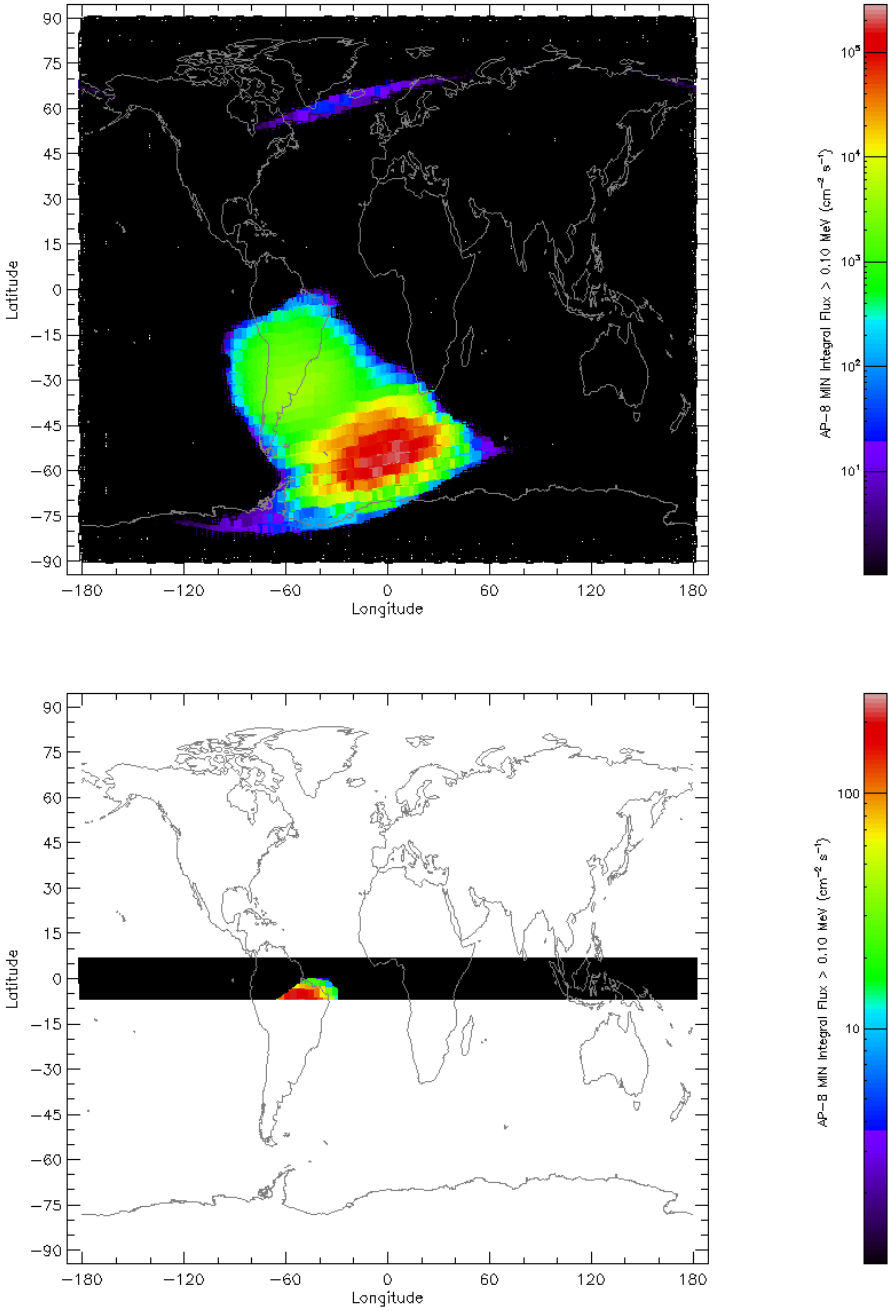

Figure 4.4: *Top panel: Map of the trapped proton integral fluxes, above 100 keV, at an altitude of 600 km, computed using the AP8 model at solar minimum. The region with the strongest emission is the SAA. Bottom panel: The equatorial orbit in which THESEUS will operate: the SAA will be only grazed. Source: SPENVIS.*

wind can deflect and scatter the incoming cosmic rays. The parameter that quantifies the effect of the solar cycle is the *solar modulation potential* Φ: at solar minimum it is 0.55 GV, while at solar maximum it is 1.10 GV (Gleeson and Axford, 1968). Moreover, the presence of the geomagnetic field modifies the trajectories of charged particles near the Earth, according to the *particle rigidity* $R = pc/q$, where p is the momentum, q the charge and c the speed of light (i.e., the momentum for unit charge, measured in volts). If an individual cosmic ray has a rigidity above a certain threshold, it can reach a given location in the magnetosphere. This threshold value is called cutoff rigidity, $R_{\rm cut}$, and is a complex function of the altitude, the geomagnetic latitude, and the incoming direction of the incident particle (see Stormer formula in Smart and Shea 2005). For the 600 km, 5.4° inclination THESEUS orbit, the cutoff rigidity is found to be in the range $R_{\rm cut}$ ∼10.1–12.1 GV.

By taking into account all these factors, the full differential spectrum for a primary cosmic ray particle of mass M, charge Ze, rigidity R, and kinetic energy E, at a location around the Earth given by an altitude h and a geomagnetic latitude λ, can be expressed by the following relation (Mizuno et al., 2004):

$$F(E) = F_U(E) \times F_M(E, M, Z, \Phi) \times C(R, h, \lambda) \tag{4.1}$$

in which F_U is the incoming, unmodulated, cosmic ray spectrum, F_M is an analytic solar cycle modulation factor, and C is a geomagnetic cutoff function (Campana et al., 2013).

The unmodulated cosmic ray flux can be described following the approximations by Mizuno et al. (2004), based on AMS measurements (AMS collaboration, 2000):

$$F_U(E) = K \times \left[\frac{R(E)}{GV}\right]^{-\gamma} \qquad [\text{particles cm}^2\ \text{s}^{-1}\ \text{sr}^{-1}\ \text{MeV}^{-1}] \tag{4.2}$$

where $R(E)$ is the rigidity in GV and K and γ are parameters which depend on particle type and geomagnetic latitude. In particular, for the primary particles used in the simulations, the following values obtained from the AMS observations were employed for the differential spectra:

- *protons*, $K = 23.9$, $\gamma = 2.83$
- *electrons*, $K = 0.65$, $\gamma = 3.3$
- *positrons*, $K = 0.051$, $\gamma = 3.3$
- *alpha*, $K = 1.5$, $\gamma = 2.77$

Only the primary helium nuclei have been considered, as the contribution of heavier nuclei is negligible with respect to the other primary particle fluxes (Zuccon, 2004).

4.1.2 Secondary particles

The interaction of cosmic rays with the Earth atmosphere produces a secondary component, "quasi-trapped" in the magnetic field lines. According to AMS measurements, this secondary component is composed of a short-lived and a long-lived particle population, both originating from the regions near the geomagnetic equator. Mizuno et al. (2004) model the secondary equatorial proton spectrum as a cutoff power-law:

$$F(E) = 0.123 \times \left(\frac{E}{1\,\mathrm{GeV}}\right)^{-0.155} e^{-(E/0.51)^{0.845}} \qquad [\text{particles cm}^2\ \text{s}^{-1}\ \text{sr}^{-1}\ \text{MeV}^{-1}] \quad (4.3)$$

and a power law for energies below 100 MeV:

$$F(E) = 0.136 \times \left(\frac{E}{100\,\mathrm{MeV}}\right)^{-1} \qquad [\text{particles cm}^2\ \text{s}^{-1}\ \text{sr}^{-1}\ \text{MeV}^{-1}] \quad (4.4)$$

Furthermore, the equatorial secondary electron spectrum can be approximated with a broken power law:

$$F(E) = 0.3 \times \left(\frac{E}{100\,MeV}\right)^{-2.2} \qquad \text{for} \quad 100\,MeV < E < 3\,\mathrm{GeV} \quad (4.5)$$

$$F(E) = 0.3 \times \left(\frac{3\,\mathrm{GeV}}{100\,\mathrm{MeV}}\right)^{-2.2} \left(\frac{E}{3\,\mathrm{GeV}}\right)^{-4} \qquad \text{for} \quad E \geq 3\,\mathrm{GeV} \quad (4.6)$$

and a power law for energies below 100 MeV:

$$F(E) = 0.3 \times \left(\frac{E}{100\,\mathrm{MeV}}\right)^{-1} \qquad [\text{particles cm}^2\ \text{s}^{-1}\ \text{sr}^{-1}\ \text{keV}^{-1}] \quad (4.7)$$

4.1.3 Photon background

The principal source of photon background for a spaceborne X-ray astronomy mission is the nearly isotropic diffuse cosmic radiation, the cosmic X-ray background (CXB), discovered during the very first X-ray astronomy experiments in the 1960s (Giacconi et al., 1962), which is the integrated emission of extragalactic point sources such as AGN, powered by supermassive black holes. The model assumed is given by Gruber et al. (1999) derived from HEAO-1 A4 and COMPTEL measurement. Below 60 keV:

$$F(E) = 7.877 \times \left(\frac{E}{1\,\mathrm{keV}}\right)^{-1.29} e^{-E/41.13} \qquad [\text{photons cm}^2\ \text{s}^{-1}\ \text{sr}^{-1}\ \text{MeV}^{-1}] \quad (4.8)$$

while above 60 keV it is described by the following formulas:

$$F(E) = 0.0004317 \times \left(\frac{E}{60\,\mathrm{keV}}\right)^{-6.5} \tag{4.9}$$

$$+ 0.0084 \times \left(\frac{E}{60\,\mathrm{keV}}\right)^{-2.58} \tag{4.10}$$

$$+ 0.00048 \times \left(\frac{E}{60\,\mathrm{keV}}\right)^{-2.05} \tag{4.11}$$

$$[\text{photons cm}^2\ \text{s}^{-1}\ \text{sr}^{-1}\ \text{keV}^{-1}] \tag{4.12}$$

Besides the extragalactic component, the diffuse photon emission includes also a galactic contribution, non uniform spatially, due to different classes of sources such as cataclysmic variables, coronally active binaries. The emission is strongest in the central radians of the galaxy (i.e., approximately for absolute galactic longitudes below 30° and latitudes below 10°), but a thin component all along the Galactic disk is still present at other longitudes (Revnivtsev et al., 2006).

Another source of photons background that has been employed in the simulations is the Earth γ-ray albedo radiation, which includes the reflection of CXB emission; this component is mainly produced through bremsstrahlung and π^0 decay processes during the interaction of the primary cosmic rays with the atmosphere, along with the showers of the already described secondary particles. The modeling developed by Ajello et al. (2008) based on Swift/BAT data has been used:

$$F(E) = \frac{0.0148}{\left(\frac{E}{33.7\,\mathrm{keV}}\right)^{-5} + \left(\frac{E}{33.7\,\mathrm{keV}}\right)^{1.72}} \qquad [\text{photons cm}^2\ \text{s}^{-1}\ \text{sr}^{-1}\ \text{keV}^{-1}] \tag{4.13}$$

Finally, neutron albedo radiation has been considered, originating from hadronic showers induced by the interaction of primary cosmic rays with the atmosphere. The resulting neutron flux will depend on the geomagnetic latitude, with a flux increase of about an order of magnitude for polar regions with respect to equatorial latitudes. The adopted model is the one suggested by ESA standards (ECSS, 2000).

Fig. 4.5 shows the average differential fluxes of each described component.

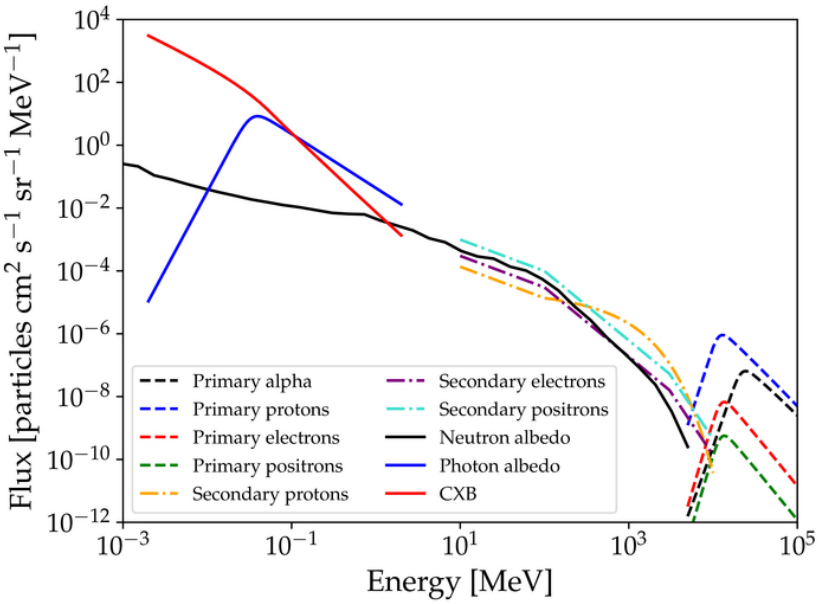

Figure 4.5: *Differential spectra of background sources in equatorial LEO expressed in terms of particles cm^{-2} s^{-1} sr^{-1} MeV^{-1}. Up to 10 keV, CXB and Photons Albedo components are dominant, while at higher energies, particles contribution prevails (Campana et al., 2020).*

4.2 Simulations

To study the impact of the previously described background sources, macro files containing the differential spectrum of each source have been provided as input to the Geant4 application. Unlike the simulations performed for the effective area and response matrix, this time the input sources have been simulated isotropically on a sphere surrounding the XGIS mass model, as shown in Fig. 4.6. Once again, both the simple and upgraded mass models have been used, and the same pipeline has been exploited in order to obtain cleaned data, divided among X-mode and S-mode events (see Sect. 3.2.4).

The initial events (particles or photons) are generated on the surface of a sphere of radius R (see Fig. 4.7), with a cosine-biased emission angle to ensure an isotropic flux. The emission angle is further restricted between 0 (normal to the spherical surface) to $\theta_{\max}$: the emission cone then subtends a smaller sphere of radius r that surrounds the detector. In particular:

$$\theta_{\max} = \arctan\left(\frac{r}{R}\right)$$

Calling Φ the energy-integrated flux between $E_{\min}$ and $E_{\max}$, expressed in particles cm^{-2} s^{-1} sr^{-1}, then the total rate is:

$$N_r = \Phi\, 4\pi^2 R^2 \sin^2\theta_{\max}$$

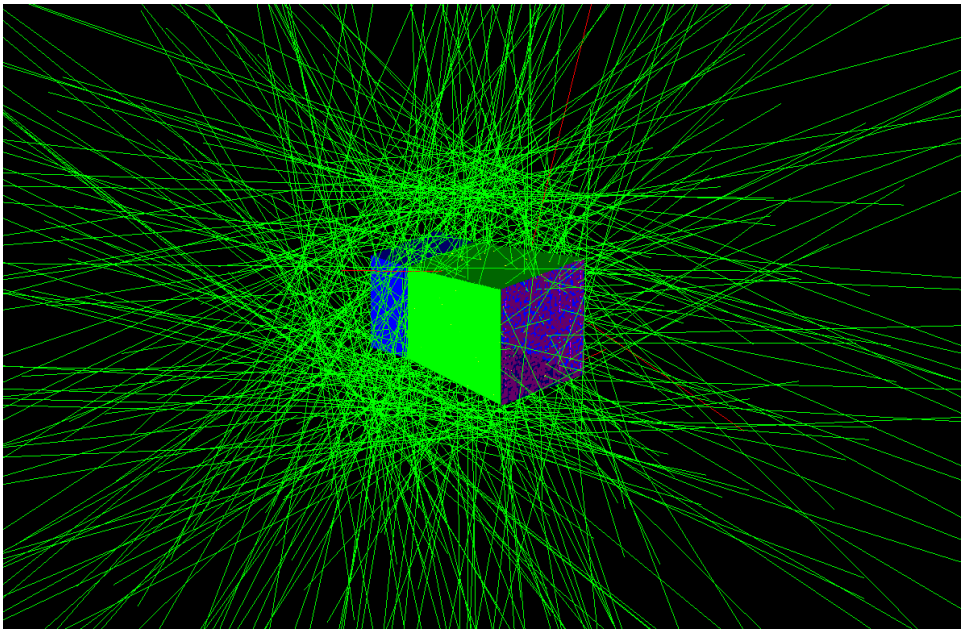

Figure 4.6: *Simulation of an isotropic source. The XGIS mass model (collimator shown in green, support in blue, coded mask in pink) is fully exposed to radiation (green lines).*

This derives from the integration over the 2π emission angle for a point on the spherical surface, biased with the cosine law:

$$\int_0^{2\pi} d\phi \int_0^{\pi/2} \cos\theta \sin\theta \, d\theta = \pi$$

and integrated over the source sphere surface $S = 4\pi R^2$. The restriction on the emission angle introduces the further factor $\sin^2\theta_{\max}$. Therefore, the simulation time (i.e. *exposure time*) that corresponds to N generated primary events is:

$$\tau = \frac{N}{\Phi \, 4\pi^2 R^2 \sin^2\theta_{\max}}$$

Simulations provide C_i counts in the energy bin i, (multiplied by the factor $(80/89)^2$ to account for the "dead pixels") both for X-mode and S-mode, thus the corresponding *measured flux*, in counts cm^{-2} s^{-1}, i.e., convolved with the detector response, has been computed as:

$$F_i = \frac{C_i}{\tau \, A_{\rm det}}$$

where $A_{\rm det}$ is the detector geometric area. Events detected in X-mode have been normalized using $A_{\rm det} = 1600$ cm^2, while events in S-mode have adopted $A_{\rm det} = 1296$ cm^2 [2].

[2]The first results from the number of SDD pixels per detector side (80) multiplied by the pixel size

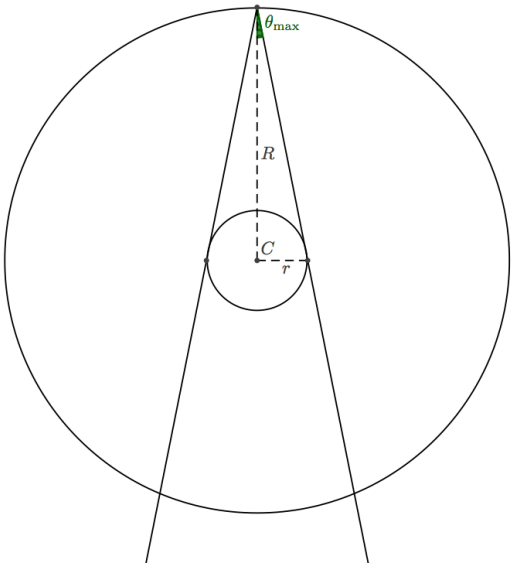

Figure 4.7: *Sketch of the source geometry used in the simulations for the background. Photons are emitted from a sphere of radius R; their isotropic emission is confined within an angle $\theta_{\max}$, which subtends a smaller sphere of radius r, that encloses the entire XGIS system.*

For the spherical source, a radius of $R = 500$ cm has been chosen, while $r = 70$ cm has been fixed to ensure that the whole XGIS system is irradiated. Therefore, a value of $\theta_{\max} = 7.97°$ has been computed. This choice is not restrictive, as the only constraint is to illuminate the entire detector.

Another aspect that needs to be considered in the normalization of the counts in X-mode and S-mode is the solid angle of origin for each source. It is important to first note that the solid angle, Ω_E, subtended by the Earth at an altitude h is given by (Campana et al., 2013):

$$\Omega_E = 2\pi \left(1 - \frac{1}{\frac{R_E}{h} + 1}\sqrt{1 + \frac{2R_E}{h}}\right) \tag{4.14}$$

with R_E the Earth radius; thus the accessible sky subtends a solid angle of $\Omega = 4\pi - \Omega_E$.

As shown in Fig. 4.8, a satellite like THESEUS, orbiting at an altitude of 600 km, has its FoV obstructed by the Earth by 30%. For this reason, the following correction factors have been considered: 0.7 for primary particle sources and the CXB, as they come from space; 0.3 for albedo radiation, which originates from the atmosphere; 1 for secondary particles, as their incoming direction is almost isotropic (AMS collaboration, 2000). In Tab. 4.1, for each simulated source, the number of primaries, the energy-integrated flux

(0.5 cm); the second considers the same number of scintillator bars, each with a size of 0.45 cm.

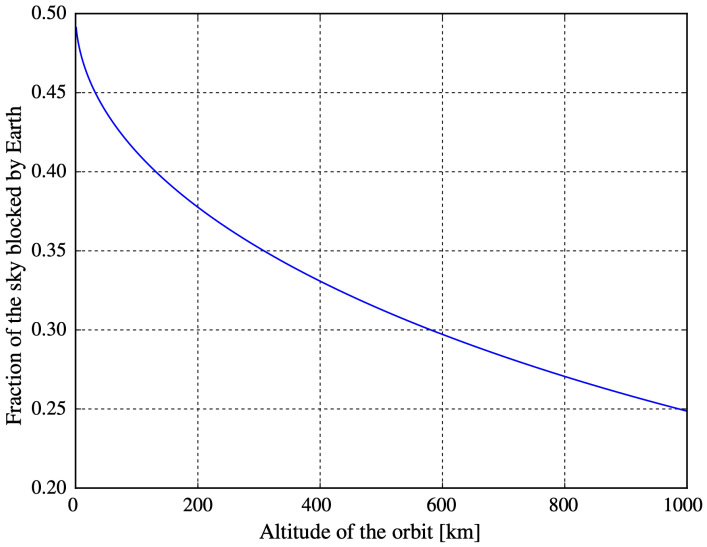

Figure 4.8: *The fraction of the sky obstructed by the Earth for a given orbit altitude h. For an altitude of 600 km, the Earth covers approximately 30% of the field of view (Campana et al., 2013).*

Φ (particles cm^{-2} s^{-1} sr^{-1}), the resulting exposure time and the fraction of solid angle are shown.

Source	**N**	**Φ (part/cm^2/s/sr)**	**Exposure (s)**	**Solid Angle**
primary Alpha	10^5	1.66×10^{-3}	317.5	0.7
primary Protons	10^5	1.14×10^{-2}	46.2	0.7
primary Electrons	10^5	7.15×10^{-5}	7371.7	0.7
primary Positrons	10^5	6.00×10^{-6}	87846.2	0.7
secondary Protons	10^6	9.55×10^{-3}	551.9	1
secondary Electrons	10^6	9.43×10^{-3}	558.9	1
secondary Positrons	10^6	3.11×10^{-2}	169.5	1
neutron Albedo	10^7	3.70×10^{-2}	1424.5	0.3
photon Albedo	10^7	6.69×10^{-1}	78.8	0.3
CXB	10^7	1.10×10^{1}	4.8	0.7

Table 4.1: *Inputs provided to the simulations for both the simple mass model and the upgraded one. The background sources are those described in the previous section. The number of primary events have been chosen to ensure a significant counting statistic (>10.000 counts). The integrated fluxes has been derived from the spectra discussed earlier, which were used to calculate the exposure time; finally the solid angle factor considered for each source.*

The contribution of each component to the XGIS background as a function of energy per unit area, is shown in Fig. 4.9 and Fig. 4.10, for the count rates in X-mode and S-mode, respectively. The results are presented for the simple mass model (top panels) and the upgraded one (bottom panels). In Tab. 4.2 and Tab. 4.3, the total count rates for the individual components and for the total background are reported, respectively, for the simple and upgraded mass models. Finally, in Fig. 4.11, the total count rates per unit area, as a function of energy, are shown.

For both mass models, the dominant contribution to the X-mode background, in the 2–30 keV energy range, comes from the CXB, which accounts for more than 99% of the total contribution. The contribution from other sources is negligible. The difference between the simple and upgraded mass models is noticeable at low energies: in fact, the count rate is nearly halved from 2800 ± 33 to 1630 ± 21 counts/s ($\sim$ 42% reduction) due to the additional components. As analyzed in Chap. 3, these components reduce the detection of low-energy photons, consequently decreasing the overall background contribution in this energy range.

For the S-mode background, in the 20–5000 keV energy range, the dominant contributions are due to the photon background up to several hundred of keV. For higher energies, the particle background becomes dominant. The difference in count rates between the two mass models is negligible ($\sim$ 1%) since, at high energies, the layers result transparent. The count rate reaches 1630 ± 25 counts/s. The S-mode background also shows noticeable fluorescence lines due to the tungsten in the mask and collimator (K_α and K_β lines at $\sim$59 keV and $\sim$67 keV, respectively), which could be used for calibration purposes.

The reported data are averaged over all possible satellite pointing directions. However, the Earth position relative to the XGIS pointing direction significantly impacts the resulting background, and its modulation will be the subject of further studies. For M5, it has been shown that, for S-mode, the maximum modulation is about 20%, a relatively small value due to the nearly isotropic sensitivity of the instrument. Whereas, for X-mode, the modulation can reach up to 90%, as a result of the restricted FoV (Campana et al., 2020).

Having an accurate estimate of the expected background rate at the current stage of the mission study is crucial, as it allows for further investigations and simulations regarding the population of short and long GRBs that XGIS can detect and localize. Moreover, it enables a more precise distinction between true detection triggers and false ones. In fact, considering that $SNR = N_{\mathrm{signal}}/\sqrt{\mathrm{N_{signal}} + \mathrm{N_{bkg}}}$, for M5, a conservative estimate was made such that triggers with $SNR > 7$ are considered to be originated from true GRBs. This estimate, based on studies of simulated GRB populations, allows not only to discard potential false triggers but also to avoid missing true, albeit faint, triggers (Mereghetti et al., 2020).

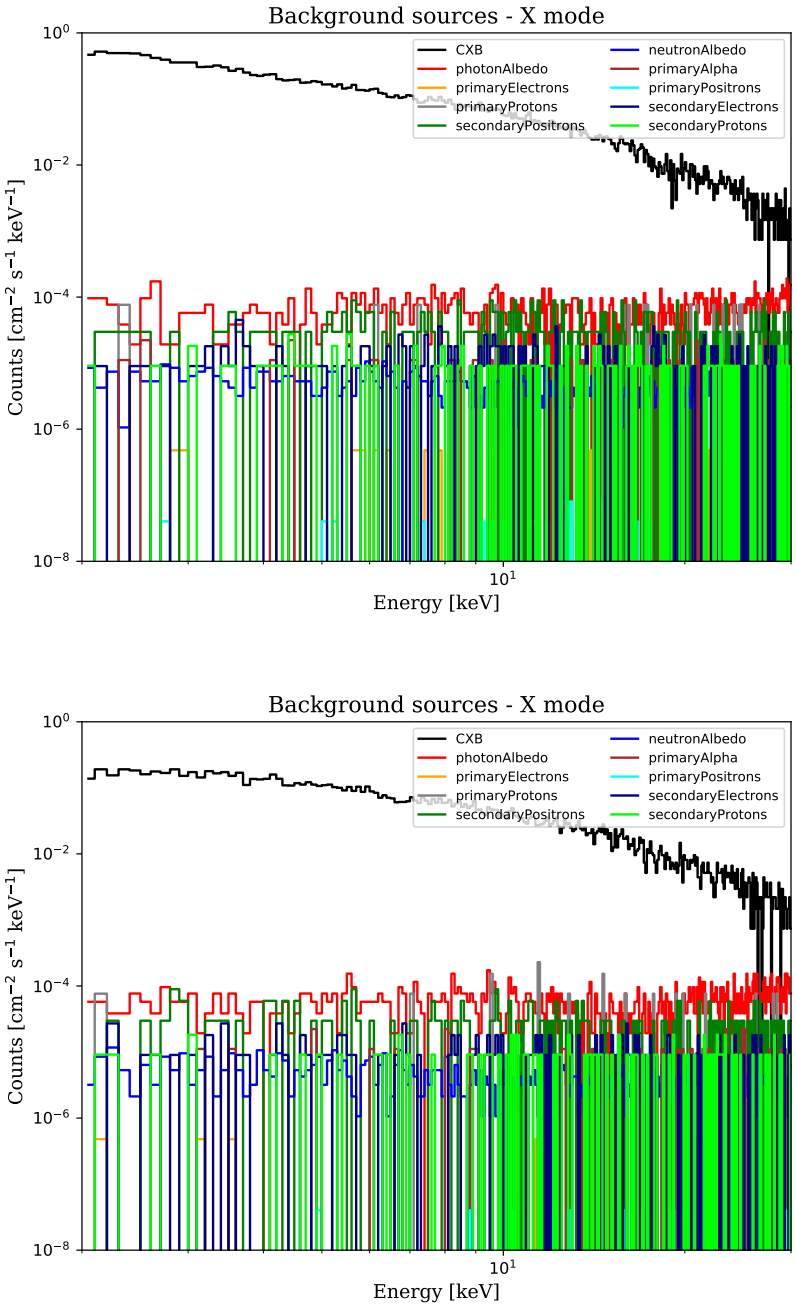

Figure 4.9: *Simulated source contributions to the X-mode background for the simple mass model (top panel) and the upgraded mass model (bottom panel), expressed in counts* $cm^{-2}\,s^{-1}\,keV^{-1}$. *The dominant contribution comes from CXB, while the others are negligible. Note that at lower energies, the count rate in the upgraded mass model is reduced by* $\sim 42\%$ *thanks to the presence of additional layers.*

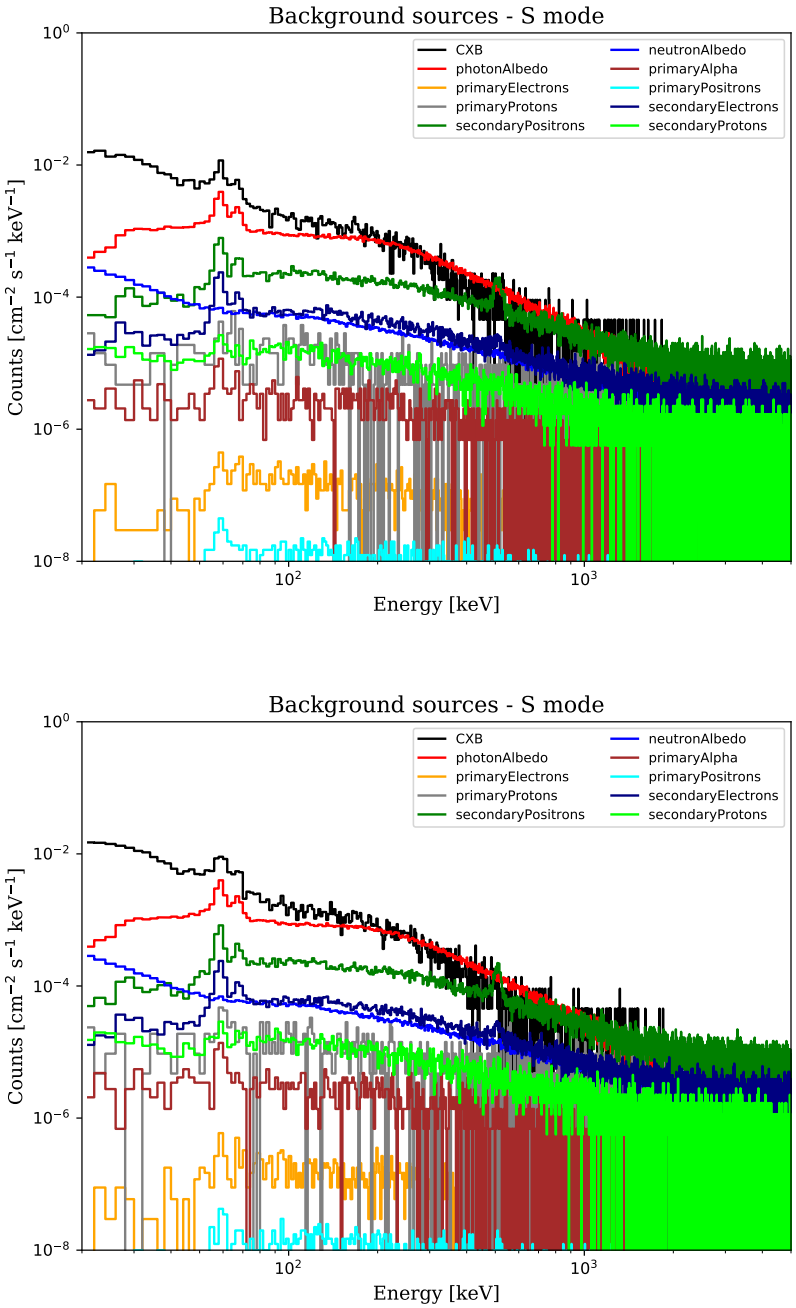

Figure 4.10: *Simulated source contributions to the S-mode background for the simple mass model (top panel) and the upgraded mass model (bottom panel), expressed in counts $cm^{-2}\,s^{-1}\,keV^{-1}$. Up to several hundred of keV, the dominant contribution is the photon background sources, while at higher energies, particle background prevails. No significant difference between the two mass model is present. Tungsten fluorescence lines are also present.*

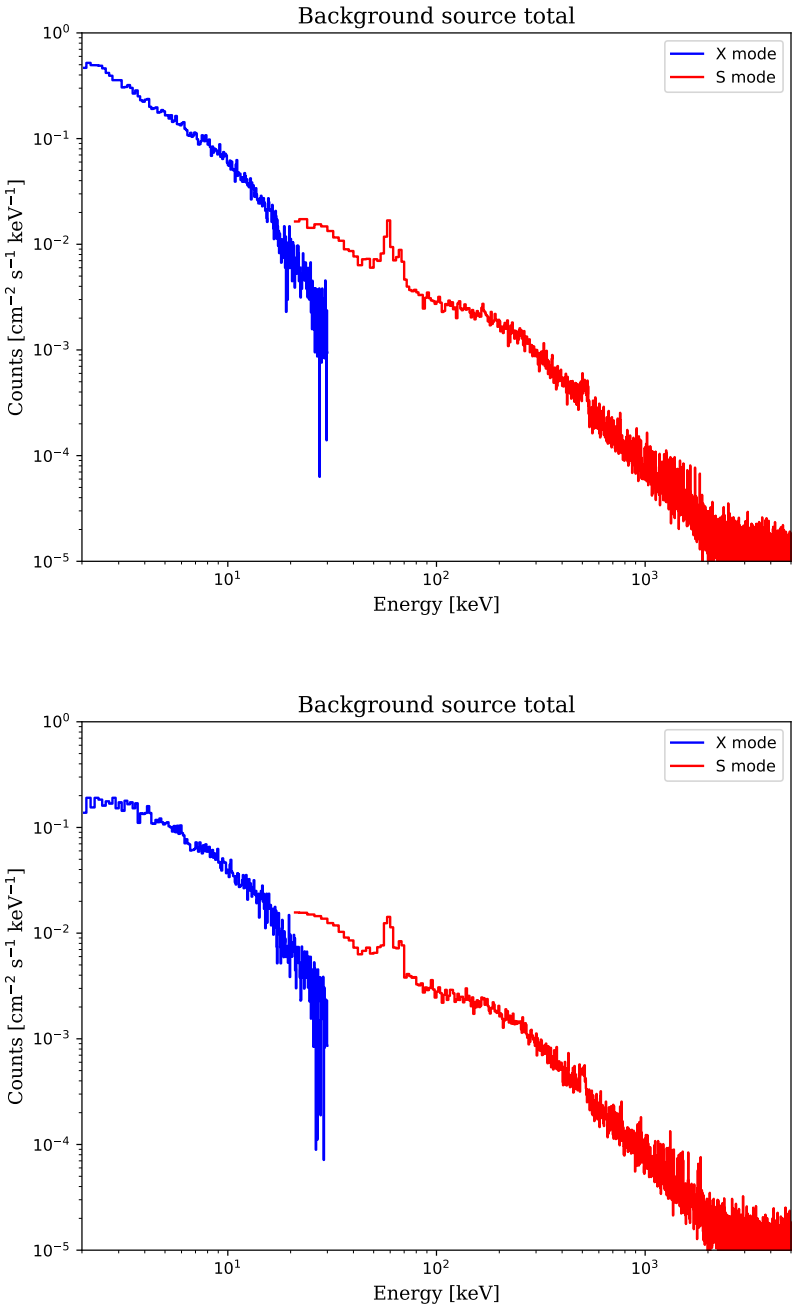

Figure 4.11: *Total background contributions in X-mode and S-mode for the simple mass model (top panel) and upgraded mass model (bottom panel), expressed in counts $cm^{-2}\,s^{-1}\,keV^{-1}$. At lower energies, the shielding effect of the protecting layers reduces the counts, while at higher energies, tungsten fluorescence lines are present.*

Table 4.2: *Total background count rate in X-mode and S-mode for the simple mass model. X-mode rate has been computed in the range within 2–30 keV, while S-mode rate in the range 20–5000 keV. The percentages refer to the maximum value reported for X-mode and S-mode. The statistical error is also reported.*

Source	**X-mode (s^{-1})**	**S-mode (s^{-1})**	**X-mode (%)**	**S-mode (%)**
CXB	2.80×10^{3}	9.18×10^{2}	99.82%	56.33%
photon Albedo	2.99×10^{0}	4.27×10^{2}	0.11%	26.20%
primary Electrons	1.76×10^{-3}	1.86×10^{-1}	0.00%	0.01%
primary Protons	1.96×10^{-1}	1.46×10^{1}	0.01%	0.90%
secondary Positrons	1.04×10^{0}	1.71×10^{2}	0.04%	10.50%
neutron Albedo	2.02×10^{-1}	3.90×10^{1}	0.01%	2.40%
primary Alpha	9.80×10^{-2}	2.82×10^{0}	0.00%	0.17%
primary Positrons	1.67×10^{-4}	1.58×10^{-2}	0.00%	0.00%
secondary Electrons	3.34×10^{-1}	4.51×10^{1}	0.01%	2.77%
secondary Protons	2.03×10^{-1}	1.18×10^{1}	0.01%	0.72%
Total X mode	2800 ± 33		100%	
Total S mode		1630 ± 21		100%

Table 4.3: *Total background count rate in X-mode and S-mode for the upgraded mass model. X-mode rate has been computed in the range within 2–30 keV, while S-mode rate in the range 20–5000 keV. The percentages refer to the maximum value reported for X-mode and S-mode. The statistical error is also reported.*

Source	**X-mode (s^{-1})**	**S-mode (s^{-1})**	**X-mode (%)**	**S-mode (%)**
CXB	1.63×10^{3}	9.02×10^{2}	99.74%	56.04%
photon Albedo	2.69×10^{0}	4.24×10^{2}	0.16%	26.35%
primary Electrons	0.00×10^{-4}	0.18×10^{-1}	0.00%	0.01%
primary Protons	0.22×10^{-1}	1.47×10^{1}	0.01%	0.90%
secondary Positrons	0.69×10^{-1}	1.70×10^{2}	0.04%	10.59%
neutron Albedo	0.20×10^{-1}	3.91×10^{1}	0.01%	2.43%
primary Alpha	0.06×10^{-2}	2.65×10^{0}	0.00%	0.16%
primary Positrons	0.00×10^{-4}	0.02×10^{-2}	0.00%	0.00%
secondary Electrons	0.25×10^{-1}	4.50×10^{1}	0.02%	2.79%
secondary Protons	0.14×10^{-1}	1.16×10^{1}	0.01%	0.72%
Total X mode	1630 ± 25		100%	
Total S mode		1610 ± 21		100%

4.3 Radiation effects and mitigation strategies

In the space environment, the interaction of high-energy particles can damage any X-ray detector. For instance, solid-state detectors are susceptible to the so-called nonionizing energy loss (NIEL), in which the transfer of energy from an incoming particle can damage the crystalline lattice of a semiconductor detector, increasing the dark current over time and degrading its performance.

Charged particles can interact with the satellite leaving in their wake an ionization streak, i.e., a continuous ionization of the material along their path, that, however, can be detected by the instrument. Another process that generates charged particles is the production of secondary showers by the electromagnetic and hadronic interactions of a high-energy primary proton with the instrument or the spacecraft structures. Moreover, high-energy protons encountered by the spacecraft along its orbit can induce radioactivation of the various spacecraft and detector materials: the net result is the creation of various types of unstable isotopes, which can then decay and ultimately perform as sources of unwanted γ-rays and ionizing particles, thus contributing to the background.

The background influences the instrument performance on multiple levels. It introduces rapid variations such as sudden increases due to flares, as well as gradual shifts related to the satellite orbit and orientation, affecting timing measurements. In the spectral domain, additional continuous signals and distinct emission lines are present, for example due to fluorescence in the detector materials. In imaging, these effects can lead to localized issues, such as unusually bright pixels and non-uniform detector responses.

These effects impose strict requirements on the design of space experiments, influencing factors such as the detector operating temperature and expected lifetime.

Estimating the level of onboard background for an X-ray space experiment is a mandatory feature of the instrument design phase and, in order to minimize it, several strategies can be employed (Campana, 2022).

To suppress the background caused by high-energy photons, detectors can be shielded using appropriate thicknesses of high-Z (high-density) materials. In the case of XGIS, the primary shielding is provided by the tungsten and aluminum layers that form the collimator and the detector supports. However, these shields can still generate a significant amount of secondary radiation, for example, due to fluorescence (as highlighted in the figures of the previous section).

A more advanced technique, which also helps reduce the mass, involves using graded-Z shielding (Fig. 4.12). This consists of a stack of materials with progressively lower atomic numbers. The layer with the highest Z is capable of scattering and absorbing protons, electrons, and gamma rays. Each following layer absorbs the X-ray fluorescence generated by photon interactions in the previous material, gradually reducing the energy to an acceptable level. A similar system could be introduced in the XGIS design to reduce the impact of fluorescence lines, but the trade-off with the additional mass and

complexity burden has to be carefully evaluated[3].

Another method to reduce the impact of charged particles on the instrumental background is the use of an active anticoincidence system. This involves surrounding the instrument with a fast, particle-sensitive detector. When the anticoincidence detector is triggered, it generates a veto signal, which allows for the rejection of any event that is caused by the same particle in the detector of interest (Fig. 4.13). This technique "isolate" the true events of interest by effectively filtering out background interference from charged particles. In the case of XGIS, this could be achieved by exploiting the most external layer of scintillator bars.

Another effective suppression method for particle-induced events can be achieved through an onboard filter, implemented either in hardware or software, that identifies and rejects such events. Particles incident on the XGIS detector leave ionization streaks that intersect multiple crystals simultaneously, and these can be effectively recognized thanks to the fine segmentation of the detection plane, which consists of 6400 individual pixels. Simulations show that a "topological" filter, which considers both the occurrence of an energy deposit above a few MeV in a single crystal (event saturation) and the number of simultaneously triggering crystals (event multiplicity), can achieve a rejection efficiency as high as 90%, depending on the type and energy of the incoming particle (Campana et al., 2020).

[3]THESEUS Report: XGIS Instrument Performance Budget.

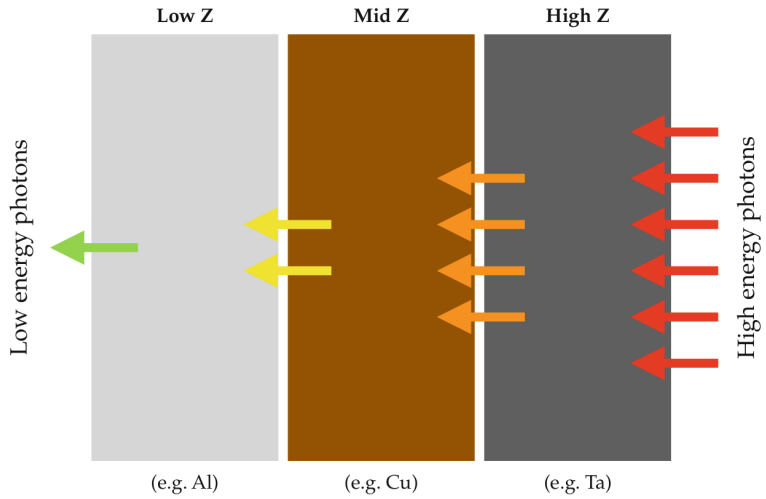

Figure 4.12: *Example of a graded-Z shield, in which layers of materials with different atomic number progressively filter the incoming photon flux, shifting the typical energies to lower values (Campana, 2022).*

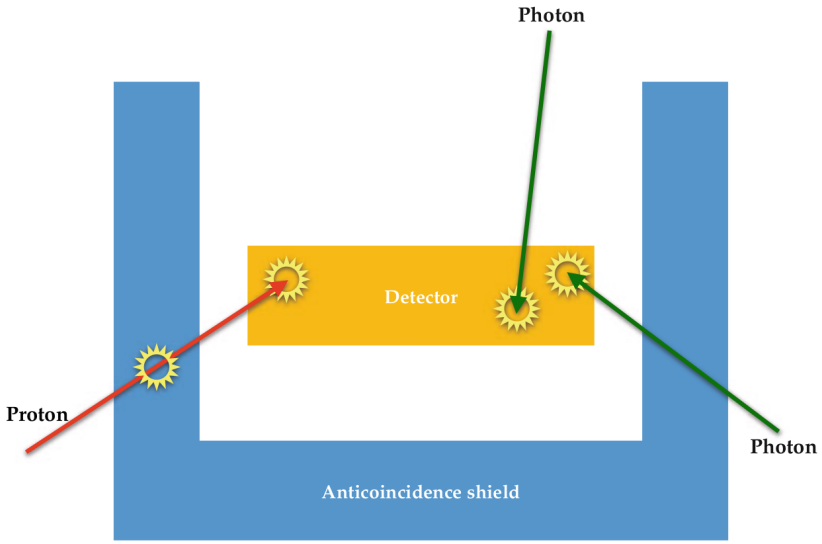

Figure 4.13: *Conceptual example of an active anticoincidence. A charged particle will leave a signal on both the detector and on the external shield, while photons will interact only with the detector. A suitable control electronics can then veto events occurring on both structures (Campana, 2022).*

4.4 Summary

The background noise sources in LEO affect the observations of any X-ray and gamma-ray detector.

The background count rates of the XGIS instrument have been evaluated through Monte Carlo simulations using the Geant4 software, considering both the simple and the upgraded mass models. As input, the sources described in Campana et al. (2013), previously used for studies conducted during the M5 phase, have been employed.

The simulations show a 42% reduction in background counts in X-mode (2–30 keV) between the two mass models, decreasing from 2800 ± 33 counts/s to 1630 ± 21 counts/s. This reduction is due to the protective layers in the upgraded mass model, which limit the passage of photons and particles with energies below 10 keV. The dominant component is found to be the Cosmic X-ray Background.

The background in S-mode (20–5000 keV) does not show significant differences between the two mass models and remains at approximately 1610 ± 21 counts/s, since the implemented protective layers affect only low energies. In this case, photon background dominates up to a few hundred keV, while at higher energies, particle background becomes the main contributor to the noise.

Upcoming improvements will take into account the activation of materials caused by trapped particles within the geomagnetic field lines. Moreover, a systematic study of strategies for rejecting spurious events, as well as a more detailed analysis of background contributions as a function of the XGIS pointing direction relative to the Earth, will be conducted. Additionally, a better mass model (CAD model) for the simulations will be exploited, provided by the University of Valencia working group responsible for the XGIS coded mask system.

The background count rate obtained is useful for upcoming scientific simulations of the XGIS performance and actively contributes to the current study phase of the entire M7 THESEUS mission.

Chapter 5

Conclusions and future perspectives

Gamma-Ray Bursts are the most energetic transient phenomena ever observed in the universe, capable of outshining any other source in the γ-ray band. Their extreme luminosity and connection to the final stages of stellar evolution make them essential tools for investigating the Early Universe and Multi-Messenger Astrophysics. In particular, high-redshift GRBs can provide crucial insights into the first stars (Population III) and the cosmic reionization process, while GRBs detected across a wide redshift range contribute to understanding star formation history and the evolution of cosmic metallicity.

The scientific importance of GRBs has led to the development of advanced space missions such as THESEUS, which is currently in Phase A (in the framework of the ESA Cosmic Vision M7 launch opportunity, after a previous study carried on in 2018–21 for the M5 slot) until the downselection of the mission, that will occur in 2026. Its payload includes two wide-field high-energy monitors and an infrared telescope, combined with rapid slewing capabilities, enabling the detection and localization of GRBs up to high redshifts. THESEUS will play a key role in triggering alerts for future ground-based and space-based observatories.

My thesis focuses on the performance evaluation of XGIS, the wide-field monitor onboard THESEUS, designed to perform imaging in the 2–150 keV range and spectroscopy up to 5–10 MeV. The detector employs an innovative design, combining Silicon Drift Detectors with CsI(Tl) scintillating bars, resulting in a compact architecture capable of covering a broad energy range.

The sensitivity of XGIS, crucial for detecting weak GRB signals, depends on factors such as effective area, instrumental response and background noise. These aspects have been analyzed through Monte Carlo simulations using the Geant4 toolkit, a standard tool for evaluating high-energy instruments. Compared to previous studies conducted for M5, the simulations in this work benefited from a more detailed mass model of XGIS, allowing for a more precise assessment of its design and performance.

Monte Carlo simulations were conducted to evaluate the effective area and instrument response in both X-mode (2–30 keV) and S-mode (20–5000 keV). The analysis compared

the simplified mass model with a random coded mask pattern to an improved model incorporating additional protective layers.

- In X-mode, the simple model yielded an effective area of ~ 800 cm^2, consistent with the 50% open fraction of the mask. The upgraded model showed a reduction in effective area (< 600 cm^2), due to the added shielding materials (MLI, polypropylene, PCB). In both cases the instrument response is essentially diagonal.

- In S-mode, no significant differences were observed between the two models. The effective area peaks at $\sim$1200 cm^2 around 300 keV, as the protective layers, transparent in this range, mainly affect low-energy photons. In both cases the instrument response is diagonal, with a low energy tail.

The effective area was confirmed to meet mission requirements. Future improvements will include finer sampling of energy, zenith, and azimuthal angles, as well as an increased number of simulated primary events. Additionally, an updated CAD-based mass model provided by the University of Valencia working group will be incorporated.

Background noise sources in Low Earth Orbit significantly impact X-ray and γ-ray observations. The background count rate for XGIS was evaluated using Monte Carlo simulations based on established models from previous studies.

- In X-mode, the improved mass model resulted in a significant reduction in background counts (from 2800 ± 33 to 1630 ± 21 counts/s), mainly due to the added protective layers. The dominant background component in this range is the Cosmic X-ray Background.

- In S-mode, background levels remained unchanged (1610 ± 21 counts/s) as high-energy photons and particles are less affected by shielding. Photon background dominates up to a few hundred keV, while at higher energies particle background become the primary source of noise.

Future work will refine background estimations by considering material activation effects due to trapped particles, optimizing event rejection strategies, and analyzing background contributions as a function of the instrument pointing direction relative to the Earth. The updated CAD-based mass model will also be implemented for more accurate simulations, allowing to evaluate also the performance of different, more efficient scintillator crystals such as GAGG:Ce (Cerium-doped Gadolinium Aluminum Gallium Garnet).

In subsequent phases of the THESEUS study, further design optimizations will be explored, including improvements to the coded mask pattern, mask element size and thickness, and mask support structures. Simulations will also investigate the possibility

of reducing background noise by exploiting the coarse 3D event reconstruction capabilities of XGIS, allowed by the dual readout of the scintillation light at both pixel ends, which could help discriminate spurious events originating from the bottom side of the scintillators. These optimizations will contribute to refining the instrument design trade-offs and enhancing its overall performance.

The results of this study provide valuable inputs for upcoming scientific simulations of XGIS performance and actively support the ongoing Phase A study of the M7 THESEUS mission (see Fig.5.1). For example, the analysis of the effective area, response, and background will be used to evaluate the overall flux sensitivity of the instrument[1]. Furthermore, the output of the simulations will be useful for studying and optimizing data transfer from the detector/module level to the data handling unit.[2]

The results presented in this thesis have also contributed to updating the official performance documents provided to ESA, ensuring that XGIS meets the mission scientific and technical objectives.

[1]According to the THESEUS/M7 Science Requirements Document, the current values for the sensitivity requirement are of 1.8×10^{-11} over the 0.3–5 keV energy band in 1500 seconds, of 1×10^{-10} over the 0.3–5 keV energy band in 100 seconds, of 10^{-8} over the 2–30 keV energy band in 1 second, of 3×10^{-8} over the 30–150 keV energy band in 1 second, and of 2.7×10^{-7} over the 150 keV–1 MeV energy band in 1 second at 3σ, in cgs units.

[2]In particular, this topic is currently actively under evaluation in the XGIS collaboration as a part of the Phase A study (I'm grateful to P. Calabretto and G. Mattioli for useful discussions).

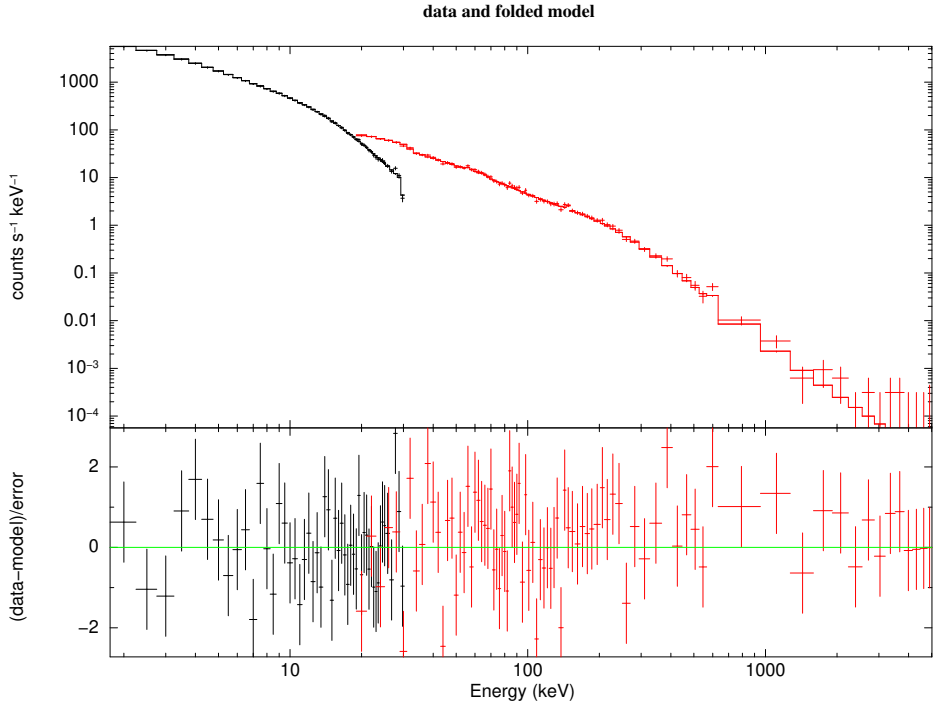

Figure 5.1: *Simulation, using the response matrices obtained in this work, of a very bright GRB (total 50–300 keV fluence of ∼10 photons cm^{-2}) as observed by XGIS. The black curve is X-mode, the red curve is S-mode. The spectrum is modeled as a Band function (Band et al., 1993) with parameters $\alpha = -2$, $\beta = -3$, and a break energy of 300 keV.*

Appendix A

Listing of the `main()` function

Here is the `main()` function I developed for the Geant4 simulations. This function calls several C++ scripts that make up the simulation, including those that define the construction of the mass model, the scripts that define the simulated physical processes, and those related to user actions, which include the input source and the output data to be saved.

The Python pipeline is used to invoke the `main()` function an arbitrary number of times, enabling consecutive simulations to be executed in sequence.

```
#include "G4MTRunManager.hh"
#include "G4RunManager.hh"
#include "G4VisExecutive.hh"
#include "G4UImanager.hh"
#include "G4UIExecutive.hh"
#include "G4UIterminal.hh"
#include "G4UItcsh.hh"
#include "DetectorConstruction.hh"
#include "UserActionInitialization.hh"
#include "PhysicsList.hh"
#include "G4PhysListFactory.hh"
#include "G4VUserPhysicsList.hh"
#include "PrimaryGeneratorAction.hh"
#include "UserRunAction.hh"
#include "UserEventAction.hh"
#include "G4UImessenger.hh"
#include "G4AnalysisManager.hh"

int main(int argc, char **argv)
{
    //    G4Random::setTheEngine(new CLHEP::RanecuEngine);
    //    G4Random::setTheSeed(time(0));
    // Detect interactive mode (if no arguments) and define UI session
    G4UIExecutive* ui = 0;
    if (argc == 1)
```

```
26      {
27          ui = new G4UIExecutive(argc, argv);
28      }
29      // Construct the run manager
30  #ifdef G4MULTITHREADED
31      G4MTRunManager * runManager = new G4MTRunManager;
32          runManager->SetNumberOfThreads(4);
33  #else
34      G4RunManager * runManager = new G4RunManager;
35  #endif
36      //runManager->SetVerboseLevel(2);
37      // Set mandatory initialization classes
38      runManager->SetUserInitialization(new DetectorConstruction());
39      runManager->SetUserInitialization(new PhysicsList());
40      // User action initialization
41      runManager->SetUserInitialization(new UserActionInitialization());
42      // Initialize G4 kernel
43      runManager->Initialize();
44      G4AnalysisManager* analysisManager = G4AnalysisManager::Instance();
45
46      // Visualization manager construction
47      auto visManager = new G4VisExecutive;
48      // G4VisExecutive can take a verbosity argument - see /vis/verbose
            guidance.
49      // G4VisManager* visManager = new G4VisExecutive("Quiet");
50      visManager->Initialize();
51
52      // Get the pointer to the User Interface manager
53      auto uiManager = G4UImanager::GetUIpointer();
54      // Activation of atomic EM de-excitation processes
55      uiManager->ApplyCommand("/run/initialize");
56      uiManager->ApplyCommand("/process/em/deexcitation␣World␣true␣true␣
            true");
57      uiManager->ApplyCommand("/process/em/fluo␣true");
58      uiManager->ApplyCommand("/process/em/auger␣true");
59      uiManager->ApplyCommand("/run/physicsModified");
60
61      if (!ui) // Batch mode
62      {
63          // execute an argument macro file if exist
64          G4String command = "/control/execute␣";
65          G4String fileName = argv[1];
66          if(argc==3)
67          {
68              // If there are two batch files (e.g. a General Particle
                    Source macro)
69              // load this first
70              G4String fileGPS = argv[2];
71              uiManager->ApplyCommand(command+fileGPS);
```

```
72              G4cout << "GPS␣macro␣file␣executed:␣" << fileGPS << G4endl;
73          }
74          else
75          {
76              // Default GPS
77              uiManager->ApplyCommand("/gps/particle␣gamma");
78              uiManager->ApplyCommand("/gps/energy␣100␣keV");
79              uiManager->ApplyCommand("/gps/position␣␣␣␣␣0.0␣␣0.0␣+50.0␣
                    cm");
80              uiManager->ApplyCommand("/gps/direction␣␣␣␣0.0␣␣0.0␣-1.0");
81              uiManager->ApplyCommand("/gps/polarization␣1.0␣␣0.0␣␣0.0");
82          }
83          // Execute batch file
84          uiManager->ApplyCommand(command+fileName);
85          G4cout << "Batch␣file␣executed:␣" << fileName << G4endl;
86      }
87      else // GUI or interactive mode
88      {
89          uiManager->ApplyCommand("/control/execute␣init_vis.mac");
90          if (ui->IsGUI()) {
91              uiManager->ApplyCommand("/control/execute␣visGUI.mac");
92          }
93          // start interactive session
94          ui->SessionStart();
95          delete ui;
96      }
97      // Job termination
98      delete visManager;
99      delete runManager;
100     return 0;
101 }
```

Listing A.1: The `main()` function implemented in the Geant4 application used for all simulations.

Below, I provide the list of C++ source code files used for the simulation. Their corresponding headers files are omitted. The `CMakeLists.txt` file is used to build the source code and create the executable `xgis_M7`. The `mask.dat` and `detector_params.inp` files are input parameters for the mass model, which are read by `ConfigFile.cc` to allow easy modifications. The `mask.dat` file contains the random mask pattern provided to the mass model, which can also be easily replaced. The `geometry.gdml` file contains all the information related to the detector.

- `DetectorConstruction.cc`
- `ModuleParameterisation.cc`
- `PrimaryGeneratorAction.cc`

- SensitiveDetector.cc
- UserRunAction.cc
- DetectorHit.cc
- PCBParameterisation.cc
- SDDDetectorHit.cc
- UserActionInitialization.cc
- UserRun.cc
- ConfigFile.cc
- MaskParameterisation.cc
- PhysicsList.cc
- SDDSensitiveDetector.cc
- UserEventAction.cc
- CMakeLists.txt
- geometry.gdml
- xgis_M7.cc
- detector_params.inp
- mask.dat
- xgis_M7

The Geant4 application was initially tested with simple simulations on my personal computer. Subsequently, the simulations exploited the computational power of the INAF/OAS computing cluster. The deployment of the code on the cluster was achieved by means of a Docker container, which included all the necessary dependencies to run the application.

Appendix B

Coded mask technique

Unlike telescopes based on the reflection or refraction of incoming radiation, the image obtained by the detector of a coded mask instrument is quite different from the actual image of the observed sky. This is because the signal collected by the detector does not directly represent the observed sources but rather the shadow pattern produced by them after being encoded by the mask (Fig. B.1). To obtain an image of the sky, it is therefore necessary to properly decode this signal (Fig. B.2).

In order to decode the signal, let's consider a detector composed of a grid of pixels (x, y), where the signal D in each pixel is given by

$$D(x, y) = A(x, y) * S(x, y) + B(x, y) \tag{B.1}$$

where A is the matrix describing the mask pattern, S is the observed sky image, B represents the background noise, and $*$ denotes the correlation operator. If the chosen mask pattern is appropriate, it is possible to reconstruct an image of the observed sky sources by performing a convolution between the detector image and a specific decoding matrix, which depends on the selected pattern:

$$\hat{S}(x, y) = G(x, y) * D(x, y) \sim S(x, y) \tag{B.2}$$

where $\hat{S}$ is the reconstructed sky matrix and G is the decoding matrix defined such that Point Spread Function PSF=$G * A$ is δ-form. If the matrix A were invertible, then $G = A^{-1}$ would satisfy the previous condition, but this solution could lead to background noise amplification issues if some elements of G are large. To avoid this, it is possible to define G as:

$$G_{jk} = \begin{cases} 1, & \text{if } A_{jk} = 1 \\ \tau/(\tau - 1), & \text{if } A_{jk} = 0 \end{cases}$$

Where τ is the open mask fraction, i.e., the ratio between the number of open mask elements and the total number of elements. The matrix thus defined approximates

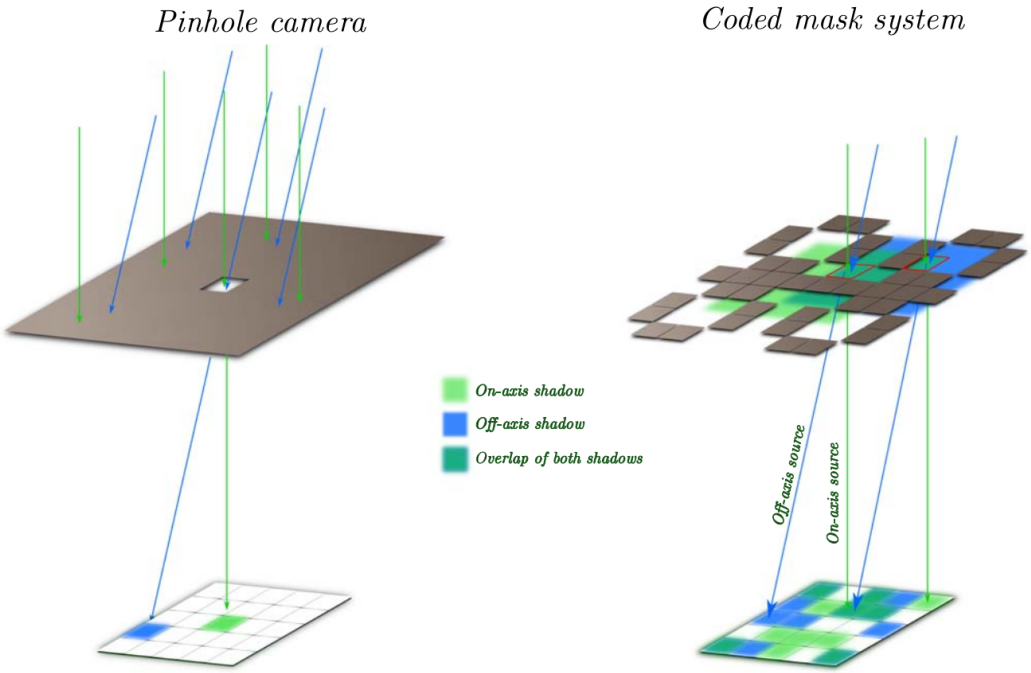

Figure B.1: *Left: a pinhole camera or a single-open-cell coded-mask imager. The detector plane registers an image of the source field with relatively low significance peaks, since the detecting area corresponds to only one mask element. Right: a coded-mask imager. The detector plane registers an overlapping set of shifted shadowgrams of the mask pattern, each set associated with one point source. The peaks in the reconstructed image have much higher significance, since the number of detected source photons is multiplied by the number of open cells of the basic mask pattern (Braga, 2019).*

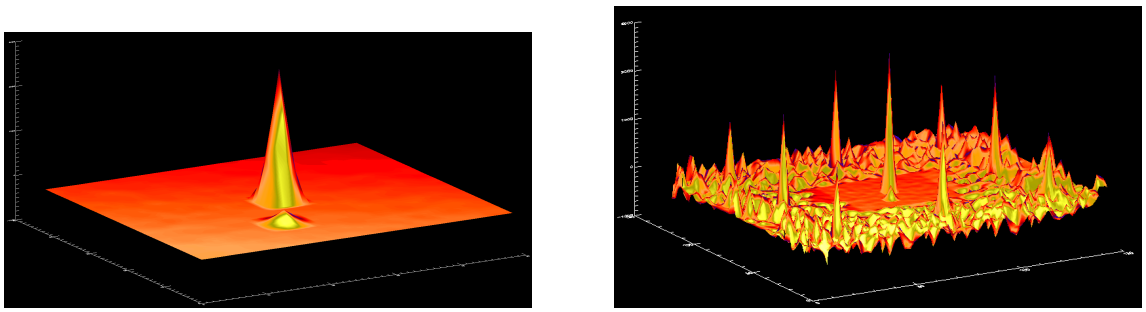

Figure B.2: *Comparison between simulated deconvolved sky images for a source within the FCFOV (left) and within the PCFOV (right). Many more artifacts and secondary lobes are produced during the deconvolution of off-axis sources, while on-axis sources generate flat side-lobe peaks. (Goldwurm and Gros, 2024).*

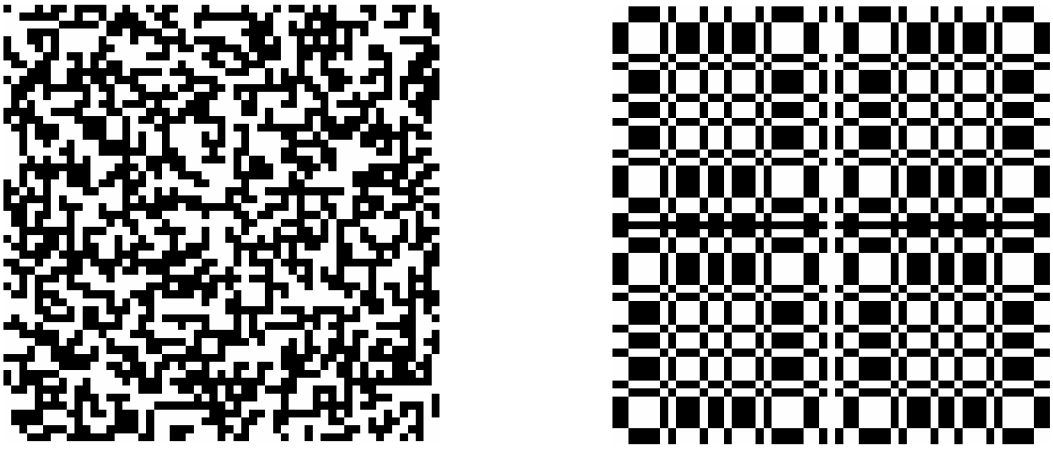

Figure B.3: *Self-supporting mask pattern (left). MURA pattern (right) (Credits: Edoardo Arrigoni, INAF-IASF Milano).*

a solution to the given condition and does not cause uncontrolled background noise amplification, as it assumes limited values for plausible τ values ($\sim$0.3–0.5)

During the design phase of a detector, it is necessary to make an optimal choice of the mask pattern used. In fact, to reconstruct an image of the sky from the data collected by the detector, it is essential that the shadow projected by the mask be unique for each direction from which the radiation originates. Therefore, the autocorrelation function (ACF) of the mask, which determines the PSF, must be δ-shaped.

The simplest pattern that satisfies this condition is one consisting of a single hole (this is the working principle of the so-called pinhole camera). However, in this configuration, sensitivity and localization accuracy are inversely proportional to each other, since the former depends on the area of the hole, while the latter depends on the inverse of its angular size. A proposed solution to this issue is to use a pattern consisting of multiple holes arranged in random positions. This improves sensitivity (which is proportional to the total area of the holes) without altering localization accuracy (which depends on the angular size of each individual hole).

The Fig. B.3 shows two types of patterns different from the random pattern used in the thesis work.

On the left, a Self-Supporting mask pattern (Giles, 1981) is shown, in which the closed elements of the mask are all adjacent. On the right, the MURA pattern (Modified Uniformly Redundant Array, Fenimore and Cannon 1978), which has not been chosen for XGIS since; although it deconvolves sources within FCFOV with less degradation, it worsens sources within PCFOV significantly, introducing artifacts and secondary structures. Therefore, since XGIS is designed to detect transient phenomena, it is expected that most of the observed sources will be off-axis.

Bibliography

Aartsen, M. G., Ackermann, M., Adams, J., Aguilar, J., Ahlers, M., Ahrens, M., Altmann, D., Andeen, K., Anderson, T., Ansseau, I., et al. (2017). The icecube neutrino observatory: instrumentation and online systems. *Journal of Instrumentation*, 12(03):P03012.

Abbott, B. P., Abbott, R., Abbott, T., Acernese, F., Ackley, K., Adams, C., Adams, T., Addesso, P., Adhikari, R., Adya, V., et al. (2017). Gravitational waves and gamma-rays from a binary neutron star merger: GW170817 and GRB 170817A. *The Astrophysical Journal Letters*, 848(2):L13.

Agostinelli, S., Allison, J., Amako, K. a., Apostolakis, J., Araujo, H., Arce, P., Asai, M., Axen, D., Banerjee, S., Barrand, G., et al. (2003). GEANT4 a simulation toolkit. *Nuclear instruments and methods in physics research section A: Accelerators, Spectrometers, Detectors and Associated Equipment*, 506(3):250–303.

Ajello, M., Greiner, J., Sato, G., Willis, D. R., Kanbach, G., Strong, A. W., Diehl, R., Hasinger, G., Gehrels, N., Markwardt, C. B., and Tueller, J. (2008). Cosmic X-Ray Background and Earth Albedo Spectra with Swift BAT. *The Astrophysical Journal*, 689(2):666–677.

Allison, J., Amako, K., Apostolakis, J., Araujo, H., Dubois, P. A., Asai, M., Barrand, G., Capra, R., Chauvie, S., Chytracek, R., et al. (2006). Geant4 developments and applications. *IEEE Transactions on nuclear science*, 53(1):270–278.

Allison, J., Amako, K., Apostolakis, J., Arce, P., Asai, M., Aso, T., Bagli, E., Bagulya, A., Banerjee, S., Barrand, G., et al. (2016). Recent developments in Geant4. *Nuclear instruments and methods in physics research section A: Accelerators, Spectrometers, Detectors and Associated Equipment*, 835:186–225.

Amaro-Seoane, P., Audley, H., Babak, S., Baker, J., Barausse, E., Bender, P., Berti, E., Binetruy, P., Born, M., Bortoluzzi, D., et al. (2017). Laser interferometer space antenna. *arXiv preprint arXiv:1702.00786*.

Amati, L. et al. (2018). The THESEUS space mission concept: science case, design and expected performances. *Advances in Space Research*, 62(1):191–244.

Amati, L. et al. (2021). The THESEUS space mission: science goals, requirements and mission concept. *Experimental Astronomy*, pages 1–36.

Amati, L., Frontera, F., Tavani, M., Antonelli, A., Costa, E., Feroci, M., Guidorzi, C., Heise, J., Masetti, N., Montanari, E., et al. (2002). Intrinsic spectra and energetics of bepposax gamma–ray bursts with known redshifts. *Astronomy & Astrophysics*, 390(1):81–89.

Amati, L., Labanti, C., Mereghetti, S., Frontera, F., Campana, R., Auricchio, N., Baldazzi, G., Bellutti, P., Bertuccio, G., Branchesi, M., et al. (2022). The X/Gamma-ray Imaging Spectrometer (XGIS) for THESEUS and other mission opportunities. In *Space Telescopes and Instrumentation 2022: Ultraviolet to Gamma Ray*, volume 12181, pages 551–563. SPIE.

AMS collaboration (2000). Protons in near earth orbit. *arXiv preprint hep-ex/0002049*.

Angel, J. (1979). Lobster eyes as X-ray telescopes. In *Space Optics Imaging X-Ray Optics Workshop*, volume 184, pages 84–85. SPIE.

Ascenzi, S., Oganesyan, G., Branchesi, M., and Ciolfi, R. (2021). Electromagnetic counterparts of compact binary mergers. *Journal of Plasma Physics*, 87(1):845870102.

Atwood, W., Abdo, A. A., Ackermann, M., Althouse, W., Anderson, B., Axelsson, M., Baldini, L., Ballet, J., Band, D., Barbiellini, G., et al. (2009). The large area telescope on the Fermi gamma-ray space telescope mission. *The Astrophysical Journal*, 697(2):1071.

Band, D., Matteson, J., Ford, L., Schaefer, B., Palmer, D., Teegarden, B., Cline, T., Briggs, M., Paciesas, W., Pendleton, G., et al. (1993). BATSE observations of gamma-ray burst spectra. I-Spectral diversity. *Astrophysical Journal, Part 1 (ISSN 0004-637X), vol. 413, no. 1, p. 281-292.*, 413:281–292.

Braga, J. (2019). Coded aperture imaging in high-energy astrophysics. *Publications of the Astronomical Society of the Pacific*, 132(1007):012001.

Brough, S., Collins, C., Demarco, R., Ferguson, H. C., Galaz, G., Holwerda, B., Martinez-Lombilla, C., Mihos, C., and Montes, M. (2020). The Vera Rubin Observatory Legacy Survey of space and time and the low surface brightness Universe. *arXiv preprint arXiv:2001.11067*.

Campana, R. (2022). In-orbit background for X-ray detectors. In *Handbook of X-ray and Gamma-ray Astrophysics*, pages 919–945. Springer.

Campana, R., Feroci, M., Del Monte, E., Mineo, T., Lund, N., and Fraser, G. W. (2013). Background simulations for the Large Area Detector onboard LOFT. *Experimental Astronomy*, 36:451–477.

Campana, R., Fuschino, F., Labanti, C., Mereghetti, S., Virgilli, E., Fioretti, V., Orlandini, M., Stephen, J. B., and Amati, L. (2020). The XGIS instrument on-board THESEUS: Monte Carlo simulations for response, background, and sensitivity. In *Space Telescopes and Instrumentation 2020: Ultraviolet to Gamma Ray*, volume 11444, pages 1245–1253. SPIE.

Caroli, E., Stephen, J., Di Cocco, G., Natalucci, L., and Spizzichino, A. (1987). Coded aperture imaging in X-and gamma-ray astronomy. *Space Science Reviews*, 45(3):349–403.

Castoldi, A. and Guazzoni, C. (2012). Sideward depletion: A novel detector family pushes the performance of the integrated front end to new heights. *IEEE Solid-State Circuits Magazine*, 4(3):46–54.

Cavallo, G. and Rees, M. (1978). A qualitative study of cosmic fireballs and γ-ray bursts. *Monthly Notices of the Royal Astronomical Society*, 183(3):359–365.

Christiansen, E. L., Arnold, J., Corsaro, B., Davis, A., Giovane, F., Hyde, J., Lear, D., Liou, J., Lyons, F., Prior, T., et al. (2009). Handbook for designing MMOD protection. *NASA Johnson Space Center, NASA/TM-2009-214785*.

Cordier, B., Götz, D., and Motch, C. (2018). The SVOM mission, a pathfinder for THESEUS. *arXiv preprint arXiv:1802.01681*.

Costa, E., Frontera, F., Heise, J., Feroci, M. a., In't Zand, J., Fiore, F., Cinti, M., Dal Fiume, D., Nicastro, L., Orlandini, M., et al. (1997). Discovery of an X-ray afterglow associated with the γ-ray burst of 28 February 1997. *Nature*, 387(6635):783–785.

Cruise, M., Guainazzi, M., Aird, J., Carrera, F. J., Costantini, E., Corrales, L., Dauser, T., Eckert, D., Gastaldello, F., Matsumoto, H., et al. (2024). The newathena mission concept in the context of the next decade of x-ray astronomy. *Nature Astronomy*, pages 1–9.

CTA Consortium (2010). Design concepts for the cherenkov telescope array. *arXiv preprint arXiv:1008.3703*.

Deininger, W. D., Peterson, C., Kalinowski, W., Bladt, J., Ly, T., Mitchell, S., Maddox, T., Osborne, D., Ruswick, S., Davis, K., et al. (2023). Imaging X-Ray Polarimetry Explorer (IXPE)-One Year On-Orbit. In *2023 IEEE Aerospace Conference*, pages 1–18. IEEE.

Dewdney, P. E., Hall, P. J., Schilizzi, R. T., and Lazio, T. J. L. (2009). The square kilometre array. *Proceedings of the IEEE*, 97(8):1482–1496.

ECSS (2000). Space environment. Technical report, ECSS-E-10-04A.

Elitzur, M. (2006). The obscuring torus in agn. *New Astronomy Reviews*, 50(9-10):728–731.

European Space Agency (ESA) (2021). THESEUS Assessment Study Report (Yellow Book). Technical Report ESA/SCI(2021)2, European Space Agency (ESA), Noordwijk, The Netherlands. Accessed: January 25, 2025.

Fenimore, E. E. and Cannon, T. M. (1978). Coded aperture imaging with uniformly redundant arrays. *Applied optics*, 17(3):337–347.

Frontera, F. (2024). A Short History of the First 50 Years: From the GRB Prompt Emission and Afterglow Discoveries to the Multimessenger Era. *Universe*, 10(6):260.

Fuschino, F., Campana, R., Labanti, C., Amati, L., Virgilli, E., Terenzi, L., Bellutti, P., Bertuccio, G., Borghi, G., Ficorella, F., et al. (2020). The XGIS instrument on-board THESEUS: the detection plane and on-board electronics. In *Space Telescopes and Instrumentation 2020: Ultraviolet to Gamma Ray*, volume 11444, pages 1263–1276. SPIE.

Gatti, E. and Rehak, P. (1984). Semiconductor drift chamber—An application of a novel charge transport scheme. *Nuclear Instruments and Methods in Physics Research*, 225(3):608–614.

Gehrels, N., Chincarini, G., Giommi, P., Mason, K., Nousek, J., Wells, A., White, N., Barthelmy, S., Burrows, D. N., Cominsky, L. R., et al. (2004). The Swift gamma-ray burst mission. *The Astrophysical Journal*, 611(2):1005.

Gehrels, N., Ramirez-Ruiz, E., and Fox, D. B. (2009). Gamma-ray bursts in the Swift era. *Annual Review of Astronomy and Astrophysics*, 47(1):567–617.

Ghail, R., Wilson, C., Widemann, T., Bruzzone, L., Dumoulin, C., Helbert, J., Herrick, R., Marcq, E., Mason, P., Rosenblatt, P., et al. (2017). EnVision: understanding why our most Earth-like neighbour is so different. *arXiv preprint arXiv:1703.09010*.

Giacconi, R., Gursky, H., Paolini, F. R., and Rossi, B. B. (1962). Evidence for x rays from sources outside the solar system. *Physical Review Letters*, 9(11):439.

Giles, A. (1981). Self-supporting perfect masks for 2-d infrared and x-ray imaging. *Applied Optics*, 20(17):3068–3072.

Gilmozzi, R. and Spyromilio, J. (2007). The european extremely large telescope (e-elt). *The Messenger*, 127(11):3.

Gleeson, L. J. and Axford, W. I. (1968). Solar Modulation of Galactic Cosmic Rays. *The Astrophysical Journal*, 154:1011.

Goldwurm, A. and Gros, A. (2024). Coded mask instruments for gamma-ray astronomy. In *Handbook of X-ray and Gamma-ray Astrophysics*, pages 1613–1669. Springer.

Götz, D., Basa, S., Pinsard, F., Martin, L., Arhancet, A., Bozzo, E., Cara, C., Sanz, I. E., Frugier, P.-A., Floriot, J., et al. (2020). The Infra-Red Telescope (IRT) on board the THESEUS mission. In *Space Telescopes and Instrumentation 2020: Ultraviolet to Gamma Ray*, volume 11444, pages 423–431. SPIE.

Götz, D., Paul, J., Basa, S., Wei, J., Zhang, S., Atteia, J.-L., Barret, D., Cordier, B., Claret, A., Deng, J., et al. (2009). SVOM: a new mission for Gamma-Ray Burst Studies. In *AIP conference proceedings*, volume 1133, pages 25–30. American Institute of Physics.

Gruber, D., Matteson, J., Peterson, L., and Jung, G. (1999). The spectrum of diffuse cosmic hard X-rays measured with HEAO 1. *The Astrophysical Journal*, 520(1):124.

Grün, E., Zook, H. A., Fechtig, H., and Giese, R. (1985). Collisional balance of the meteoritic complex. *Icarus*, 62(2):244–272.

H.E.S.S. Collab, Abdalla, H., Aharonian, F., Ait Benkhali, F., Angüner, E. O., Arcaro, C., Armand, C., Armstrong, T., Ashkar, H., Backes, et al. (2021). Revealing x-ray and gamma ray temporal and spectral similarities in the GRB 190829A afterglow. *Science*, 372(6546):1081–1085.

Holder, J., Atkins, R., Badran, H., Blaylock, G., Bradbury, S., Buckley, J., Byrum, K., Carter-Lewis, D., Celik, O., Chow, Y., et al. (2006). The first VERITAS telescope. *Astroparticle Physics*, 25(6):391–401.

Iyudin, A., Labanti, C., and Roberts, O. (2022). Scintillation detectors in gamma-ray astronomy. In *Handbook of X-ray and Gamma-ray Astrophysics*, pages 1–42. Springer.

Jiang, J. and Pasham, D. R. (2020). From raw data to scientific products: Images, light curves and spectra. In *Tutorial Guide to X-ray and Gamma-ray Astronomy: Data Reduction and Analysis*, pages 185–201. Springer.

Johns, M. (2006). The giant magellan telescope (gmt). In *Ground-based and Airborne Telescopes*, volume 6267, pages 762–776. SPIE.

Katz, U. F. (2006). Km3net: Towards a km3 mediterranean neutrino telescope. *Nuclear Instruments and Methods in Physics Research Section A: Accelerators, Spectrometers, Detectors and Associated Equipment*, 567(2):457–461.

Klebesadel, R. W., Strong, I. B., and Olson, R. A. (1973). Observations of gamma-ray bursts of cosmic origin. *Astrophysical Journal, vol. 182, p. L85*, 182:L85.

Knoll, G. F. (2010). *Radiation detection and measurement*. John Wiley & Sons.

Labanti, C., Amati, L., Frontera, F., Mereghetti, S., Gasent-Blesa, J. L., Tenzer, C., Orleanski, P., Kuvvetli, I., Campana, R., Fuschino, F., et al. (2020). The X/Gamma-ray Imaging Spectrometer (XGIS) on-board THESEUS: Design, main characteristics, and concept of operation. In *Space Telescopes and Instrumentation 2020: Ultraviolet to Gamma Ray*, volume 11444, pages 395–413. SPIE.

Longair, M. S. (2011). *High energy astrophysics*. Cambridge university press.

Lorenz, E. (1996). The MAGIC telescope project for gamma ray astronomy in the 15 to 300 GeV energy range. *Nuclear Physics B-Proceedings Supplements*, 48(1-3):494–496.

Macchia, M. C. (2015). *The design of a compact and portable system for combined XRF and Raman measurements*. PhD Thesis, University of Salento.

Marcucci, M. F., Retinò, A., Dunlop, M., Forsyth, C., Khotyaintsev, Y., Le Contel, O., Mann, I., Nakamura, R., Palmroth, M., Plaschke, F., et al. (2023). Plasma Observatory ESA M7 candidate mission: unveiling plasma energization and energy transport through multiscale observations. In *EGU General Assembly Conference Abstracts*, pages EGU–9043.

Margutti, R., Zaninoni, E., Bernardini, M., Chincarini, G., Pasotti, F., Guidorzi, C., Angelini, L., Burrows, D., Capalbi, M., Evans, P. A., et al. (2013). The prompt-afterglow connection in gamma-ray bursts: a comprehensive statistical analysis of Swift X-ray light curves. *Monthly Notices of the Royal Astronomical Society*, 428(1):729–742.

Marirrodriga, C. G., Pacros, A., Strandmoe, S., Arcioni, M., Arts, A., Ashcroft, C., Ayache, L., Bonnefous, Y., Brahimi, N., Cipriani, F., et al. (2021). Solar Orbiter: Mission and spacecraft design. *Astronomy & Astrophysics*, 646:A121.

Marisaldi, M., Labanti, C., Soltau, H., Fiorini, C., Longoni, A., and Perotti, F. (2005). X- and gamma-ray detection with a silicon drift detector coupled to a CsI (Tl) scintillator operated with pulse shape discrimination technique. *IEEE Transactions on Nuclear Science*, 52(5):1842–1848.

Mele, F., Dedolli, I., Gandola, M., Grassi, M., Malcovati, P., Amati, L., Bellutti, P., Borghi, G., Campana, R., Demenev, E., et al. (2021). ORION, a multichip readout electronics for satellite wide energy range X-/γ-ray imaging spectroscopy: Design and characterization of the analog section. *IEEE Transactions on Nuclear Science*, 68(12):2801–2809.

Mereghetti, S., Balman, S., Caballero-Garcia, M., Del Santo, M., Doroshenko, V., Erkut, M., Hanlon, L., Hoeflich, P., Markowitz, A., Osborne, J., et al. (2021). Time domain astronomy with the THESEUS satellite. *Experimental Astronomy*, pages 1–98.

Mereghetti, S., Ghirlanda, G., Salvaterra, R., Campana, R., Labanti, C., Connell, P. H., Farinelli, R., Frontera, F., Fuschino, F., Gasent-Blesa, J. L., et al. (2020). Scientific simulations and optimization of the XGIS instrument on board THESEUS. In *Space Telescopes and Instrumentation 2020: Ultraviolet to Gamma Ray*, volume 11444, pages 1254–1262. SPIE.

Mészáros, P. (2019). Gamma-Ray Bursts: theoretical issues and developments. *arXiv preprint arXiv:1904.10488*.

Meszaros, P. and Rees, M. (1993). Relativistic fireballs and their impact on external matter-Models for cosmological gamma-ray bursts. *Astrophysical Journal, Part 1 (ISSN 0004-637X), vol. 405, no. 1, p. 278-284.*, 405:278–284.

Miglio, A., Chiappini, C., Mosser, B., Davies, G., Freeman, K., Girardi, L., Jofre, P., Kawata, D., Rendle, B., Valentini, M., et al. (2017). PLATO as it is: A legacy mission for Galactic archaeology. *Astronomische Nachrichten*, 338(6):644–661.

Miliucci, M., Volpe, A., Fabiani, S., Feroci, M., Latronico, L., Macculi, C., Piro, L., D'Andrea, M., Gatti, F., Puccetti, S., et al. (2024). X-ray Technologies for Astrophysics Missions Supported by the Italian Space Agency. *Condensed Matter*, 9(1):11.

Mizuno, T., Kamae, T., Godfrey, G., Handa, T., Thompson, D., Lauben, D., Fukazawa, Y., and Ozaki, M. (2004). Cosmic-ray background flux model based on a gamma-ray large area space telescope balloon flight engineering model. *The Astrophysical Journal*, 614(2):1113.

Montaruli, T. (2002). The antares project. *Arxiv preprint astro-ph/0207531*.

Moresco, M., Amati, L., Amendola, L., Birrer, S., Blakeslee, J. P., Cantiello, M., Cimatti, A., Darling, J., Della Valle, M., Fishbach, M., et al. (2022). Unveiling the universe with emerging cosmological probes. *Living Reviews in Relativity*, 25(1):6.

O'Brien, P., Hutchinson, I., Lerman, H. N., Feldman, C. H., McHugh, M., Lodge, A., Willingale, R., Beardmore, A., Speight, R., and Drumm, P. (2021). The soft X-ray imager on THESEUS: the transient high energy survey and early universe surveyor.

Oswald, M., Wegener, P., Stabroth, S., Wiedemann, C., Rosebrock, J., Martin, C., Klinkrad, H., and Vörsmann, P. (2005). The MASTER 2005 model. In *4th European Conference on Space Debris*, volume 587, page 235.

Pascale, E., Eccleston, P., and Tinetti, G. (2018). The ARIEL space mission. In *2018 5th IEEE International Workshop on Metrology for AeroSpace (MetroAeroSpace)*, pages 31–34. IEEE.

Piro, L. (1997). BeppoSAX overview. In *AIP Conference Proceedings*, volume 410, pages 1485–1492. American Institute of Physics.

Piro, L., Amati, L., Antonelli, L., Butler, R., Costa, E., Cusumano, G., Feroci, M., Frontera, F., Heise, J., Zand, J., et al. (1997a). Evidence for a late-time outburst of the X-ray afterglow of GB970508 from BeppoSAX. *Arxiv preprint astro-ph/9710355*.

Piro, L., Heise, J., Jager, R., Costa, E., Frontera, F., Feroci, M., Muller, J., Amati, L., Cinti, M., Fiume, D. D., et al. (1997b). The first X-ray localization of a gamma-ray burst by BeppoSAX and its fast spectral evolution. *Arxiv preprint astro-ph/9707215*.

Racca, G. D., Laureijs, R., Stagnaro, L., Salvignol, J.-C., Alvarez, J. L., Criado, G. S., Venancio, L. G., Short, A., Strada, P., Bönke, T., et al. (2016). The Euclid mission design. In *Space telescopes and instrumentation 2016: optical, infrared, and millimeter wave*, volume 9904, pages 235–257. SPIE.

Revnivtsev, M., Sazonov, S., Gilfanov, M., Churazov, E., and Sunyaev, R. (2006). Origin of the galactic ridge x-ray emission. *Astronomy & Astrophysics*, 452(1):169–178.

Sanders, G. H. (2013). The thirty meter telescope (TMT): An international observatory. *Journal of Astrophysics and Astronomy*, 34:81–86.

Schechter, P. (1976). An analytic expression for the luminosity function for galaxies. *Astrophysical Journal, Vol. 203, p. 297-306*, 203:297–306.

Sibthorpe, B., Helmich, F., Roelfsema, P., Kaneda, H., and Shibai, H. (2015). The SPICA mission. *EAS Publications Series*, 75:411–417.

Smart, D. and Shea, M. (2005). A review of geomagnetic cutoff rigidities for earth-orbiting spacecraft. *Advances in Space Research*, 36(10):2012–2020.

Srivastava, S., Labanti, C., Amati, L., Campana, R., Virgilli, E., Marchesini, E., Borciani, E., Mele, F., Dedolli, I., Bertuccio, G., et al. (2024). The XGIS instrument on-board THESEUS: detector principle and read-out electronics. *Journal of Instrumentation*, 19(02):C02005.

Stratta, G., Ciolfi, R., Amati, L., Bozzo, E., Ghirlanda, G., Maiorano, E., Nicastro, L., Rossi, A., Vinciguerra, S., Frontera, F., et al. (2018). THESEUS: A key space mission concept for Multi-Messenger Astrophysics. *Advances in Space Research*, 62(3):662–682.

Tanvir, N. R., Fox, D. B., Levan, A. J., Berger, E., Wiersema, K., Fynbo, J. P. U., Cucchiara, A., Krühler, T., Gehrels, N., Bloom, J. S., et al. (2009). A γ-ray burst at a redshift of z $\approx$ 8.2. *Nature*, 461(7268):1254–1257.

Tavani, M., Barbiellini, G., Argan, A., Boffelli, F., Bulgarelli, A., Caraveo, P., Cattaneo, P., Chen, A., Cocco, V., Costa, E., et al. (2009). The AGILE mission. *Astronomy & Astrophysics*, 502(3):995–1013.

Toma, K., Sakamoto, T., and Mészáros, P. (2012). Population III gamma-ray bursts. *Memorie della Societa Astronomica Italiana Supplement, v. 21, p. 76 (2012)*, 21:76.

Troja, E., Piro, L., Van Eerten, H., Wollaeger, R., Im, M., Fox, O., Butler, N., Cenko, S., Sakamoto, T., Fryer, C., et al. (2017). The X-ray counterpart to the gravitational-wave event GW170817. *Nature*, 551(7678):71–74.

Tsoulfanidis, N. (2015). *Measurement and Detection of Radiation*. CRC Press.

Turon, C. (2006). ESA Space Science Programme, Cosmic Vision 2015-2025, for astrophysics. *Proceedings of the International Astronomical Union*, 2(14):530–531.

Vedrenne, G. and Atteia, J.-L. (2009). *Gamma-ray bursts: The brightest explosions in the universe*. Springer Science & Business Media.

Vernetto, S., collaboration, L., et al. (2016). Gamma ray astronomy with LHAASO. In *Journal of Physics: Conference Series*, volume 718, page 052043. IOP Publishing.

Winkler, C., Di Cocco, G., Gehrels, N., Giménez, A., Grebenev, S., Hermsen, W., Mas-Hesse, J., Lebrun, F., Lund, N., Palumbo, G., et al. (2003). The INTEGRAL mission. *Astronomy & Astrophysics*, 411(1):L1–L6.

Yuan, W., Zhang, C., Feng, H., Zhang, S.-N., Ling, Z., Zhao, D., Deng, J., Qiu, Y., Osborne, J. P., O'Brien, P., et al. (2015). Einstein probe-a small mission to monitor and explore the dynamic x-ray universe. *arXiv preprint arXiv:1506.07735*.

Zinzi, A., Capria, M. T., Palomba, E., Giommi, P., and Antonelli, L. A. (2016). MATISSE: A novel tool to access, visualize and analyse data from planetary exploration missions. *Astronomy and Computing*, 15:16–28.

Zuccon, P. (2004). AMS01 Results. In Astbury, A., Campbell, B. A., Khanna, F. C., and Vincter, M. G., editors, *Particles and the Universe*, pages 404–409.